博士論文（要約）

Development of dynamic distributed fiber-optic sensor for multi-parameter sensing

（マルチパラメータ動的計測のための分布型光ファイバセンサの開発）

朱　夢実

Development of dynamic distributed fiber-optic sensor for multi-parameter sensing (Abridged)

(マルチパラメータ動的計測のための分布型光ファイバセンサの開発)

Mengshi Zhu

Department of Systems Innovation
Graduate School of Engineering

The University of Tokyo

A thesis submitted for the degree of

Doctor of Philosophy

March 2019

I would like to dedicate this thesis to my loving parents...

Acknowledgements

This dissertation is a full stop and an academic summary of my PhD project. Its completion is thanks in large part to the special people who challenged, supported and stuck with me all along the way. I am tremendously fortunate to have my supervisor Prof. Hideaki Murayama working together during the past five years. He gave me lots of freedom to try my smart or stupid ideas and provide me with extremely important advises and support. Thank you to all the other teachers in Giso Lab. It is like being in a family to study and live in the lab. Prof. Kazuro Kageyama offered very valuable opportunity for me to learn advanced carbon fiber materials. Asst. Prof. Tsuyoshi Matsuo gave me advises on the mechanical testing equipment. Special thanks to Mr. Makoto Kanai, and Mr. Go Masuda, they have helped me a lot in the preparations for experiments. No matter what topic it is about, optical , mechanical or material, whenever I asked, they were always glad to give me a hand. Thank you to Dr. Daichi Wada and Dr. Hirotaka Igawa from JAXA for their support in the work on simultaneous measurement. I also want to thank Ms. Yumi Sakai for her very kind supports in the office and daily life. Of course, to my colleagues, Mr. Kentaro Goto, Mr. Victor Shishkin, Mr. Hideharu Ogino, Mr. Keisuke Kimura, Mr. Makito Kobayashi, very glad to have you during my PhD study. Although it is tough, but studying and researching together is also fun. Meanwhile, it is very glad to work with Dr. Daniel Leandro in the past six month. It might be one of the most productive period so far in my research. I really appreciate the discussion with you that gave us the idea on DVS. Moreover, I would like to thank the The University of Tokyo Doctoral Student Special Incentives Program (SEUT-RA) for the financial support. In the end, I am especially grateful to my parents, Mr. Dayong Zhu and Ms. Xia Yin, who supported me emotionally and financially. Thank you for encouraging me in all of my pursuits and inspiring me to follow my dreams. I always knew that you believed in me and wanted the best for me.

Abstract

The transportation, infrastructure, energy, etc. are important for people's life in the modern world. Since more and more complex engineering structure are designed and applied in these fields, to guarantee their safety and have a good knowledge of their performance, researchers have made many efforts, including structural health monitoring (SHM). The typical SHM consists of permanent, continuous, or periodic monitoring comprehensive information of structures on the changes in material and/or geometric characteristics which affect the general structural performances, in order to assess the structural condition, help with the strategy makings, etc., in the practical applications. The representative parameters selected to be monitored heavily depend on the factors including the type and use of a structure, expected loads, material, environmental conditions and possible degradation. In general, they can be mechanical, physical or chemical in which the most frequently monitored physical/mechanical parameters are strain, temperature, vibration, etc. Practically, the sensors employed are further required to be available for diverse fields, have high density information collection capability, but have little disturbance to the essential performance of the host structure.

Although, conventional electrical sensors are able to measure most of those parameters, in the last few decades, fiber-optic sensors (OFSs) have made a significant entrance in the sensor panorama. The OFSs sense the external environmental variations by the perturbed propagating/reflecting light through the core of the optical fiber that are sensitive to multiple parameters by the optical loss, gain, phase, spectral shift, etc. Meanwhile, their advantages such as small, passive, electricity independent in sensing parts, and immune to electromagnetic interference that have large potentials to become the promising technologies in SHM. Moreover, the capability of distributed measurement may tremendously reduce the number of sensors that makes the OFS even more efficient.

In the research, I focus on the fiber Bragg grating (FBG) based OFSs, and explore their sensing functions mainly for strain, temperature and vibration. For the strain and temperature sensing, the long-length fiber Bragg grating was applied to the optical frequency domain reflectometry (OFDR) for serving as the key sensing technique. By using the combinations of FBG and polarization maintaining fiber and novel doped fibers (namely PM-FBG and doped FBG respectively), the measurement has been realized for the distributions of strain and temperature simultaneously. For both approaches the sensors worked at a millimeter order spatial resolution. From the PM-FBG based method to the doped FBG based one, the measurement accuracies have been improved from over 20 με and 2 °C to less than 15 με and 1.5 °C without the degradation of spatial resolution. Meanwhile, for the first time, an adaptive and robust approach

based on over-determined systems has been investigated and developed. It has shown high potential to be applied to advanced multi-core fiber techniques in the future. Additionally, the same interrogation platform has been explored for precise vibration sensing in distribution. Driven by advanced demodulation algorithm, the maximum detectable frequency has been achieved to be 15 kHz.

Generally, in both numerical and experimental studies, it has been proven that by applying the same, OFDR based, interrogator, it is possible to achieve efficient measurement of desired parameters in distribution and dynamically. Moreover, the investigation and validation have shown the possible improvement and exploitation in the future work. Also, the proposed approaches are expected to match the additional preferences for SHM to be such as cost effective, simple and robust.

Contents

List of Figures

List of Tables

Nomenclature

Abbreviations

AWWFT Activation function associated weighted sliding windowed Fourier transform

B-Ge-DF B_2O_3 and GeO_2 co-doped fiber

BOCDA Brillouin optical correlation domain analysis

BOTDA Brillouin optical time domain analysis

BOTDR Brillouin optical time domain reflectometry

C-OFDR Coherent optical frequency domain reflectometry

DAS Distributed acoustic sensor

DOFS Distributed fiber-optic sensor

DSS Distributed strain sensor

DTS Distributed temperature sensor

DVS Distributed vibration sensor

FBG Fiber Bragg grating

FFT Fast Fourier transform

FUT Fiber under test

FWHM Full width at half maximum

Ge-DF GeO_2 doped fiber

Hi-Ge-DF Highly GeO_2 doped fiber

I-OFDR Incoherent optical frequency domain reflectometry

iFFT Inverse fast Fourier transform

NA Numerical aperture

NDT Non-destructive testing

OFDR Optical frequency domain reflectometry

OFS Fiber-optic sensor

OTDR Optical time domain reflectometry

PM Polarization maintaining

PSi-F Pure SiO_2 core fiber

Quasi-DOFS Quasi-distributed fiber-optic sensor

RMSD Root mean square deviation

SAP Stress applying part

SHM Structural health monitoring

SNR Signal to noise ratio

STFT Short time Fourier transform

TDM Time division multiplexing

TLS Tunable laser source

WDM Wavelength division multiplexing

WWFT Weighted sliding windowed Fourier transform

Chapter 1

Introduction

1.1 Background

Since the first demonstration of low loss optical fiber, the growth of opto-electronics and optic communication industries have led to rapid development of fiber-optic technologies including fiber laser, fiber telecommunication, and fiber sensor, for over five decades. As one emerging technologies, fiber-optic sensors (OFSs), employing optical fiber as sensing media, have large advantages of being small, passive, electricity independent in sensing parts, and immune to electromagnetic interference, compared with conventional electrical sensors. When optical fiber is exposed to the varying environment, the external parameter of interest modulates the light propagating trough the fiber that can result in the interactions in loss, optical phase, birefringence, spectral properties, etc. Additionally, with the great progress of material science and optical fabrication technology, various special structures are able to be implemented into the optical fibers that have extremely broadened the potential of OFSs. So far, they have made some inroads into the commercial application being targeted at chemical, biomedical and physical measurements which might cover all the fields of conventional electrical sensors, and are being expected to replace them in the future.

The early work in fiber sensing concentrated on the measurement at a particular point or within a very limited area. However, the realization slowly emerged that by perturbing the transmission properties of an optical fiber through external environments then it might be possible to achieve the measurement as a function of position along the fiber. These so-called distributed measurements have became an extremely important disruptive innovation of fiber sensor technology. It is obvious that the technical ability to make distributed measurements over distances up to tens of kilometers is unique to fiber optics. And the spatial resolution of current approaches have been realized to be in the order of sub-millimeter.

According to the characteristics mentioned above, researchers have found the OFS a promised solution for another emerging technology, structural health monitoring (SHM) which has attracted lots of attentions in the extensive testing and frequent inspections and maintenance of various of structures including airplanes, ships, and bridges. SHM is to permanently monitor comprehensive information of structures on the changes in material and/or geometric characteristics which affect the general structural performances, and stands to reduce the complexity and the costs associated with advanced approaches. By replacing the schedule-based preventative maintenance by on-board, real-time monitoring efforts, the operational safety, reliability and service life are expected to be tremendously improved while the cost will decrease. Conventionally, strain gauges are the most common

sensors for SHM. They make use of calibrated devices that express the stress upon the sample in terms of the strain induced on it. However, they have the disadvantages such as limited sensor number, large numbers of metal wire cables, easy to be interfered by electromagnetic fields, and the metal corrosion issue that make them difficult to serve stably in the long term in the harsh environments. In contrast, the OFSs have shown distinctive advantages in light weight, durability. Furthermore, their multiplexing and distributed capability offers the possibility to reduce dramatically the associated wiring required by electrical sensors employed. Meanwhile, the additional advantages have been explored in the embedded sensing approaches for advanced composite materials. The unique capabilities of OFSs opened an entirely novel range of application possibilities of which we shall explore.

1.2 Scopes and Objectives

This research aims to develop multi-parameter OFSs for dynamic distributed measurement which have potential in SHM applications. For achieving this, it is required to have a fundamental study on the optical fiber properties, fiber-optic sensing principle, signal acquisition and analysis, etc. Although, there are huge works to do through the way to practical SHM applications, in this study, I focus on the development of novel sensing approaches for *strain*, *temperature*, and *vibration*. which involves the aspects of principle, numerical simulation, and experimental validations.

The objectives of the research ultimately include four parts:

- To develop OFS for dynamic distributed simultaneous strain and temperature

  Since in the strain measurement for SHM, large temperature variations usually exist, the temperature compensation is required to reduce the errors caused by cross-sensitivity of OFS. Conventionally, complicated system with one strain sensor and another packaged reference fiber for temperature compensation is used. In this research, approaches using ultra-high birefringence polarization maintaining fibers and doped fibers are proposed in the simultaneous measurement of strain and temperature distribution.

- To develop a fast demodulation for real-time monitoring

  The high spatial resolution, high accuracy, as well as real-time capability of distributed OFS are important for real-time SHM. For newly developed sensing technique a promised demodulation approach is crucial in the measurement accuracy, efficiency and reliability. Thus, a demodulation algorithm considering a balanced performance among the speed and accuracy is to be designed and validated in the research.

- To explore the vibration sensing potential of the strain/temperature sensing platform being developed in the study

  Except for the strain or temperature, vibration information including acoustic emission is another factor which shows high efficiency in SHM. Thus, the vibration sensing approaches of OFS is also of the interest of the research. Considering the proposed strain and temperature sensing solutions, a compatible vibration sensor which has large potential to be integrated is to be developed.

- To establish a numerical model for system design and optimization

In the development of new OFSs, the numerical simulation appears to be highly efficient in associating the design as well as the optimization. In this study, a numerical model of the OFS with high degree of freedom and multiple programming interfaces is to be established and used through the whole process of the sensor development in this research.

1.3 Dissertation Structure

The dissertation is divided into 7 Chapters. Among them from Chapter 1 to Chapter 3 are the general introductions and important background knowledges in details. From Chapter 4 to Chapter 7, the original works in the aspects including principle development, numerical simulation and experimental validation and investigations are presented:

- Chapter 1

  This chapter is the general introduction of the background, motivation of the study, as well as the structure of the dissertation.

- Chapter 2

  This chapter introduces the concept of the emerging technology named as structural health monitoring and the motivation of their development and application. Additionally, the requirements and desired features for a feasible health monitoring system are briefly introduced.

- Chapter 3

  In this chapter, the optical fiber technologies and sensing approaches based on them are firstly introduced for giving a general image of the proposed ideas in this research. Then, the key sensing component, fiber Bragg grating, is introduced in Section 3.2. The solutions for realizing distributed sensing using fiber optical sensors are introduced in Section 3.3 as well as the comparison of OFS technologies in different categories. Section 3.4 and 3.5 present that for the multi-parameter capability, OFSs are attractive and valuable in current SHM developments.

- Chapter 4

  Chapter 4 is for the introduction of the optical frequency domain reflectometry, serving as the fundamental sensing platform through this study. Being combined with the long-length fiber Bragg grating technology, a numerical model is developed and presented for system design and analysis in Section 4.2.

- Chapter 5

  This chapter is the introduction of the developed fast demodulation approach in this work. Firstly, in Section 5.1, two typical demodulation methods and one recently speed enhanced one are introduced briefly. Then, the newly proposed one in this study is introduced in Section 5.2 and compared with existing ones in Section 5.3.

- Chapter 6

  Chapter 6 proposed two main approaches for enabling simultaneous strain and temperature measurement. One is based on the polarization maintaining fiber (Section 6.3) and the other is based on doped fibers (Section 6.4). In addition, a self-evaluation approach is introduced in Section 6.5 aiming for reliable and smart sensing.

- Chapter 7

  As a further exploration, the potential of the proposed system for vibration sensing (a dynamic capability) is introduced in this Chapter. Different from the previously reported ones (Section 7.1), this method offers an efficient solution which is compatible with the developed strain and temperature sensing technologies (Section 7.2).

Chapter 2

Structural Health Monitoring

2.1 Motivation of Structural Health Monitoring

The emergence of SHM is accompanied with the advances in material/structural engineering and complex systems. Since the 1980s, the concept of smart or intelligent materials and structures has become more and more present and been considered as an ideal match with non-traditional materials such as composites [1]. These new ideas were particularly attractive in the fields of aerospace, naval architecture and civil engineering [1–3]. SHM aims to assess the condition of the constituent materials, whole structure, parts, or subsystems, through their whole life. Associated with the real-time monitoring, it can provide a rapid tracking even prognosis of the appearance and evolution of damage, as well as the prediction of residual life. Moreover, the big data of the full history of the structure is the first hand resource for various analysis in the design, failure prevention, etc..

In the evolution of materials, as shown in Fig. 2.1, while the complexity of them are gradually increasing, the researchers tend to be more interested in the composite materials, or in a further step, the intelligent materials. This leads to the fact that we desire to

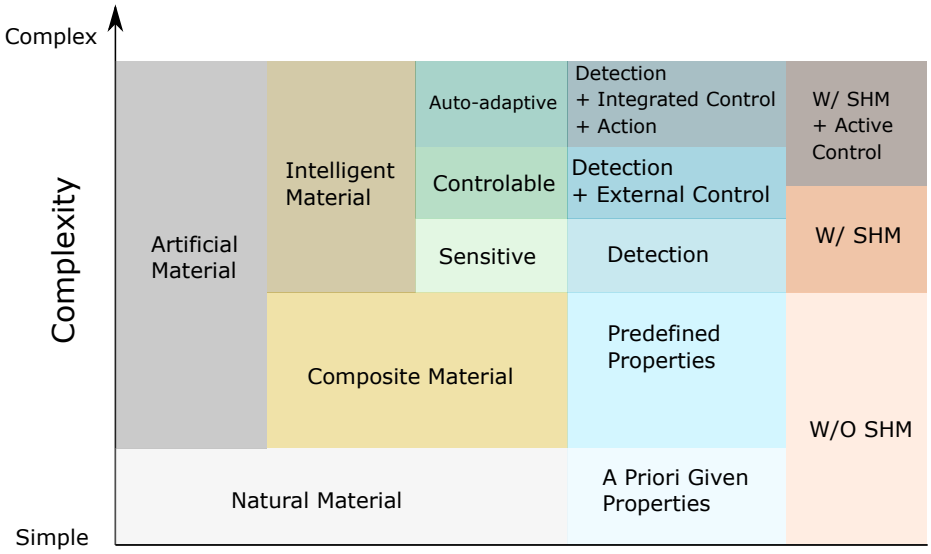

Fig. 2.1. The evolution and relative states of modern material/structure.

construct something for a specific purpose out of a material of which one can never know

enough in terms of the material properties as well as the environment the structure is going to operate in. One typical example where large amount of composite material are used is the Boeing 787. As shown in Fig. 2.2, 50% of the plane is made by composites including carbon fiber and glass fiber based ones. Due to the fact that multiple materials, typically matrix

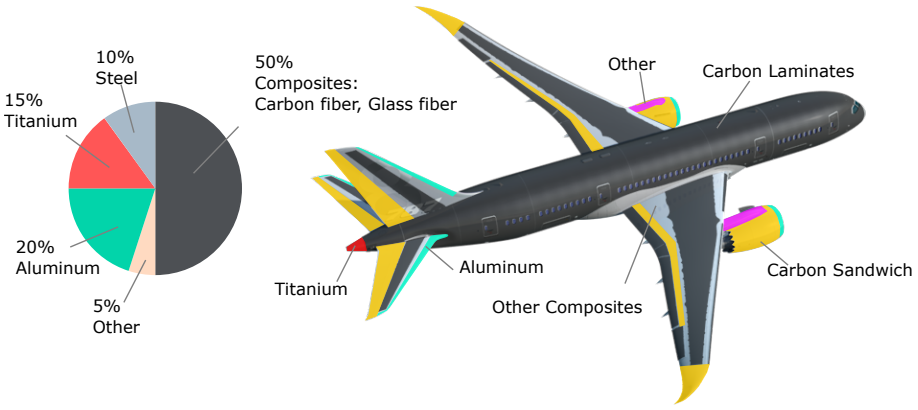

Fig. 2.2. Material usage in Boeing 787: https://www.boeing.com/commercial/787/by-design/#/advanced-composite-use

and fiber, are comprised in composites, the consequent anisotropic properties bring more unpredictable behaviors in the operation compared to their metallic counterparts. Apart from the study on the composite itself which aims to make the material stronger, more advanced demands for the evaluation, assessment, and maintenance of the structure made by them stimulate the development of SHM. There are similar demands in civil engineering as well. For civil infrastructures, such as bridge and pipeline, the aging and damage are happening every second since the birth of the structure. Currently, to assess the condition of the structure and guarantee their performance and safety, examination and detection are scheduled with a fixed time interval. In those efforts, degradation and damage can only be detected after signs caused by fault accumulations are severe and obvious enough. On the other hand, after the repair of detected damages, or scheduled maintenance, there are still lack of evidence to conclude that the structure is safe enough. The inadequate repair/maintenance will make the structure even a larger threat to human live. One recent example is the Morandi bridge collapse in Italy (Genoa, Italy, August, 2018). A section measuring about 200 m fell during the day and killed 43 people, as shown in Fig. 2.3. The

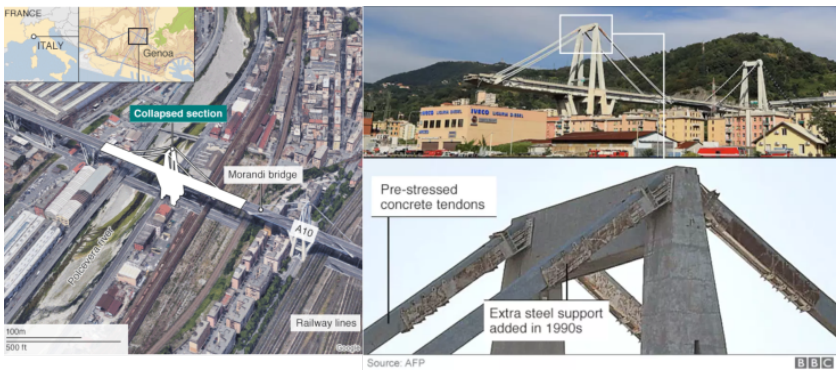

Fig. 2.3. Morandi bridge collapse in Italy, Aug. 2018.

bridge was firstly built in 1967. Some major repair was done in 1990, and the extensive

maintenance has never been stopped throughout the 90s, the 2000s and into the 2010s. The last reconstruction work was done in 2016, only two years before the collapse. Although the complete reason of the accident is still under investigation, it is believed that the repair and maintenance was not adequate. Figure 2.4, depicts a potential to functional failure curve of a hypothetical structure. Although it is natural for a structure's performance to deteriorate

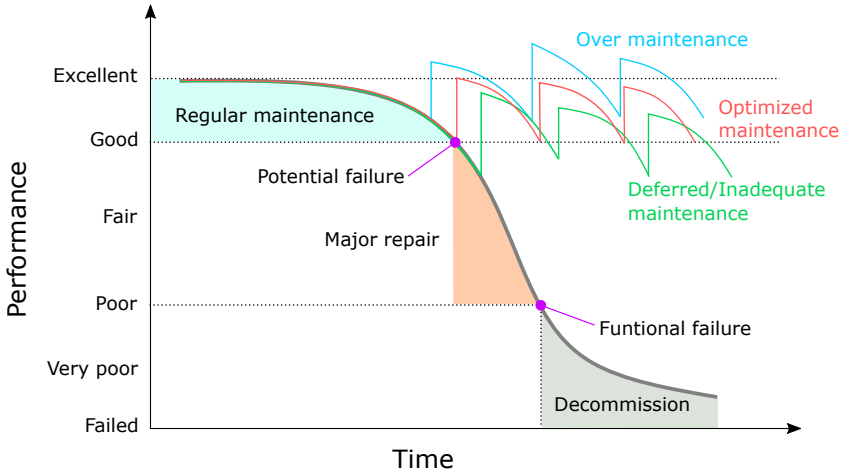

Fig. 2.4. Potential to functional failure curve and preventative maintenance.

and finally face the functional failure, the preventative maintenance may effectively slow down the process. However, if the maintenance is deferred or inadequate, the structure becomes less reliable than expected. On the other hand, the over maintenance will waste lots of resources and time. Therefore, SHM is also expected to give the reasonable signs in time for assisting an optimized maintenance.

2.2 Basic of Structural Health Monitoring System

In recent years, lots of techniques have been developed for the evaluation of structures including non-destructive testing (NDT). It might be misunderstood that SHM is a kind of NDT, or in the opposite. Actually, as shown in Fig.2.5, *non-destructive* is also one of the primary requirements of the SHM, and the integrable sensor can be converted for SHM [1]. Apart from that, SHM system, as aforementioned, is desired to track the time-resolved

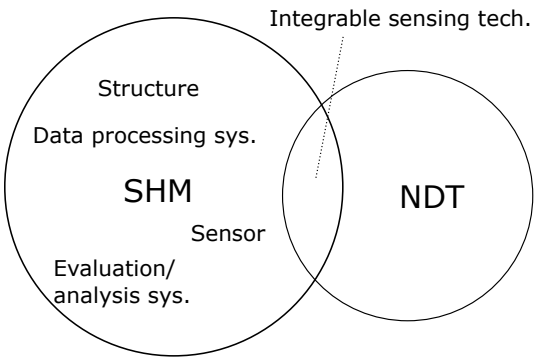

Fig. 2.5. Relation between structural health monitoring and non-destructive testing.

structural performance without disturbing the operation of the structure. In general, a

typical SHM system includes sensors, a data processing module, and a health evaluation module. The sensor collected information being transfer through and stored by data processing system will finally be analyzed by the evaluation system for giving proper reactions and management strategies.

As one primary part of a SHM system, diverse sensors are being developed for the purpose, such as piezoelectric sensor (e.g. PZT), metallic strain gauge, OFS, micro-electro-mechanical systems (MEMS)[4–6]. For those sensors, the different parameters are being measured for assessing the structure from different aspects. Figure 2.6 illustrates some commonly measured parameters. It is not difficult to understand that the desired structural

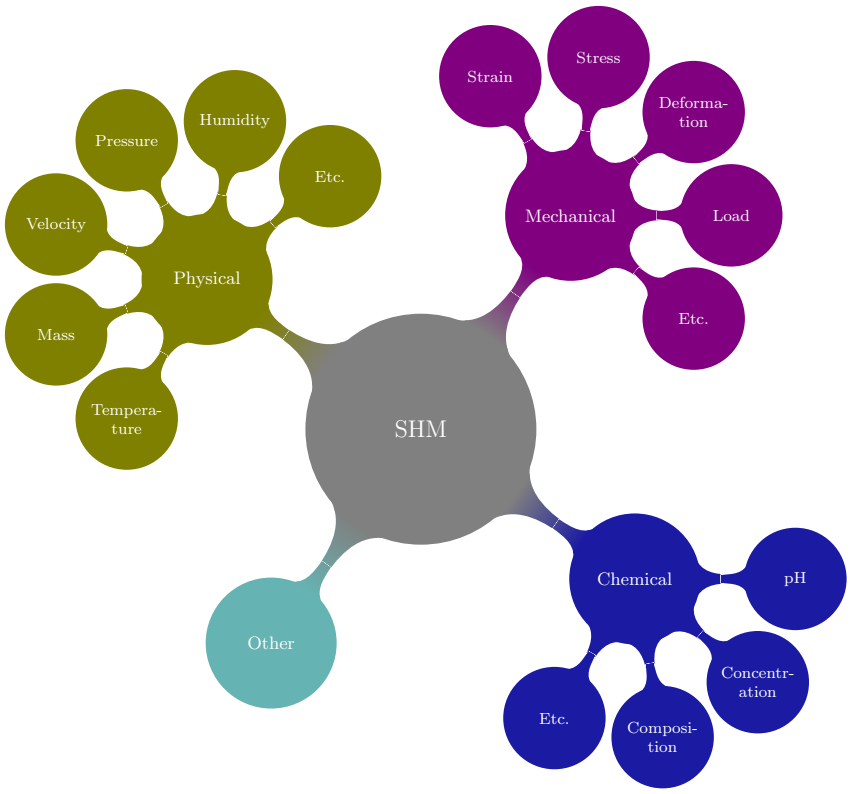

Fig. 2.6. Frequently monitored parameters in structural health monitoring.

information is not required to be directly measured using applied sensor. For example, the deformation may be reconstructed using the strain and geometry, or being further applied for the load estimation [1, 4, 7, 8]. SHM is not only a technique in the preventative efforts, it is also expected to help with the design and manufacturing to make the engineering structure lighter, more reliable, more cost effective and more available. To achieve the targets, the desired sensors should be smaller, lighter, cheaper, etc. However, in practical SHMs, usually, more than one type of sensors are installed for monitoring the structure in different aspects and meanwhile improve the redundancy. For example, in the *Wind and Structural Health Monitoring System*(HK, China), Tsing Ma, Ting Kau, Kap Shui Mun and Stonecutters bridges are being monitored by employing accelerometers, strain gauges, displacement transducers, level sensing stations, anemometers, temperature sensors and dynamic weight-in-motion sensors [9]. These sensors are supposed to measure everything from tarmac temperature and strains in structural members to wind speed and the deflection

and rotation of the kilometers of cables and any movement of the bridge decks and towers. If some of the parameters can be measured using one sensor, the complexity and cost of the SHM system can be extremely reduced. Therefore, the multi-parameter sensors have large potential in such applications.

Among the frequently monitored parameters, the *strain*, *temperature*, and *vibration* are the most interesting for me in this research.

- **Strain:** Almost every structure are considered to stand the load within a certain limit. During the operation, the load should never be out of the range. Therefore, load as well as structural strength are very critical that proper parameters are desired to be selected for evaluating their condition. Strain might be the most straightforward one to trace the stress, strength, load, etc.

- **Temperature:** The temperature is a critical parameter which in many aspects influences the structural performance as well as the SHM efficiency. On the one hand, the structure may suffer from the temperature variation induced issues such as thermal expansion, thermal fatigue. On the other hand, the responses of the sensors are usually affected due to the change of ambient temperature. To reduce the effect, adequate compensation schemes must be included in the signal conditioning part of the sensors.

- **Vibration:** Vibration is one inherent dynamic behavior of structures. One of the most comprehensive damage detection methods is based on acoustic emissions (AE). It is the stress waves produced by the sudden internal stress redistribution of the materials subject to the internal structural variation, which can be detected by vibration (or equivalent) sensors.

Notwithstanding, every SHM solution seems to conduct the analysis at a certain moment, the static/quasi-static measurement is not enough. The behaviors of the structures over time are also critical. For example, fatigue, referring to weakness in metal or other materials caused by repeated variations of stress [10], cannot be assessed through static measurement. Thus, the real-time monitoring is attracting more and more attention. Furthermore, by employing the collected information of the real-time behaviors, the P-F curve (Fig. 2.4) can be predicted more reliably.

In general, an optimal sensing solution for SHM is expected to be accurate, sensitive, stable, and repeatable. Meanwhile, an adequate sensing range, resistant to extreme environmental condition, and compensation to unexpected perturbations are also being taken into account.

Chapter 3

Fiber-Optic Sensors

3.1 Introduction of Fiber-Optic Sensor

OFS is an emerging technique believed to have large potential in SHM applications[5, 11, 12]. It employs an optical fiber as sensing media for the external environmental perturbations. The development of OFSs was actually stimulated by other fiber-optic technologies in telecommunications. OFSs rely on communication technology to provide basic equipment and components such as fiber amplifiers, detectors, couplers, splitters, wavelength multiplexers,etc. In the past few decades, OFSs have gradually made a significant entrance in the sensor panorama. The demands in fiber sensing market also facilitate the development of different versions of optical fibers purely for the sensing community.

In order to understand the principles of OFSs, firstly the optical fiber technology is briefly introduced. An optical fiber is a flexible fiber that can function as a waveguide to transmit light from one end to the other. It is usually made of silica glass and formed into several layers, as depicted in Fig. 3.1. The light-carrying core is surrounded by the cladding and protected by the coating. In order to trap the light in the core by the principle of *total internal reflection*, the refractive index of the core must be higher than that of the cladding. Injecting the light into the optical fiber core at the incident angle within the acceptance

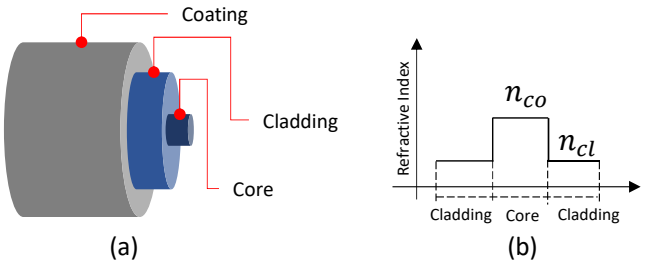

Fig. 3.1. (a) Schematic of optical fiber. (b) Refractive index profile of step-index fiber.

range, the light will propagate in the core by total refraction on the interface between core and cladding. The acceptance angle, θ_{ac}, is described using the numerical aperture (NA) which can be expressed as

$$\mathrm{NA} = \sin\theta_{\mathrm{ac}} = \sqrt{n_{\mathrm{co}}^2 - n_{\mathrm{cl}}^2}. \tag{3.1}$$

where n_{co} and n_{cl} are the refractive indexes of the fiber core and cladding, respectively [13]. Practically, the optical fiber can be divided into two categories, single mode and multi-

mode, depending on the number of propagation modes in the fiber core, as shown in Fig. 3.2. Single mode fiber enables one type of light mode to be propagated at a time, while multi-mode allows multiple modes. The difference between these fibers mainly lie on the fiber core diameter, wavelength, light source and bandwidth. In general, the relation can be expressed in terms of normalized frequency, V, which can be calculated as

$$V = \frac{2\pi \mathrm{NA} r_{\mathrm{co}}}{\lambda}, \tag{3.2}$$

where the r_{co} is the fiber core radius, and λ is the wavelength of the propagation light. For a single mode fiber, the value of V should be smaller than 2.405 [13]. However, it should

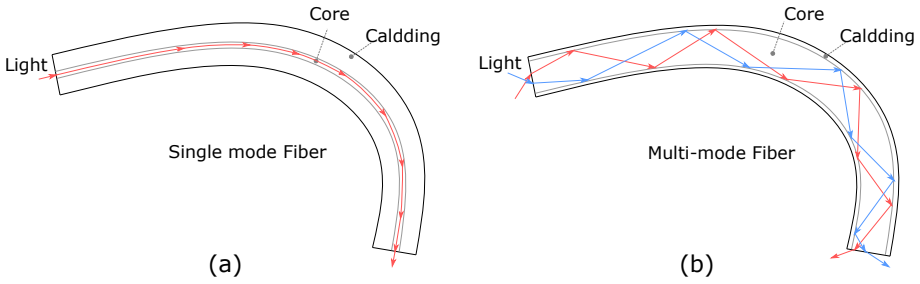

Fig. 3.2. (a) Light propagation in single mode fiber. (b) Light propagation in multi-mode fiber.

be noted that the propagation mode of single mode fiber is not truly "single" since two degenerate modes polarizing at two orthogonal axes are also supported. Ideally, in a perfect cylindrically symmetric and stress-free fiber, a polarization mode in one direction would not couple to the other. Practically, the random variations in the core shape along the fiber during the drawing process and stress-induced anisotropy will result in a cross-talk of the two polarizations. Mathematically, the mode-propagation constant β becomes slightly different for the modes polarized in the x- and y-directions, referring to the modal birefringence [14]. Defined by a dimensionless parameter B, the strength of modal birefringence can be expressed as

$$B = \frac{|\beta_x - \beta_y|}{k} = |n_x - n_y|\,, \tag{3.3}$$

where $k = 2\pi/\lambda$ is the wavenumber, n_x and n_y are the refractive indexes of x and y axis, respectively. Specially, the axis along which the refractive index is smaller is called *fast axis* because of the larger group velocity, while the other axis is called *slow axis*. In standard optical fibers, B varies because of the fluctuations in the core shape and residual anisotropic stress which lead to the randomly changed polarization states. For some applications, the fibers are desired to keep the polarization of the propagating light not changing. Such fibers are called polarization maintaining (PM) fibers. The basic mechanisms of birefringence, such as anisotropic transverse stress, non-circular core, bending, twist, and electromagnetic field, have introduced in details by Rashleigh *et al.* [15]. As shown in Fig. 3.3, generally, there are two primary types of PM fibers. One is using non-centrosymmetric structure deformed from regular fibers such as the Elliptical-clad and D-shaped Elliptical Core fiber. The other type is the stress-induced PM fiber such as PANDA and Bow-tie fiber. The second type of fibers are fabricated by employing stress applying parts (SAPs). When a preform is heated to a temperature at which a fiber can be drawn, the preform is in a stress-free state. As the fiber cools, regions with different thermal expansion will induce large thermal stresses.

Fig. 3.3. Different types of polarization maintaining fibers.

Then, the birefringence is achieved though the photoelasticity, which can be expressed as

$$B = |(C_y - C_x)(\sigma_y - \sigma_x)|\,, \tag{3.4}$$

where C_x, C_y are the stress-optic coefficients in the x and y directions, σ_x, σ_y are the axial stresses in the corresponding directions, respectively. Generally, all types of fibers including single mode, multi-mode, and PM ones have potentials to serve as sensors.

Apart from the propagation, the light through the fiber interacts with the external environmental perturbations which enables the sensing function. The transmitted/reflected light might be modulated by the environmental variations in its intensity, phase, polarization, frequency, wavelength, etc.. By detecting and then demodulating the information carried light signals, the target parameters can be interrogated. Compared with conventional electrical sensors, OFSs have advantages such as small, passive, electricity independent in sensing parts, immune to electromagnetic interference, and can be distributed that have large potential various fields including energy, civil engineering, airspace, airplane, naval architecture, and marine technology. Moreover, the measurable parameters of OFSs are diverse. By different scenarios they may be sensitive to strain, stress, temperature, vibration, displacement, acceleration, etc. Thus, they can be designed and optimized for different sensing requirements.

By the sensing principle, the OFSs can be divided into three categories: *interferometric, grating based, and scattering based.*

- **Interferometric:** It has been understood for decades that fiber-optic interferometers can be applied as sensors. Among them, the Sagnac, Fabry–Perot, Mach–Zehnder and Michelson interferometers are the most widely studied [16]. Fig. 3.4 illustrates the basic structures of different fiber optic interferometers. The sensing principles of them are based on the change in the optical phase difference between two coherent light waves, caused by the variations in one or multiple parameters. Interferometric sensors are suitable for single-point detection.

- **Grating based:** Fiber grating is a kind of micro structure primarily manufactured into the fiber core. Being applied as sensing elements, they may be based on Bragg gratings, chirped grating, long-period grating, etc.. [17] Basically, they response to the measurands by spectral shifts. In the manufacturing, the initial properties of the gratings, such as shape, wavelength, can be defined that brings large freedom in the sensor design.

- **Scattering based:** The scattering based OFSs generally refer to the ones based on the spontaneous/stimulated scattering including Rayleigh, Brillouin and Raman, as shown in Fig. 3.5. When the frequency of the propagating light is far from the medium resonance frequency of the scattering particles in the optical fiber, a time dependent

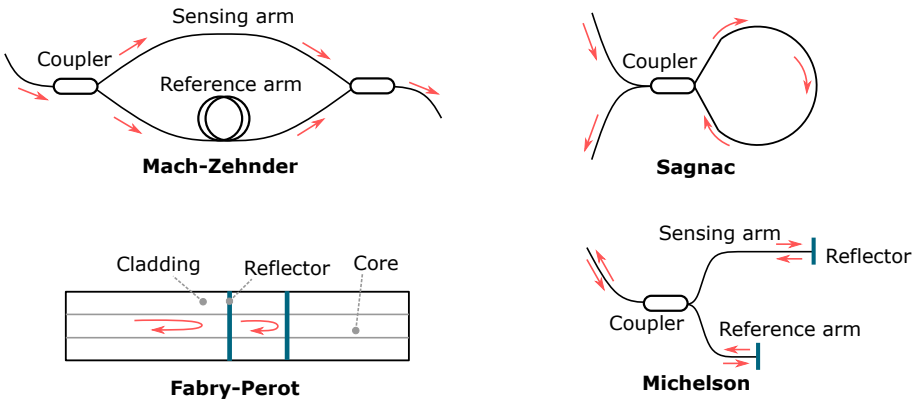

Fig. 3.4. Different types of fiber-optic interferometers.

dipole will be generated. The scattering is caused by the dipole induced secondary electromagnetic wave. Among them, Rayleigh, an elastic scattering, occurs when the electromagnetic radiation by particles is much smaller than the light wavelength. The two peaks appearing on both sides of the Rayleigh peak are the Brillouin peaks. They are contributed by the mass acoustic modes (phonon). The photon may lose energy (Stokes process) or gain energy (anti-Stokes process) by absorption that is inelastic. Another inelastic scattering called Raman is caused by the vibrational properties of matter. Different from Brillouin scattering where the scattering of photons is caused by large scale, low-frequency phonons, in Raman scattering, photons are scattered by the effect of vibrational and rotational transitions in the bonds between first-order neighboring atoms.

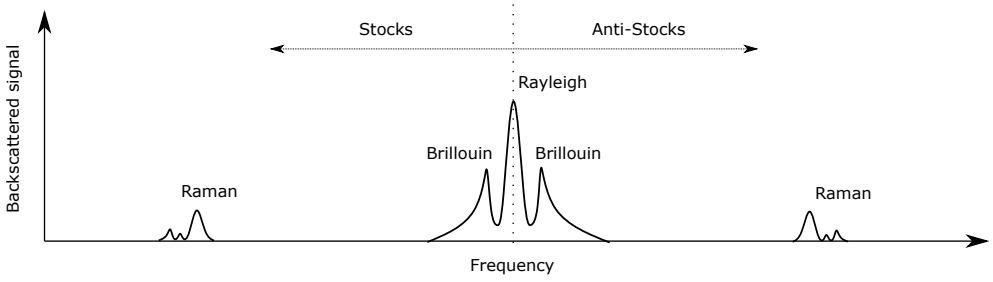

Fig. 3.5. Different types of light scattering in optical fiber.

3.2 Fiber Bragg Grating

Fiber Bragg grating (FBG) is a periodic modulation (distribution) of the refractive index in the core of an optical fiber, as shown in Fig. 3.7. It can be inscribed using intense UV source through point-by-point, interferometric or phase mask technique [18]. Mathematically, the modulation of refractive index can be simplified as

$$\delta n_{\text{eff}}(z) = \overline{\delta n}_{\text{eff}} \left\{ 1 + \upsilon_{\text{frg}} \cos \left[\frac{2\pi}{\Lambda} z + \phi_{\text{cp}}(z) \right] \right\}, \tag{3.5}$$

where $\overline{\delta n}_{\text{eff}}$ is the "dc" index change spatially averaged over a grating period, υ_{frg} is the fringe visibility of the index change, Λ is the pitch (period) of the grating, and $\phi_{\text{cp}}(z)$ is the grating chirp along the positions[19]. The optical properties of a fiber grating are essentially determined by the variation of the induced index modulation along the fiber axis. Figure 3.6 illustrates two common modulations in researches. Specially, if the modulation approaches to zero at the end of the grating, it refers to the apodization technique. Apodized gratings offer significant improvement in side-lobe suppression while maintaining the reflectivity and a narrow bandwidth. For apodized grating, the $\overline{\delta n}_{\text{eff}}$ should be rewritten to

$$\overline{\delta n}_{\text{eff}}' = \overline{\delta n}_{\text{eff}} f_{\text{apd}}(z), \tag{3.6}$$

where $f_{\text{apd}}(z)$ is the apodization profile which is a function of position. For a single mode

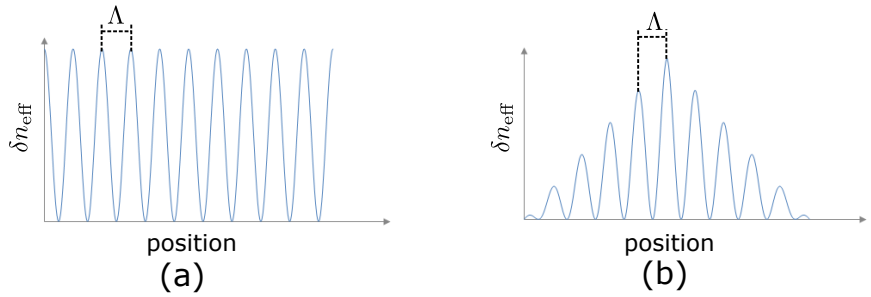

Fig. 3.6. (a) Refractive index modulation of uniform grating. (b) Refractive index modulation of Gaussian-apodized grating.

FBG, injecting spectrally broadband light into the fiber, a narrowband spectral component at the Bragg wavelength is reflected by the grating, as shown in Fig. 3.7. According to the Bragg's law, the selected wavelength, namely Bragg wavelength, is expressed as

$$\lambda_{\text{B}} = 2n_{\text{eff}}\Lambda, \tag{3.7}$$

where n_{eff} is the effective refractive index of the core. Figure 3.8 shows the spectra of the

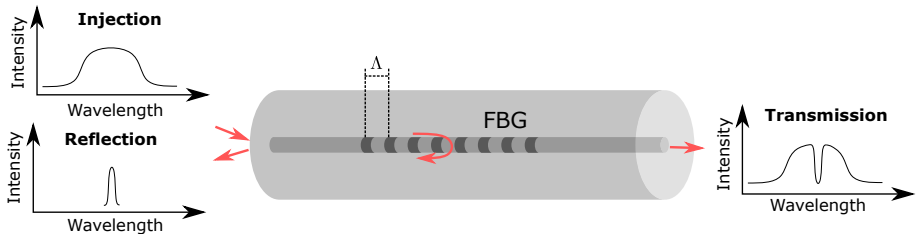

Fig. 3.7. Schematic of the FBG principle.

reflection from a uniform and Gaussian-apodized FBG centered at about 1550 nm. It can be seen that the side-lopes of apodized FBG has been effectively removed. While for an FBG in PM fiber, the Bragg wavelength will split into two peaks which polarize in two orthogonal directions. Thus, the Bragg wavelength can be expressed as

$$\lambda_{\text{B},x} = 2n_x\Lambda, \tag{3.8}$$
$$\lambda_{\text{B},y} = 2n_y\Lambda. \tag{3.9}$$

The Bragg wavelength is a very important parameter that represent the strain and temper-

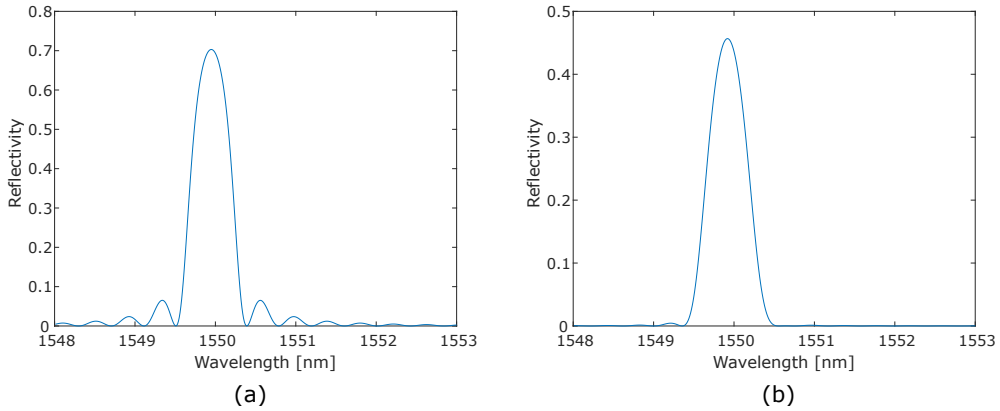

Fig. 3.8. Spectra of FBGs: (a) uniform, (b) Gaussian-apodized.

ature condition when the fiber is manufactured. Once the environmental variations occur, the shift in Bragg wavelength will be observed. The shift with respect to strain, $\Delta\varepsilon$, and temperature, ΔT, changes can be expressed as

$$\Delta\lambda_{\mathrm{B}} = 2n_{\mathrm{eff}}\Lambda\left\{1 - \frac{n_{\mathrm{eff}}^2}{2}\left[P_{12} - \nu(P_{11} + P_{12})\right]\right\}\Delta\varepsilon + 2n_{\mathrm{eff}}\Lambda\left[\alpha + \frac{\left(\frac{dn}{dT}\right)}{n_{\mathrm{eff}}}\right]\Delta T, \tag{3.10}$$

where ν is the Poisson's ratio, $P_{11,12}$ is Pockel's coefficients, α is the thermal expansion coefficient, dn/dT is the thermo-optic coefficient, respectively [17, 20].

3.3 Distributed Fiber-Optic Sensing Techniques

So far, the OFS might be the most applicable solution for fully distributed sensing ever reported. In a broad sense, the distributed fiber-optic sensors (DOFSs) may include fully-distributed and quasi-distributed ones. For the monitoring of large structures such as airplane, bridge, oil pipe, ship, off-shore platform, etc. sensors are supposed to be installed on hundreds/thousands of positions on the structures to assess their condition. Instead of applying numbers of point sensors with heavy associated wires, the distributed solutions which enables the measurement at multiple points are desired in such applications. In terms of OFS, the fully distributed one is expected to reveal information such as temperature, strain and vibration from any point along an optical fiber through light scattering. For a quasi-distributed fiber-optic sensor (Quasi-DOFS), the sensing point is selected and not necessary to be continuous. Classified by the measurands, the most popular DOFSs under study for physical variations are distributed strain, temperature and vibration sensors (DSS, DTS, DVS). Since the acoustic signal may also be regarded as vibration, in some cases, the DVS is also called distributed acoustic sensor (DAS). The key of these techniques lies on the selection of proper fiber-optic phenomena where both the measurand and spatial information is carried by the light signals. Generally speaking, they can apply light scattering or structured optical components. In this section, I will introduce two categories of the DOFSs based on backscattering and FBG, and briefly compare their pros and cons.

3.3.1 Interrogation Techniques

Despite the sensing type, the common thing in almost all DOFSs is that the variation of external environment is probed by the injected light and carried by its backscattering/reflection. To detect the light signal and reveal the measurands as well as the spatial information, the most broadly used interrogation techniques are the optical time domain reflectometry (OTDR) and optical frequency domain reflectometry (OFDR).

Optical Time Domain Reflectometry

Essentially, the OTDR technique is compatible to almost all the DOFSs. It applies light pulse to determine the round-trip impulse response of the fiber. Figure 3.9 depicts a basic structure of OTDR and its principle. When a short probe pulse is launched into the fiber under test (FUT), during its travel in the fiber, various attenuation will be induced by the environmental variations (e.g. strain, temperature). Then the backscattering light will return and be sensed by the photodetector at the fiber end where the probe pulse is injected. The position on the fiber is calculated from the time delay of each received signal, considering the light speed in the fiber core. In the system, there are two important

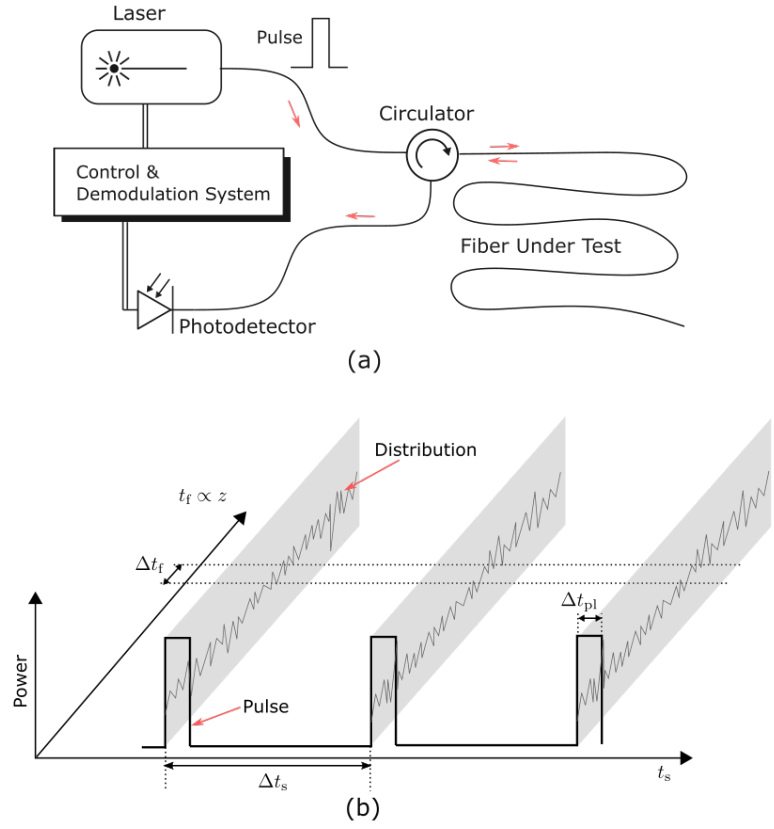

Fig. 3.9. The schematic and principle of a basic OTDR: (a) structure, (b) principle.

time axes. The slow one, t_s, is the time when the probe pulse are launched, and the fast one, t_f, which is proportional to the distance, z, is time when each round-trip light signal is detected. Defining the time interval of each probe as Δt_s, the repetition rate is calculated as

its reciprocal, $1/t_s$. At the same time, the highest readout resolution of spatial distribution is calculated as

$$\Delta z_{rd} = \frac{v_{co}\Delta t_f}{2}, \tag{3.11}$$

where Δt_f is the time interval of each detected signal and v_{co} is light speed in the fiber core. This is because of that the time delay of the rising and falling edges of the pulse will induce overlaps in the received signals. On the other hand, the spatial resolution is limited by the width of the pulse, Δt_{pl}, that can be mathematically described as

$$\Delta z_{sp} = \frac{v_{co}\Delta t_{pl}}{2}. \tag{3.12}$$

However, due to the attenuation, the maximum measurement length of OTDR is mainly determined by the energy of the probe pulse. Thus, for a longer length, a wider pulse is desired. Taking Eq. (3.12) into consideration, it is apparent that there is a trade-off between the maximum measurement length and spatial resolution. Practically, the choose of them should depend on the specific application.

Optical Frequency Domain Reflectometry

OFDR methods may be divided into two main variants: incoherent OFDR (I-OFDR) and coherent OFDR (C-OFDR)[21]. Similar to OTDR, OFDR also rely on the round-trip propagation of the light in optical fiber. However, instead of directly retrieving the position information from the time delay, the frequency response is used. To achieve this, in an I-OFDR, the general setup is the same as shown in Fig. 3.9 (a). The difference is that the input pulse is replaced by the intensity modulated continuous wave laser. By keeping the optical frequency of the input light constant, and changing the modulation frequency periodically or step-wise, the response as a function of modulation frequency will be detected. After applying the Fourier transform to the frequency response, the obtained impulse response in time domain can provide the positions through the same process as introduced in OTDR technique. On the other hand, for C-OFDR, the mechanisms are based on the fiber-optic interferometers by injecting the light with swept frequency/wavelength using tunable laser source (TLS). In this study, the C-OFDR is used because of the advantages including that low power input is needed, no saturation of detectors occurs, the required bandwidth for photodetector is small, and the measurable range of the backscattering/reflection amplitude is large.

Figure 3.10 illustrates a classic simple C-OFDR based on the Michelson interferometer and linear frequency swept TLS. Assuming that the speed of frequency sweep, γ_f, is constant, the reflection wave in the reference arm can be expressed as

$$E_r(t) = E_0 \exp\left\{j\left[2\pi f_0 t + \pi\gamma_f t^2 + \phi(t)\right]\right\}, \tag{3.13}$$

where E_0 is the amplitude, f_0 is the initial optical frequency of TLS, and $\phi(t)$ is the optical phase with respect to time, t, respectively. On the other hand, the wave function from the sensing arm at position z on the FUT can be expressed as

$$E_{s,z}(t) = R_s(\tau_z, f_t) E_0 \exp\left\{j\left[2\pi f_0 (t-\tau_z) + \pi\gamma_f (t-\tau_z)^2 + \phi(t-\tau_z)\right]\right\}, \tag{3.14}$$

where τ_z is the round-trip time delay, $f_t = f_0 + \gamma_f t$ is the optical frequency at time t, R_s is the reflection profile, respectively. Considering that $\tau_z = 2z/v_{co}$, the reflection is also the

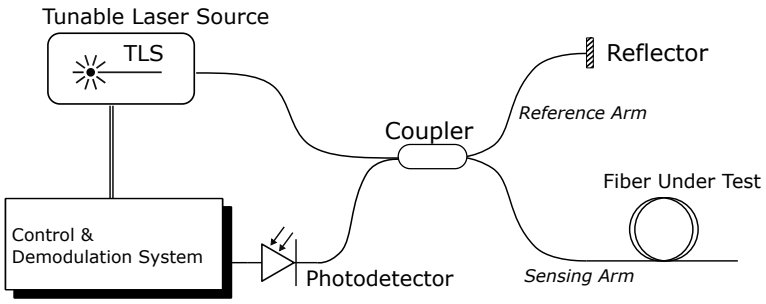

Fig. 3.10. Schematic of a classic C-OFDR based on Michelson interferometer.

function of position. It has to be noted that the position here refers to the path difference between the reflector and the points on FUT. According to the mechanism of Michelson interferometer, the photodetector received beat signal can be expressed as

$$\begin{aligned} I(t) &= \sum_z \left(E_\mathrm{r} + E_{\mathrm{s},z}\right)\left(E_\mathrm{r} + E_{\mathrm{s},z}\right)^* \\ &\propto \sum_z R_\mathrm{s} \cos\left\{2\pi\left[\gamma_\mathrm{f}\tau_z t + f_0\tau_z + \frac{\gamma_\mathrm{f}\tau_z^2}{2} + \phi(t) - \phi(t-\tau_z)\right]\right\}, \end{aligned} \tag{3.15}$$

where $*$ represents the complex conjugate, $\gamma_\mathrm{f}\tau_z$ refers to the frequency of beat signal. It is apparent that, by applying Fourier transform to Eq. (3.15), the distribution at position domain can be retrieved. It should be mentioned that the time related phase terms in the beat signal will induce errors for the measurement. Additionally, the errors might be generated by the phase noise, nonlinear laser sweep, etc.. In C-OFDR, the theoretical highest spatial resolution is determined by the sweep range of the TLS, Δf_rng, which can be expressed as

$$\Delta z_\mathrm{sp} = \frac{v_\mathrm{co}}{2\Delta f_\mathrm{rng}}. \tag{3.16}$$

On the other hand, the measurement length is mainly limited by the coherent length of TLS, SNR, etc. For convenience, in the following parts of the thesis, all the "OFDR"s refer to the "C-OFDR".

3.3.2 Backscattering Based Techniques

As aforementioned, the light scattering is caused by the interaction of light waves and particles due to the non-uniformities in the optical fiber. If the direction of the scattering light is opposite to the injection, it is called backscattering which is naturally "distributed". By using different integration techniques, all three types of backscattering, Rayleigh, Brillouin, and Raman, can be applied for distributed sensing.

Rayleigh Based Techniques

Rayleigh scattering is an elastic scattering that the scattered power is simply proportional to the power of incident light, while no energy exchange between light and solid particles occurs. Thus, there is no change in frequency of the scattered light comparing with that of the input light. This backward propagating light has a position difference (optical phase) induced time delay that can be used for distributed sensing. If the fiber is perturbed by

such as strain, temperature, vibration, the relative positions of scattering centers change, resulting in the variations in the detected beat pattern. This change can be tracked by using a phase sensitive OTDR (Φ–OTDR) for vibration sensing [22–24], or using OFDR for strain/temperature measurement [23, 25, 26].

Brillouin Based Techniques

Different from the Rayleigh scattering, spontaneous Brillouin scattering is an inelastic phenomenon generated from the interaction between the incident light and the thermally-induced material-density fluctuations (acoustic phonons) traveling along the fiber at the speed of sound [23, 27]. These phonons modulate the refractive index through the stress-optical effect and produce a traveling fluctuation of the refractive index. In this interaction, the wavelength matching among longitudinal acoustic phonons and input probe optical wavelength generates two additional signals at frequencies on either side of the incident light (Rayleigh peak). The separation of the Brillouin peaks from incident light, referring to the Brillouin frequency shift, ν_{B}, mathematically satisfies

$$\nu_{\mathrm{B}} = \frac{2n_{\mathrm{eff}}v_{\mathrm{a}}}{\lambda_0}\sin\left(\frac{\theta}{2}\right), \tag{3.17}$$

where v_{a} is the acoustic velocity in the fiber, λ_0 is the incident light wavelength, and θ is the angle between the incident and scattered light, respectively. In the case of backscattering, $\theta \approx \pi$. Since the local temperature and the strain of the fiber influence the frequency and intensity of the Brillouin scattering, it can be applied as distributed strain and temperature sensor [28, 29]. The mode widely explored ones are Brillouin optical time domain reflectometry (BOTDR) and Brillouin optical time domain analysis (BOTDA) [23]. Additionally, the techniques using Brillouin optical correlation domain analysis (BOCDA) have been demonstrated [30].

Raman Based Techniques

Spontaneous Raman scattering is another inelastic process caused by molecular vibrations. The incident light is scattered through the interaction between the light and electrons of vibrating molecules (optical phonons), and its frequency is shifted by an amount equivalent to the resonance frequency of the lattice oscillation [27, 31]. When light is launched into a fiber to probe the Raman scattering, apart from the Rayleigh scattering, other two spectral components are generated: the Stokes component at a lower frequency, and the anti-Stokes one at a higher frequency. The temperature around the fiber intrinsically affects the intensity of the anti-Stokes peaks, while the Stokes signal is temperature insensitive. Therefore, temperature can be measured by the ratio between the anti-Stokes and the Stokes light intensity where backscattered photons are generated. This mechanism has been well exploited as distributed temperature sensors by employing OTDR as integrator [23, 27, 32].

3.3.3 FBG Based Techniques

As introduced, FBG, essentially inscribed within a limited length (millimeters or centimeters), can serve as both strain and temperature sensors mathematically described by Eq. (3.10). Compared to Rayleigh-based technology, FBGs-based technology can achieve much

higher SNR. The key to realize distributed measurement is the in-line inscription and compatible interrogation technologies. Figure 3.11 shows three kinds of in-line inscribed FBGs. In the sparse short FBG array, these FBGs can have different Bragg wavelengths and can be interrogated by wavelength devision multiplexing (WDM) technique enabling quasi-distributed measurements[17, 33]. However, the number of FBGs in this method is limited by the bandwidth of the incident light. If the Bragg wavelengths are the same, the time division multiplexing (TDM) technique can be applied [17, 20, 34]. The TDM and WDM can be combined for increasing the number of in-line FBGs. In the dense short/long FBG based systems, these FBGs are usually spectrally located at the same Bragg wavelength. Based on current techniques, the all-grating fiber is commercially available[35]. To make more effective use of the high density of FBGs, the OFDR which has a very high spatial resolution (millimeter order) is preferred[7, 36–39]. It is worth mentioning that the high spatial resolution enables the dense FBG based sensors to be applied for the precise measurement of elaborate structure/substructures. Considering the ultra-high information density of the dense long-length FBG array, the DOFSs based on it can be treated as fully distributed.

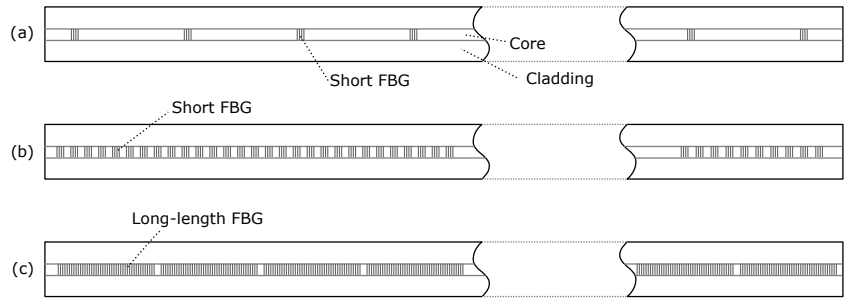

Fig. 3.11. Schematic of three types of in-line inscribed FBGs: (a) sparse short FBG array, (b) dense short FBG array, (c) dense long-length FBG array.

3.3.4 General Comparison of Distributed OFSs

Since various OFSs have been demonstrated, it is interesting and valuable to compare their capabilities in some general aspects, especially for end-users. Neglecting the measurands which differ between the applications, two unique characteristics in DOFSs are the sensing length (measurement length) and spatial resolution. The measurement length is the maximum length within which an sensor can serve (different from measurement distance). While the spatial resolution is the minimum size of distribution that can be recognized by the sensor. In most cases, there is a trade-off between these two values. Table 3.1 shows some reported DOFSs and their claimed sensing performances. Generally, most of the listed techniques are available for the strain and temperature measurement, while the sensing length and spatial resolution are quite different. Practically, such properties will limit the area of potential application. Since the claimed accuracies of strain and temperature are heavily dependent on where the sensors are applied. For a clear illustration, in this part, the comparison of strain/temperature measurable DOFSs is made, in the aspects of sensing length, spatial resolution and single measurement time, as shown in Fig. 3.12. It is not difficult to find that if one of the three properties is expected to be improved, the other two will be sacrificed. Assume that there are an airplane and a pipeline to be monitored. Their desired sensing performances (sensing length, spatial resolution, measurement time) are (50 m, 0.5 mm, 0.01 s) and (10 km, 0.5 m, 30 s), respectively. It is apparent that FBG-OFDR is more

Table 3.1. Performances of selected distributed fiber-optic sensors.

Type	Sensing length	Spatial resolution	Measurands	Measurement time (single)	Ref.
BOTDR	20–50 km	1 m	Str./Temp.*	> 5 min	†
BOTDA	2 km	2 cm	Str./Temp.	n/a	[40]
	1 km	10 cm	Str./Temp.	> 2 min	‡
	150 km	2 m	Str./Temp.	n/a	[41]
BOCDA	10.5 km	1 cm	Str./Temp.	5833 h	[42]
	17.5 km	8.3 mm	Str./Temp.	1.5 h	[43]
	500 m	3 cm	Str./Temp.	0.014 s	[44]
Raman–OTDR	0.9 km	0.4 m	Temp.	5 min	[45]
	37 km	17 m	Temp.	n/a	[46]
Rayleigh–Φ–OTDR	1 km	0.5 m	Vibr.*	2×10^{-5} s	[47]
Rayleigh–OFDR	35 m	22 µm	n/a	3 s	[48]
	30 or 70 m	1 cm	Str./Temp.	0.4–2.1 s	○
	40 km	5 cm	n/a	n/a	[49]
	10 km	40 m	Vibr.	1×10^{-3} s	[50]
FBG–OFDR**	26.5 m	1.6 mm	Str./Temp.	0.007 s	[51]
	20	1 mm	Vibr.	0.007 s	[52]

* Str., Temp. and Vibr. stand for strain, temperature and vibration, respectively.
** The FBG refers to dense long-length FBG array.
† Yokogawa Electric Corporation, AQ8603
‡ Neubrex, Neubrescope NBX-6000
○ Luna Innovation, OBR4600

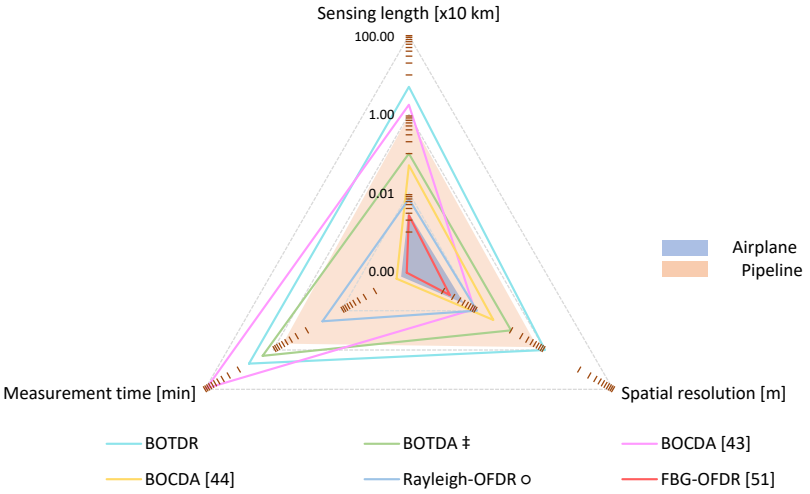

Fig. 3.12. Performances of selected distributed fiber-optic sensors: sensing length, spatial resolution and single measurement time. (logarithmic scale)

proper for the airplane, while the Brillouin based ones are more preferred for the bridge.

3.4 Multi-Parameter Distributed Fiber-optic Sensor

Multi-parameter sensors are always valuable in order to improve the information collection capabilities of the sensors. For distributed/quasi-distributed systems, a ratio named as effective information density, can be briefly defined as

$$\rho_{\text{info}} = \frac{n_{\text{par}} \Delta z_{\text{sp}}}{\Delta z_{\text{rng}}}, \tag{3.18}$$

where n_{par} is the number of measurable parameters, Δz_{sp} is the spatial resolution, and Δz_{rng} is the maximum measurement length (sometimes called dynamic range). For some DOFS, another index called effective sampling points is used [42, 43]. By enabling a distributed system for multi-parameter, the collected information will be increased by several times. This might improve the overall efficiency regarding the whole SHM system.

Although much more parameters are available for types of OFSs (strain, stress, pressure, temperature, refractive index, pH, etc.) [53–55], in terms of DOFSs, at current stage, the mostly developed multi-parameter ones are for strain and temperature [27]. Currently, approaches have been reported in Brillouin, Rayleigh and FBG based categories. For Brillouin scattering based DOFSs, Hotate's group made various efforts, including the combination of measurements of stimulated Brillouin frequency shift and the birefringence changes (based on Brillouin dynamic gratings) [56–58]. For basic Brillouin time domain techniques, 1 m was considered as the spatial resolution limit that is difficult to realize the strain-temperature discrimination with such high spatial resolution by time domain techniques. Meanwhile, by combining the Rayleigh and Brillouin scattering, the discrimination of strain and temperature was achieved by Bao's group [59]. The principle of such a system is applying a BOTDA and Rayleigh-OFDR to the strain and temperature variation at the same time. Since the fundamental phenomena and modulation principles are different, in the approach, actually there are two sets of sensing systems applied. Moreover, the simultaneous strain and temperature measurement have also be demonstrated by using long-length FBG-OFDR based on PM fibers by *Wada et al.* (our group) [60]. In this method, FBGs were inscribed into a PM fiber, and realized the strain and temperature discrimination by the birefringence induced different sensitivities to strain and temperature. This plan is also adopted as part of this research for studying the fundamental sensing properties and developing enhanced approaches which will be introduced in Section 6.3. In addition to the strain and temperature, vibration is also a very attractive measurand for researchers [1, 27]. Currently, there are some emerging techniques trying to combine vibration and strain/temperature sensor. For example, Li *et al.* recently (2018) reported an integration of Φ-OTDR and ultra-short FBG array for an almost fully distributed vibration sensing and quasi-distributed strain or temperature sensing [61]. In this approach, the strain and temperature were not discriminated. In this research, the measurands of interest are also strain and temperature, but the target is to achieve the discrimination of strain and temperature distribution for the first stage and then realize vibration sensing based on the same interrogation platform. Of course, other than OTDR, the basic principle of this research is OFDR based for their excellent advantages for middle scale (tens of meters) structural monitoring.

3.5 Fiber-Optic Sensors in Structural Health Monitoring

As introduced in Chap. 2, the emerging technology, SHM, aiming to assess the structural safety and operational conditions in the transportation, infrastructure, energy, etc., are getting more and more popular, although conventional electrical sensors are able to serve for most SHM applications. In the last few decades, OFSs have made a significant entrance in the sensor panorama [11]. Their advantages such as small, passive, electricity independent in sensing parts, and immune to electromagnetic interference that have large potentials to become the promising technologies in SHM [17, 20, 62]. Practically, the OFSs have been broadly explored in diverse fields, such as civil engineering, aerospace and aviation industry, oil and gas industry, naval architecture and ocean technology. This part will briefly introduce the current applications of OFSs in SHM.

- **Civil Engineering:** The great majority of OFSs applied in the civil engineering area is constituted by point/quasi distributed sensors such as FBG. Additionally, the fully distributed sensors offer more convenient installation and monitoring solution that are also being explored. In past few decades, some different DOFSs applications were made in different civil engineering structures such as bridges, dams, tunnels, pipelines and slopes [63, 64]. Bridges, especially concrete bridges, are the most monitored civil structures by OFSs. As early as 1993, Intelligent Sensing for Innovative Structures (ISIS, Canada) has equipped up to six bridges with OFSs that allow remote monitoring. In Japan, the SHM practice using FBG sensors (strain, temperature, acceleration) has also been performed on the Myoko-ohashi Bridge [65]. As for fully DOFSs, Rayleigh, Brillouin and Raman based systems have all been demonstrated in the monitoring of civil structures [64, 66–68]. For the usage in civil engineering, the OFSs are desired to have long measurement length.

- **Aerospace & Aviation Industry:** OFSs have also found their positions in the SHMs in aerospace/aviation. Aircraft SHM generally consists of several critical aspects, i.e., operational load monitoring, deformation/shape estimation and impact damage detection [2, 69]. To realize the monitoring, strain is the usual chosen parameter for load and shape sensing, while for impact damage the consequent acoustic emission is to be detected. Various studies have been reported regarding the deformation reconstructed from strain distribution. Systems based on FBG sensors for operational load monitoring are well established, developed and even commercialized [70, 71]. Regarding the shape sensing, one possible approach has been demonstrated using an inverse finite element method that relies on a least squares variational principle to predict the deformation shape of 3D plate and shell elements [72]. Kim H. *et al.* applied FBGs to investigate shape reconstruction for rotating structures [73]. Kim J. *et al.* conducted wing strain sensing by WDM of FBGs [74]. Kressel *et al.* applied FBG sensors to an unmanned aerial vehicle (UAV) for measuring strains of the wing and tail booms at high speed [75]. Saito *et al.* demonstrated Brillouin-based distributed sensing for the vertical tail of a business jet [76]. Wada *et al.* applied dense long FBG array and validated the fully distributed strain sensing on the fuselage [51]. These studies have successfully proven the applicability of the optical fiber sensing technique to aircraft flight monitoring. Furthermore, in the space, the European Space Agency has been investigating OFSs for several years and started the first operational spaceflight demonstrations in 2005 [77]. Notwithstanding, the applications of OFSs

in damage detection/monitoring are still at its early stage [71, 78], since this technique is based on the developing acoustic and ultrasonic NDT techniques. However, the emerging demands on directly monitoring of the crack existence and growth have stimulated the relevant researches. For the sensors applied to aircrafts/spacecrafts, they are desired to be stable, robust, compact, and have high information density collection capability (sometimes refers to high spatial resolution).

- **Naval Architecture & Ocean Technology:** As reported, lots of OFSs have been researched for the SHM of ship hull and offshore structures, such as FBG, interferometer, Brillouin scattering based techniques. Murayama *et al.* applied OFSs to full-scale composite structures to monitor strain or temperature and in-service structural performance of sailing boats [79]. In the research, two kinds of OFSs based on Brillouin and Raman scattering were installed. The application of FBG technology has also been demonstrated. For example, FBG sensors were employed in a hull monitoring system developed under the composite hull embedded sensor system (CHESS) program to determine the stress and strain distributions in the hull due to wave loads at various sea states [80]. Majewska *et al.* used FBG on sailing ships which were surrounded by the harsh marine environment and exposed to long-term cyclic loadings [81]. Ren *et al.* demonstrated FBG sensor application in offshore platform monitoring [82]. Those sensors may serve as point, distributed sensors, or networks for the measurement of various parameters including strain, stress, pressure, temperature. Thanks to the rapid development of fiber-optic vibration sensors, NDT can also be achieved using fiber-optic methods [83, 84]. For large ship or offshore structures, the DVS/DAS have attracted lots of attention [27].

Chapter 4

FBG-OFDR Sensing System

Before introducing the advanced approaches developed for multi-parameter sensing, it is important to make an overall explanation of the key principles which the sensing system is based on. In Section 4.1, the sensing principle is introduced. The FBG-OFDR system applies dense long-length FBGs as sensing component and employs an auxiliary interferometer. Such an arrangement enables the large sweep range of the TLS that brings a sub-millimeter order spatial resolution. In order to analyze the sensing performances such as measurement range, resolution and accuracy, a numerical model which combines the sensing part, interrogation system, demodulation and calibration processes has been proposed and introduced in Section 4.2. For obtaining the reflection of long-length FBG, the transfer matrix method is employed (Section 4.2.1). By applying Monte Carlo method in the estimation of sensitivity coefficients and simulated sensing process, the accuracy/error analysis can be performed as introduced in Section 4.2.3.

4.1 Principle of the system

In this study, the sensing system is based on the FBG–OFDR arrangement and its derivative approaches. In Section 3.3, the principle of OFDR has been introduced briefly. In my research, the system employs long-length FBG as sensing component and OFDR as interrogator. Different from the setup in Fig. 3.10, an auxiliary interferometer is implemented, as shown in Fig. 4.1. Among the commercial TLSs, there are two common sweep modes, linear and sinusoidal, as shown in Fig. 4.2. In the linear swept TLS, the frequency or wavelength of the output light is tuned at a constant speed, while in the other one, the sweep process follows a sine or cosine function. Usually, compared to the linear sweep, sinusoidal sweep results in a higher repetition rate. As aforementioned, the linearity is essential for an accurate measurement. Specially, as expressed in Eq. (3.16), to achieve high spatial resolution, large sweep range is required that makes it important to keep the linear sampling condition. For both high spatial resolution and repetition rate of the system, the auxiliary interferometer is employed to re-sample the beat signals at wavenumber (frequency) domain. Assuming that the path difference between reflectors, R1 and R2, is L_{r}, the interference beat signal by PD1 can be expressed as

$$I_{\mathrm{PD1}} \propto \cos\left(2n_{\mathrm{eff}}L_{\mathrm{r}}k\right), \tag{4.1}$$

where $k = 2\pi/\lambda$ is the wavenumber. As shown in Fig. 4.3, by employing it as clock signal, the PD2 is triggered by the positive zero crossing detection. The corresponding sampling

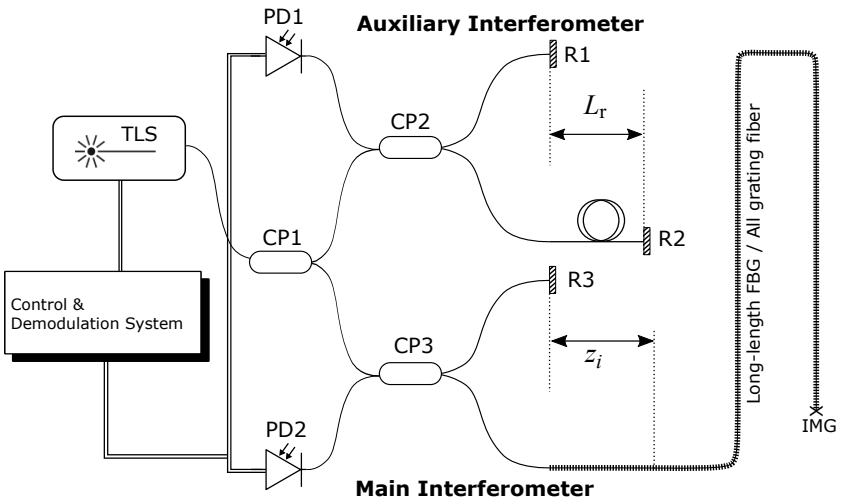

Fig. 4.1. Schematic of the long-length FBG–OFDR system. CP: coupler, PD: photodetector, R: reflector, IMG: index matching gel.

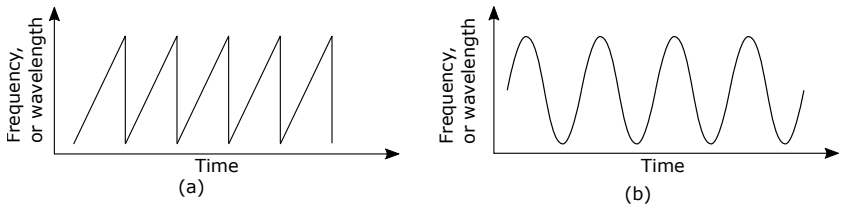

Fig. 4.2. Sweep modes of tunable laser source: (a) linear sweep, (b) sinusoidal sweep.

rate, determined by the path difference, is expressed as

$$\Delta k = \frac{\pi}{n_{\text{eff}} L_{\text{r}}}. \tag{4.2}$$

It is apparent that, this interval is always constant that will not be disturbed by the non-linearity of the TLS sweep. In this study, in-line long-length FBGs are applied as sensing part. Fig. 4.4 depicts the mechanism of their reflections. By dividing the whole FBG into small segments by the interval Δz_{g}, the reflected wave from the FBG can be regarded as the accumulation from each segment in distribution along the fiber. Thus, derived from Eq.

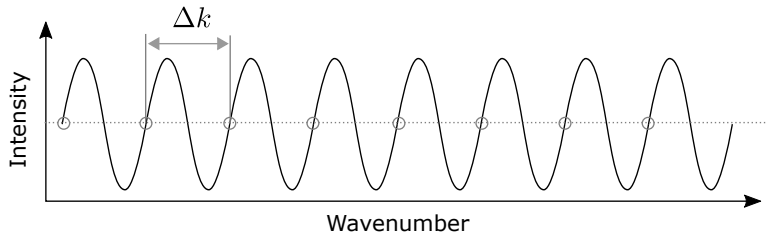

Fig. 4.3. Generated clock signal from PD1.

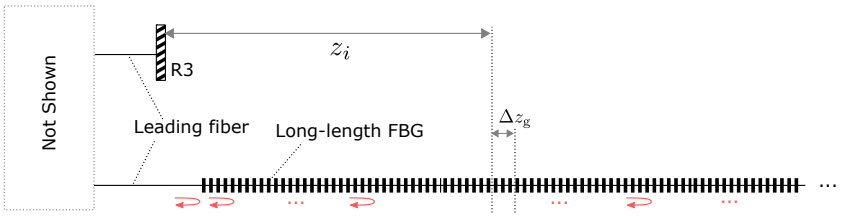

Fig. 4.4. Schematic of the distributed reflection of FBG.

(3.15), the beat signal by PD2 can be expressed as

$$I_{\mathrm{PD2}} \propto \sum_{i=1}^{N} R_{\mathrm{g}}\left(z_i, k\right) \cos\left(2 n_{\mathrm{eff}} z_i k\right), \tag{4.3}$$

where z_i is the relative position of the i^{th} FBG segment, R_{g} is the corresponding reflection profile which is the function of relative position and wavenumber. Since I_{PD2} is sampled at constant wavenumber interval, by applying Fourier transform to it, the reflection distribution at position domain can be revealed. From the Nyquist theorem, it is known that the maximum position of the FBG is limited by the L_{r} which is expressed as

$$z_{\max} < \frac{L_{\mathrm{r}}}{2}. \tag{4.4}$$

In this part, all the fluctuation of laser phases are ignored for convenience of explanation of sensing principle. For recovering the spatial distribution of FBG spectra, the beat signal, I_{PD2} is processed following the steps shown in flow chart, Fig. 4.5, the details of which will be introduced in Chapter 5.

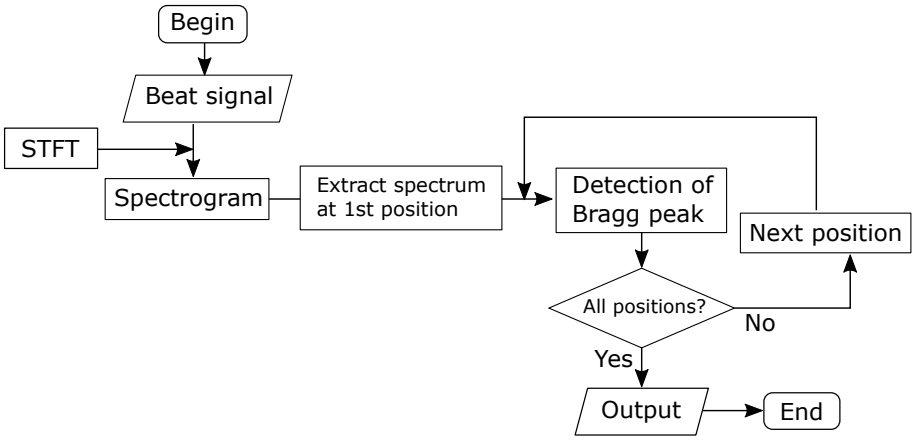

Fig. 4.5. Flow chart of the basic demodulation process. STFT: short time Fourier transform.

Additionally, a subgroup of the introduced FBG-OFDR system has been developed based on PM fibers, as shown in Fig. 4.6. In the system, 45° polarized light is injected into the PM fiber based main interferometer. Thus, 50% of the incident light is polarizing in the x direction while the rest is in the orthogonal direction. And this condition is maintained through the light propagation, ideally. By employing a polarization splitter before the photodetectors, PD2x and PD2y, the information from the fast and slow modes can be retrieved separately. Such an arrangement is especially valuable in PM-FBG based

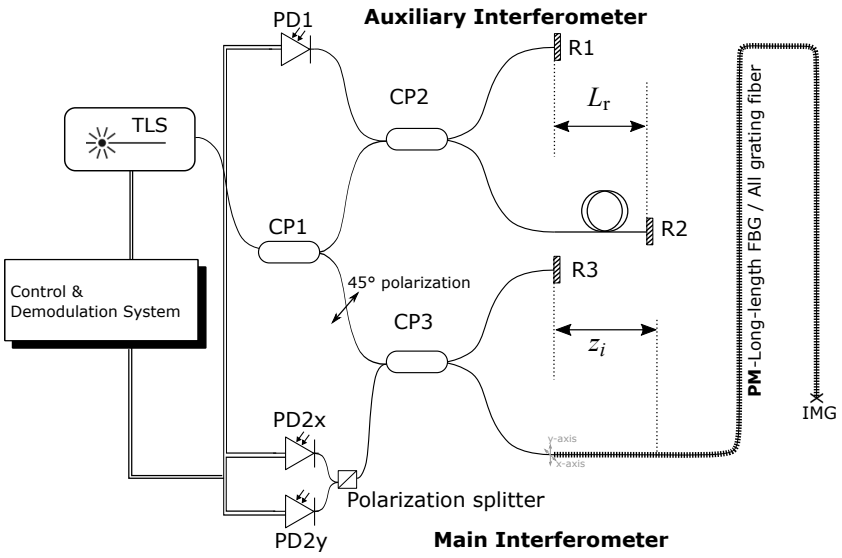

Fig. 4.6. Schematic of the polarization maintaining fiber based FBG-OFDR.

approaches which will be introduced in the next section.

4.2 Numerical Model

4.2.1 FBG-OFDR Simulation

FBG Reflection

For quantitatively obtaining spectral information of fiber gratings, a widely used and most straightforward tool is the coupled-mode theory [18, 19]. Also, it is intuitive, and it accurately models the optical properties of most fiber gratings. Here, in terms of Bragg grating, by defining the forward (reference) and backward propagating (signal) modes as R_{pr} and S_{pr}, respectively, the coupled-mode equations can be simplified as

$$\frac{dR_{\mathrm{pr}}}{dz} = j\hat{\kappa}_{\mathrm{dc}}R_{\mathrm{pr}}(z) + j\kappa_{\mathrm{ac}}S_{\mathrm{pr}}(z), \tag{4.5}$$

$$\frac{dS_{\mathrm{pr}}}{dz} = -j\hat{\kappa}_{\mathrm{dc}}S_{\mathrm{pr}}(z) - j\kappa^{*}_{\mathrm{ac}}R_{\mathrm{pr}}(z), \tag{4.6}$$

where κ_{ac} is the "ac" coupling coefficient, and $\hat{\kappa}_{dc}$ is the "dc" self-coupling coefficient defined as

$$\hat{\kappa}_{\mathrm{dc}} = \delta + \kappa_{\mathrm{dc}} - \frac{d\phi_{\mathrm{cp}}}{2dz}, \tag{4.7}$$

where κ_{dc} is the "dc" coupling coefficient. δ is the the detuning which is expressed as

$$\begin{aligned}\delta &= \beta - \frac{\pi}{\Lambda} \\ &= 2\pi n_{\mathrm{eff}}\left(\frac{1}{\lambda} - \frac{1}{\lambda_{\mathrm{D}}}\right).\end{aligned} \tag{4.8}$$

In the equation, $\lambda_{\mathrm{D}} = 2n_{\mathrm{eff}}\Lambda$ is the design wavelength for Bragg scattering. For a single mode FBG, the "dc" and "ac" coupling coefficients follow

$$\kappa_{\mathrm{dc}} = \frac{2\pi}{\lambda}\overline{\delta n}_{\mathrm{eff}}, \tag{4.9}$$

$$\kappa_{\mathrm{ac}} = \kappa_{\mathrm{ac}}^{*} = \frac{\pi}{\lambda}\upsilon_{\mathrm{frg}}\overline{\delta n}_{\mathrm{eff}}. \tag{4.10}$$

Analytically, the transfer matrix method, a piecewise-uniform approach, is efficient for simulating an FBG (uniform or non-uniform) with the length L_{g}. Figure 4.7 illustrates that the whole grating is divided into N segments. For the i$^{\mathrm{th}}$ segment, the corresponding

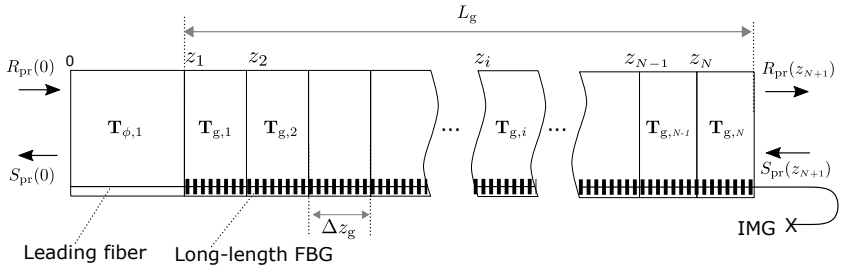

Fig. 4.7. Schematic of the transfer matrix method.

transfer matrix, $T_{\mathrm{g},i}$, is of the form

$$\mathbf{T}_{\mathrm{g},i} = \begin{bmatrix} \cosh(\gamma_{\mathrm{B}}\Delta z_{\mathrm{g}}) - j\frac{\hat{\kappa}_{\mathrm{dc}}\sinh(\gamma_{\mathrm{B}}\Delta z_{\mathrm{g}})}{\gamma_{\mathrm{B}}} & -j\frac{\kappa_{\mathrm{ac}}\sinh(\gamma_{\mathrm{B}}\Delta z_{\mathrm{g}})}{\gamma_{\mathrm{B}}} \\ j\frac{\kappa_{\mathrm{ac}}\sinh(\gamma_{\mathrm{B}}\Delta z_{\mathrm{g}})}{\gamma_{\mathrm{B}}} & \cosh(\gamma_{\mathrm{B}}\Delta z_{\mathrm{g}}) + j\frac{\hat{\kappa}_{\mathrm{dc}}\sinh(\gamma_{\mathrm{B}}\Delta z_{\mathrm{g}})}{\gamma_{\mathrm{B}}} \end{bmatrix}, \tag{4.11}$$

where γ_{B} is calculated as

$$\gamma_{\mathrm{B}} = \sqrt{\kappa_{\mathrm{ac}}^2 - \hat{\kappa}_{\mathrm{dc}}^2}. \tag{4.12}$$

The phase shift caused by leading fiber is introduced using matrix

$$\mathbf{T}_{\phi,1} = \begin{bmatrix} \exp\left(-j\frac{\phi_1}{2}\right) & 0 \\ 0 & \exp\left(j\frac{\phi_1}{2}\right) \end{bmatrix}, \tag{4.13}$$

where the phase term ϕ_1 is

$$\phi_1 = \frac{4\pi n_{\mathrm{eff}}}{\lambda}\Delta z_1. \tag{4.14}$$

Therefore, the light propagation in the fiber can be described as

$$\begin{bmatrix} R_{\mathrm{pr}}(0) \\ S_{\mathrm{pr}}(0) \end{bmatrix} = \mathbf{T}_{\mathrm{all}} \begin{bmatrix} R_{\mathrm{pr}}(z_{N+1}) \\ S_{\mathrm{pr}}(z_{N+1}) \end{bmatrix}, \tag{4.15}$$

where the $\mathbf{T}_{\mathrm{all}}$ is the production of the transfer matrix in sequence, which is expressed as

$$\mathbf{T}_{\mathrm{all}} = \begin{bmatrix} T_{11} & T_{12} \\ T_{21} & T_{22} \end{bmatrix} = \mathbf{T}_{\phi,1}\mathbf{T}_{\mathrm{g},1}\mathbf{T}_{\mathrm{g},2}\ldots\mathbf{T}_{\mathrm{g},z_N}. \tag{4.16}$$

Considering that the FBG is a reflection grating, when the incident light is only from the left to the right, the boundary condition can be set to be $R_{\mathrm{pr}}(0) = 1$ and $S_{\mathrm{pr}}(z_{N+1}) = 0$.

Thus, the reflection is obtained as

$$S_{\mathrm{pr}}(0) = \frac{T_{21}}{T_{11}}. \tag{4.17}$$

In the case of PM fiber, an orthonormal basis $\langle \hat{\mathbf{x}}, \hat{\mathbf{y}} \rangle$ is defined. Then, the transfer matrix should be rewritten as

$$\hat{\mathbf{T}}_{\mathrm{g},i} = \mathbf{T}_{\mathrm{gx},i} \cdot \hat{\mathbf{x}} + \mathbf{T}_{\mathrm{gy},i} \cdot \hat{\mathbf{y}}, \tag{4.18}$$

$$\hat{\mathbf{T}}_{\phi,i} = \mathbf{T}_{\phi\mathrm{x},i} \cdot \hat{\mathbf{x}} + \mathbf{T}_{\phi\mathrm{y},i} \cdot \hat{\mathbf{y}}, \tag{4.19}$$

where $\mathbf{T}_{\mathrm{gx},i}$, $\mathbf{T}_{\mathrm{gy},i}$, $\mathbf{T}_{\phi\mathrm{x},i}$ and $\mathbf{T}_{\phi\mathrm{y},i}$, should be calculated for the fast and slow mode separately, by considering the properties of PM fiber as introduced in Chapter 3. For the same reason, the reflection of PM-FBG is of the form

$$\hat{\mathbf{S}}_{\mathrm{pr}}(0) = \frac{T_{\mathrm{x},21}}{T_{\mathrm{x},11}} \cdot \hat{\mathbf{x}} + \frac{T_{\mathrm{y},21}}{T_{\mathrm{y},11}} \cdot \hat{\mathbf{y}}. \tag{4.20}$$

Beat Signal

As aforementioned, the beat signal detected by PD2 is the interference of the reflection of R3 and FBG. Just use single mode fiber for example. Assuming that the one way path of R3 is L_{R3}, the reflection wave is expressed as

$$E_{\mathrm{R3}} = E_0 \exp(2n_{\mathrm{eff}} L_{\mathrm{R3}} k + \pi) \tag{4.21}$$

Thus, the beat signal is obtained as

$$I_{\mathrm{PD2}} = \left(S_{\mathrm{pr}}(0) + E_{\mathrm{R3}}\right) \left(S_{\mathrm{pr}}(0) + E_{\mathrm{R3}}\right)^* \tag{4.22}$$

Results

In order to demonstrate the performance of the simulation, a single mode FBG with the properties shown in Table 4.1 is defined. By using the numerical model introduced here, the FBG spectrum, beat signal and spectrogram are obtained as shown in Fig. 4.8.

Table 4.1. Parameters of the long-length single mode FBG in simulation.

Parameter	Value
n_{eff}	1.45
Λ	534.48 nm
υ_{fg}	0.394
κ_{ac}	$1.42\,\mathrm{m}^{-1}$
L_{r}	2 m
L_{g}	100 mm
z_0	1.4 m
L_{R3}	1.0 m
TLS sweep range	1546 $\sim$ 1555 nm

Additionally, a PM-FBG was simulated using the parameters given in Table 4.2. The corresponding spectrum, beat signal and spectrogram are shown in Fig. 4.9.

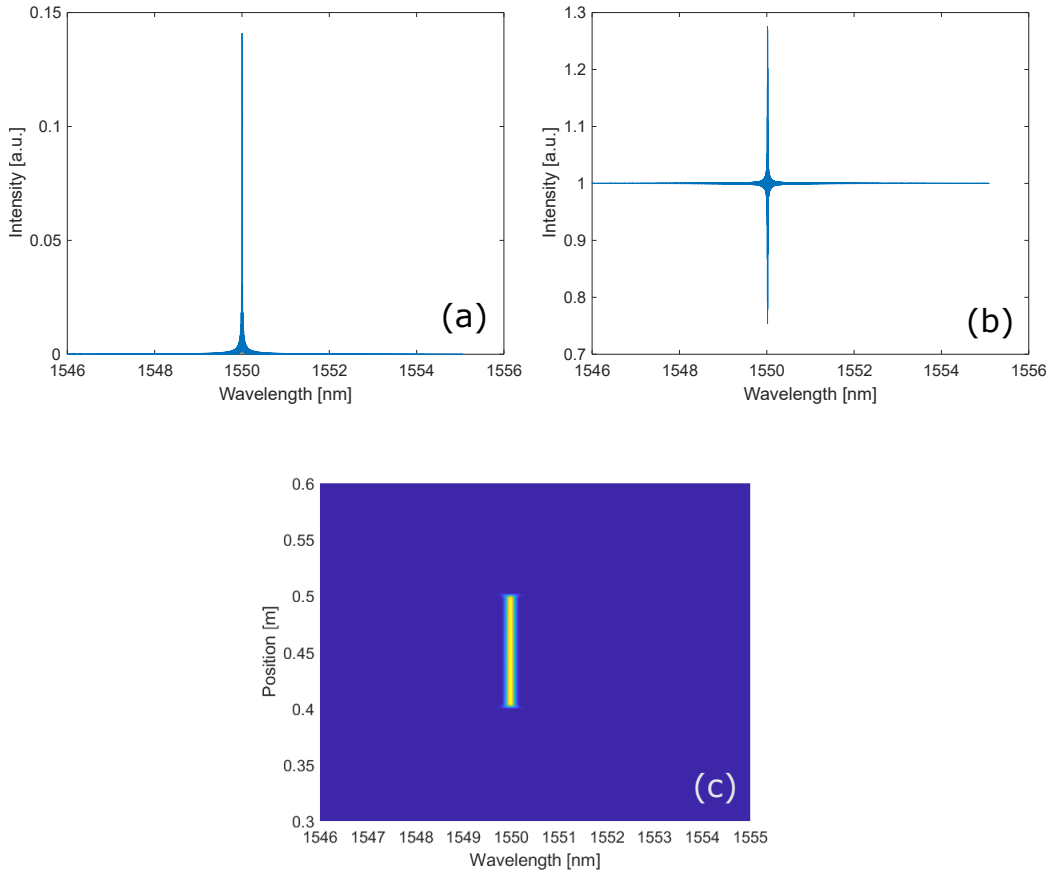

Fig. 4.8. Simulated long-length single mode FBG: (a) FBG spectrum, (b) beat signal and (c) spectrogram.

Table 4.2. Parameters of the long-length PM-FBG in simulation.

Parameter	Value
n_{eff}	1.45
B	8.5×10^{-4}
Λ	534.48 nm
υ_{fg}	0.394
κ_{ac}	$1.42\,\text{m}^{-1}$
L_{r}	2 m
L_{g}	100 mm
z_0	1.4 m
L_{R3}	1.0 m
TLS sweep range	1546 $\sim$ 1555 nm

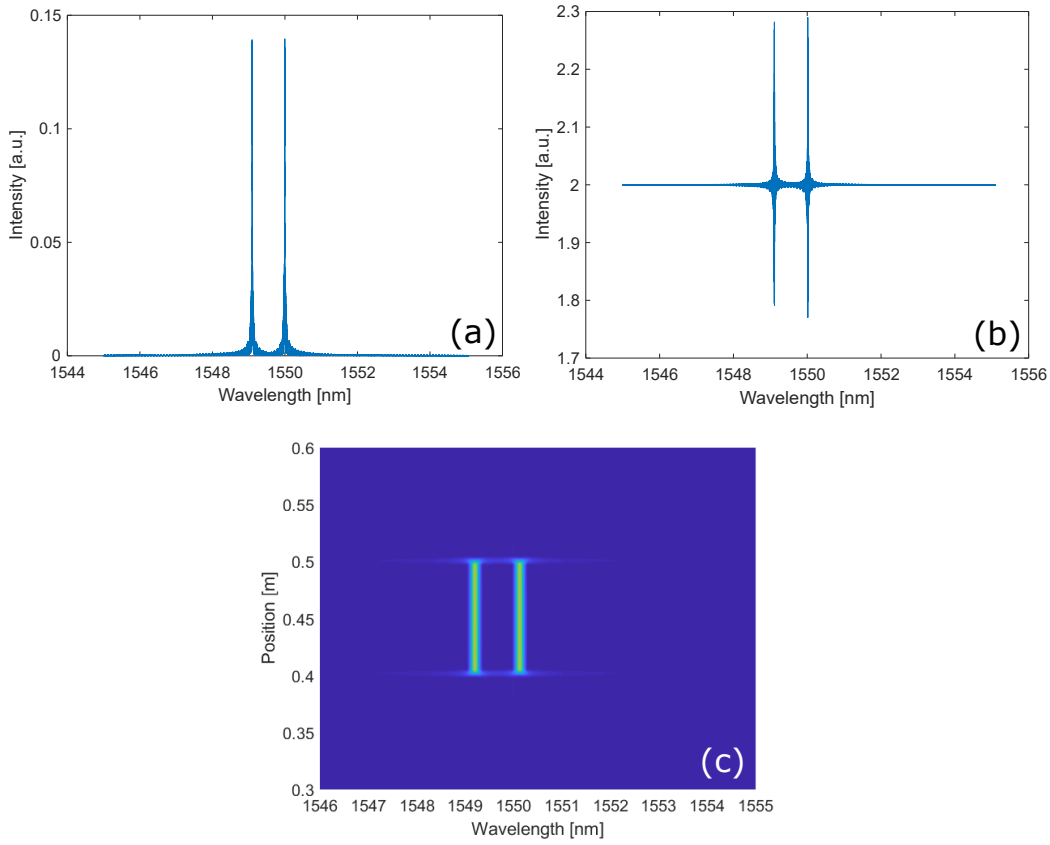

Fig. 4.9. Simulated long-length PM-FBG: (a) FBG spectrum, (b) beat signal and (c) spectrogram.

4.2.2 Calibration Simulation

In this study, the numerical model is supposed to simulate not only the sensing component and system, but the whole process of the measurement conducted using FBG-OFDR system. Thus, a proper simulation of the sensor calibration is essential as well. In this study, all the proposed sensors are applied for the measurement after calibrated through the following steps:

- **Apply temperature**: set initial strain to 0 με, change temperature from 50 °C to 100 °C by the interval of 10 °C. During the temperature increase, the strain is kept 0 με. Record the applied temperatures and measured central wavelengths.
- **Apply strain**: keep the temperature constant at room temperature (∼ 25 °C), and apply the tensile strains from any positive value by the interval of ∼ 50 με. Record the applied strains and measured central wavelengths.
- **Linear regression**: estimate the sensitivity coefficients for temperature and strain by applying linear fitting to the "wavelength vs. temperature" and " wavelength vs. strain" plots.

For the FBG in a standard optical fiber with circular cross section, the variation of axial strain and environmental temperature will have the most direct influence to its effective

refractive index and grating pitch, which can be expressed as

$$\Delta n_{\text{eff}} = -\frac{n_{\text{eff}}^3}{2}\left[P_{12} - \nu(P_{11} + P_{12})\right]\Delta\varepsilon + \frac{dn}{dT}\Delta T, \tag{4.23}$$

$$\Delta\Lambda = \Lambda\Delta\varepsilon + \Lambda\alpha\Delta T, \tag{4.24}$$

where ν is the Poisson's ratio, $P_{11,12}$ is Pockel's coefficients, α is the thermal expansion coefficient, dn/dT is the thermo-optic coefficient, respectively. To make a clear explanation, a short FBG is simulated using the parameters in Table 4.3. Considering that for silica fiber,

Table 4.3. Parameters of the short FBG in simulation.

Parameter	Value
n_{eff}	1.45
Λ	534.48 nm
υ_{fg}	1
κ_{ac}	$606\,\text{m}^{-1}$
L_{g}	2 mm
α	$5.5 \times 10^{-7}\,^{\circ}\text{C}^{-1}$
dn/dT	$8.95 \times 10^{-6}\,^{\circ}\text{C}^{-1}$

$[P_{12} - \nu(P_{11} + P_{12})] \approx 0.209$, the shifted spectra of FBG can be simulated using the same transfer matrix method. Figure 4.10 shows the spectrum of an FBG and its shift under the variations of $+500\,\mu\varepsilon$ and $+10°\text{C}$. By detecting the peak shift, the strain and temperature

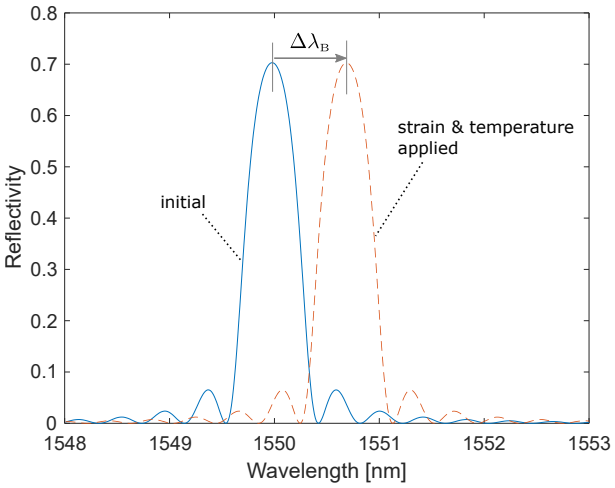

Fig. 4.10. Simulated spectrum shift of a short FBG.

induced Bragg wavelength can be estimated. By applying strains from 50 με to 500 με by the interval of 50 με and temperature changes from 10°C to 50°C by the interval of 10°C, the Bragg wavelengths are detected and processed through linear regression. As shown in Fig. 4.11, the numerical model made an effective simulation of the calibration process. In the figures, the slopes are defined as strain (K_ε) and temperature (K_T) sensitivities respectively. Note that the high order thermo-optic effect is ignored as in other FBG sensing researches [19, 20, 85]. This simplification is valid when the temperature variation is within 100°C at least.

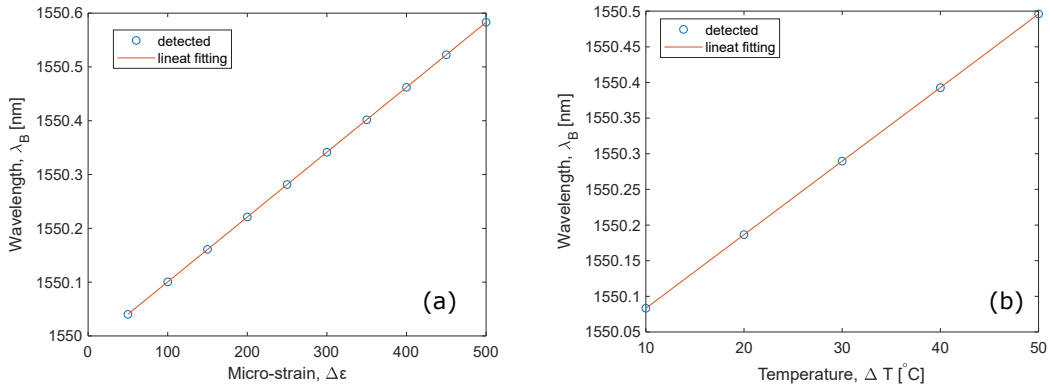

Fig. 4.11. Detected Bragg wavelength shifts with respect to (a) strain and (b) temperature in simulation.

4.2.3 Monte Carlo Method Based Accuracy/Error Estimation

Monte Carlo methods are a broad class of computational algorithms that rely on repeated random sampling to obtain numerical results. This method is also employed in this study for estimating the accuracy/error of proposed sensing approaches for strain and temperature measurement.

In order to feed the random errors, the clear identification of error source and error propagation is critical. In this study, the errors are originally from the noises of the OFDR system (mainly electrical noises and phase noises) and peak detection. Specially, in the calibration process, the monitored strain or temperature by reference sensor also induces errors in the process. As shown in Fig. 4.12, when ±3 pm of the wavelength sampling error and −45 dBm Gaussian noises (input power 0 dBm) are applied, the shift of the detected peak position will shift. Thus, by introducing the errors of reference sensors (±0.2 με and

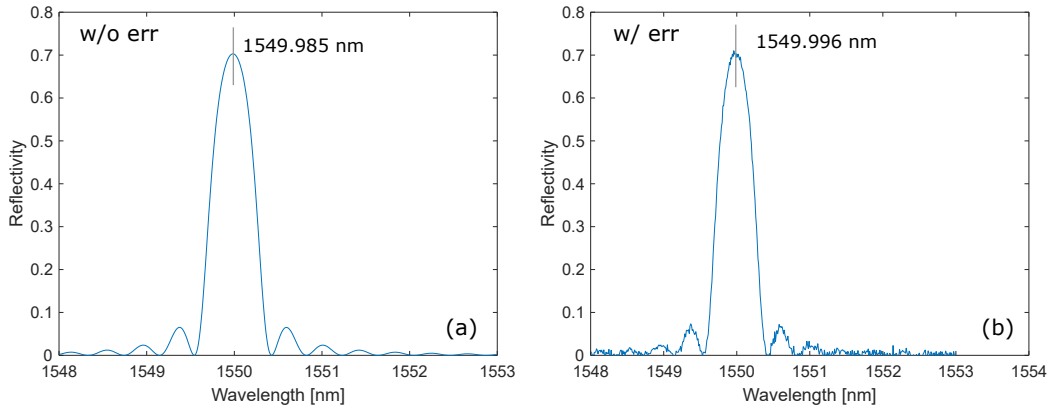

Fig. 4.12. Simulated FBG spectra with and without error.

±0.1°C) and repeating the calibration process, the linear regression is shown in Fig. 4.13. It is very clear that the errors in the scatters will result in the errors of the calibrated strain and temperature sensitivities. In the case of long-length FBG, the calibration process is the same, but in the simulation, the errors are firstly propagated to the beat signal instead of the spectrum, as shown in Fig. 4.14(a-b). Then the spectrograms are demodulated. Here the input error is also −45 dBm.

Figure 4.15 depicts the flow chart for a complete measurement. Firstly, the initial sensor

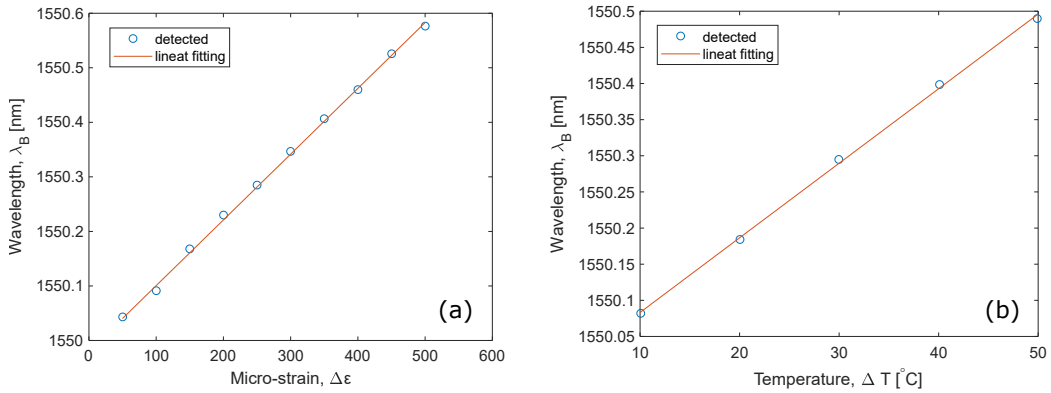

Fig. 4.13. Detected Bragg wavelength shifts with respect to (a) strain and (b) temperature in simulation with errors.

parameters are used to calculate the initial Bragg wavelength distribution obtained from the FBG-OFDR system. Then, the applied strain ($\Delta\varepsilon$) and temperature (ΔT) will change the effective refractive index, n_{eff}, and grating pitch, Λ. By using the Eqs. (4.23) and (4.24), the variated parameters, $n_{\text{eff}}^{'}$, and $\Lambda^{'}$ are obtained. After using the updated sensor parameters and introducing random errors, the simulated strain ($\Delta\varepsilon^{'}$) and temperature ($\Delta T^{'}$) with errors are further processed for error analysis. Note here that the estimation of K_ε and K_T with errors are realized using the aforementioned linear regression as illustrated by Fig. 4.13.

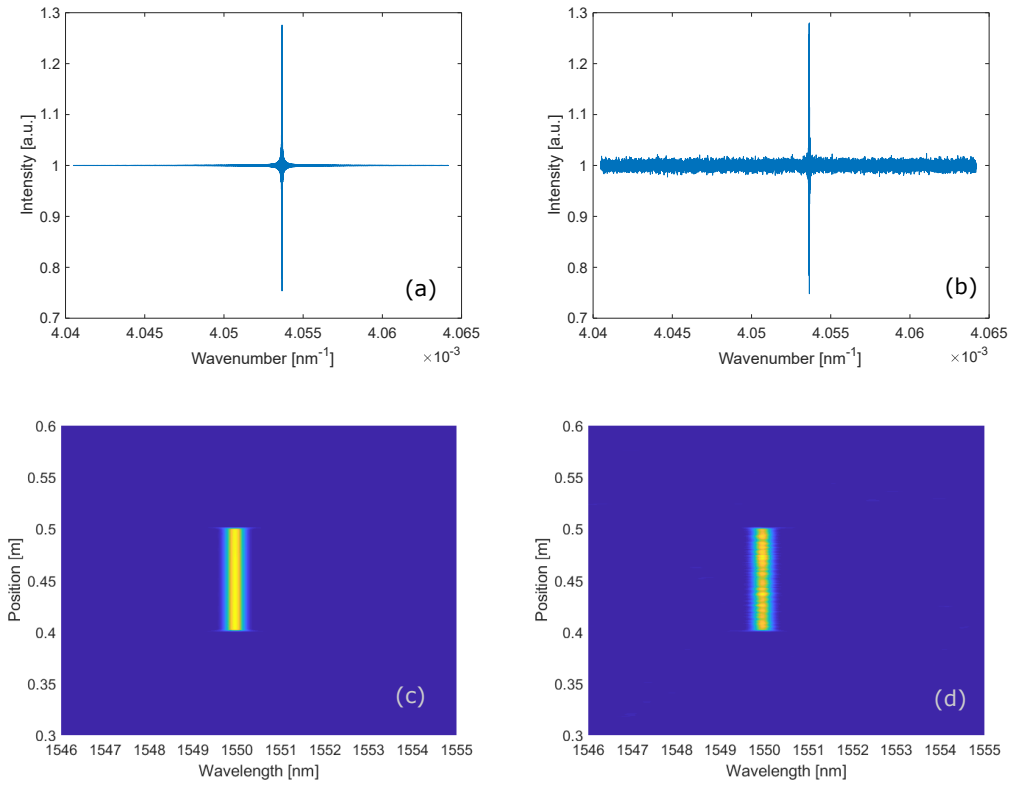

Fig. 4.14. Simulated long-length FBG with and without error: (a) beat signal without error,(b) beat signal with error, (c) spectrogram without error and (d) spectrogram with error.

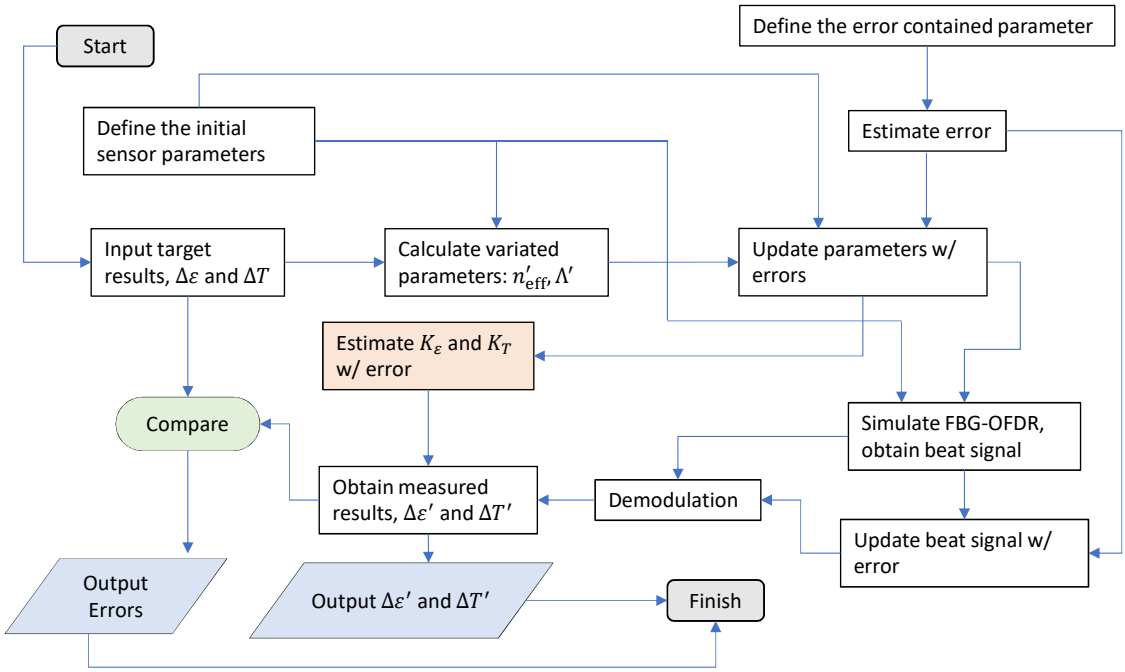

Fig. 4.15. The complete flow chart of the accuracy/error analysis model.

Chapter 5

Demodulations for Dynamic Distributed FBG-OFDR system

In the explanations of the FBG-OFDR sensing system, it has been briefly introduced that the Bragg wavelength shifts are demodulated from the detected beat signal by the photodetector PD2. Among the reported researches on relevant topics, there are two classic demodulation methods including the sliding band-pass filter and short time Fourier transform (STFT) based ones [37, 38, 86]. In general, these two methods work well for such OFDR based systems in static/quasi-static measurements, and show similar performances. However, at high spatial resolution and sampling rate, both methods require large amount of computational time and memory, which limit the applicability of such systems in dynamic measurements. In recent years, some approaches on fast demodulation have been reported. For example, the time-resolved OFDR for Rayleigh scattering [87], and Rayleigh-OFDR with fast processing algorithm for distributed acoustic sensing [88]. As for FBG-OFDR, a recent study introduced a fast demodulation algorithm by calculating the windowed group delay [89]. This method, introduced in Section 5.1.3, can remarkably reduce the computational time. However, the approach did not consider the noisy signal which is unavoidable in practical applications. In this study, we propose a fast demodulation process which is described in details in Section 5.2. This method mainly employs the cross correlation, fast Fourier transform (FFT), and more importantly, a newly designed thresholding function based on logistic activation function. As a result, this approach shows good measurement accuracy at noisy condition without sacrificing the spatial resolution and computing speed, which may further improve the applicably of this technology in real-time dynamic SHM.

5.1 Previously Reported Demodulation Approaches

5.1.1 Sliding Band-pass Filter Based Demodulation

The sliding band-pass filter based demodulation method is widely used in Rayleigh-OFDR systems [25, 26, 87]. Since the reflection of FBG is also elastic but with higher strength and limited in a selected linewidth, this method is also valid for FBG-OFDR system [38]. The process of this approach is depicted in Fig. 5.1. As shown, the acquired beat signal is firstly processed by an FFT to obtain the intensity of FBG as a function of position. In the distribution, the high intensity part of the length, L_g, is where the FBG locates. In the next step, a window (band-pass filter) is used to extract "local" intensity of a short segment

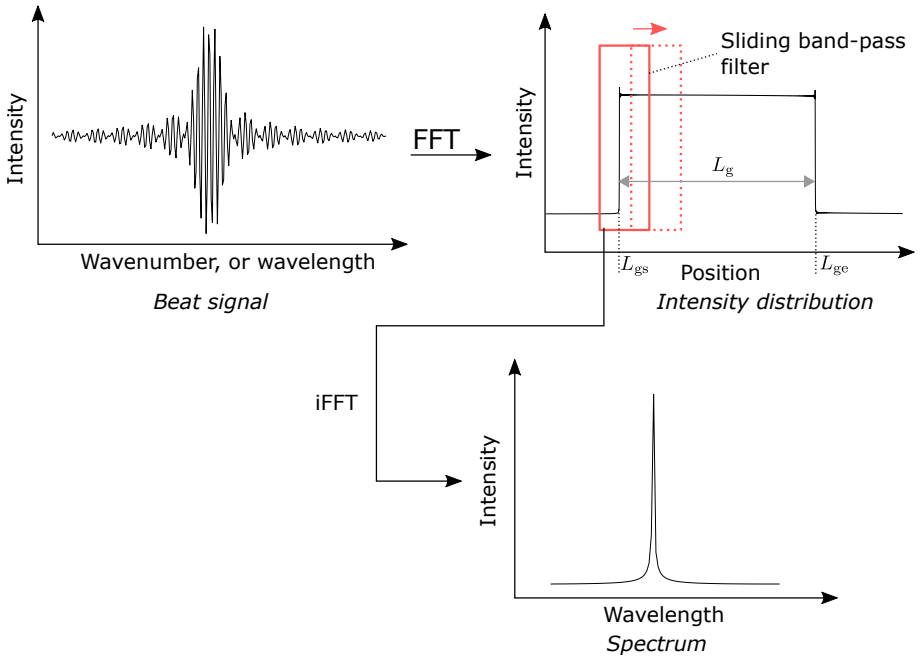

Fig. 5.1. Schematic of the band-pass filter based demodulation.

of FBG. After the calculation of inverse fast Fourier transform (iFFT), the spectrum of the FBG in corresponding segment is retrieved. In order to extract the spectra all along the position, we just need to slide the band-pass filter at position domain with a small step. The Bragg wavelength distribution is able to be detected with various method such as the mid-point of full width at half maximum (FWHM) and spectral centroid. By subtracting the initial Bragg wavelength distribution from the testing one, the desired distribution of Bragg wavelength shifts can be obtained. This method is very effective for sparse short FBG arrays, because the non FBG inscribed part can be clearly identified in the intensity distribution and skipped in the following processes. As shown in Fig. 5.2, the sliding band-pass filter is replaced by a hopping one.

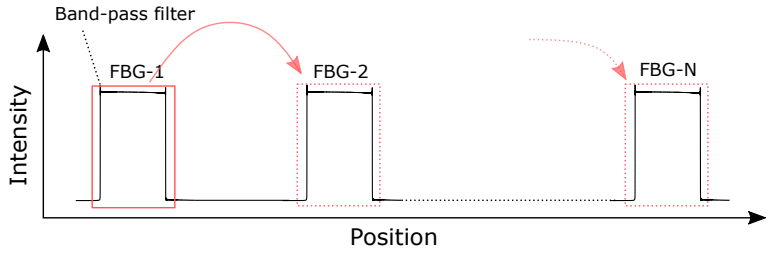

Fig. 5.2. Schematic of the hopping band-pass filter for sparse short FBG array.

5.1.2 Short Time Fourier Transform Based Demodulation

The STFT based demodulation was firstly introduced for demodulating dense long-length FBG array applied OFDR sensing systems [36, 37]. In this approach, instead of applying FFT to the beat signal, a STFT is employed. Typically, STFT is used to determine the sinusoidal frequency and phase content of local sections of a signal as it changes over time

[90]. In a more general use, it is actually retrieving the information scattering in one selected axis and its changes with respect to another orthogonal axis. In the case of OFDR, the eligible axes are position and wavenumber (or wavelength in this study). Therefore, the spectrogram represents the intensity distribution at spatial wavenumber domain, as shown in Fig. 5.3. From the spectrogram, it is easy to extract the optical spectra of the long-

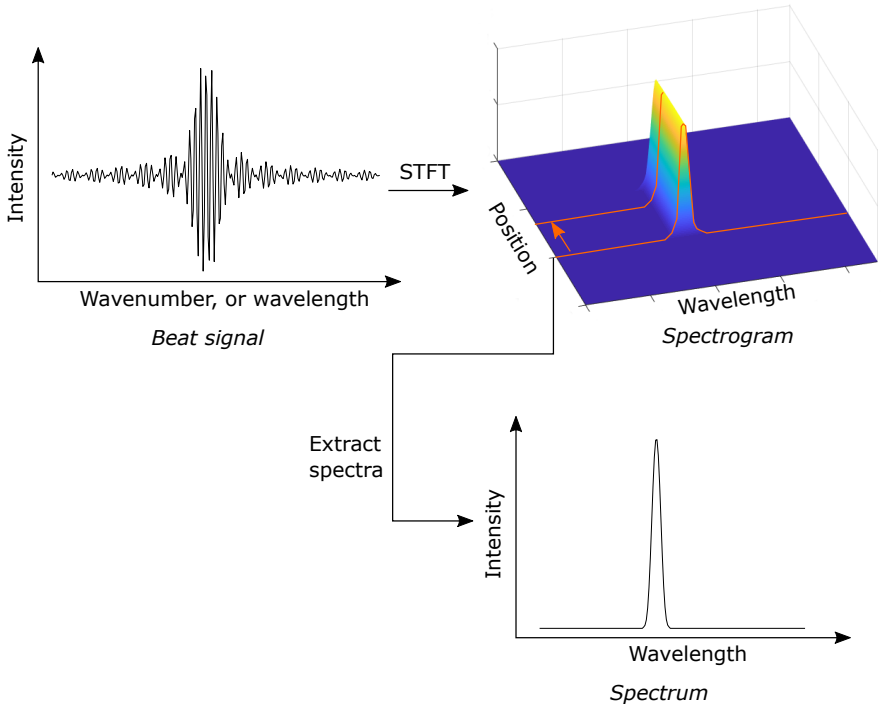

Fig. 5.3. Schematic of the short time Fourier transform based demodulation.

length FBG at each position and conduct further analysis. After converting wavenumber to wavelength, the Bragg wavelength distribution are detected by using the same methods as sliding band-pass filter based method. By subtracting the initial Bragg wavelength distribution from the testing one, the desired distribution of Bragg wavelength shifts can be obtained.

5.1.3 Group Delay Calculation Based Demodulation

The group delay is defined as a measure of the time delay experienced by narrow-band light pulses in an optical device. The group delay of an optical element can be measured in various ways. A conceptually most direct method is based on measuring the arrival times of ultrashort pulses. However, there are more powerful interferometric methods which allow the measurement of wavelength-resolved group delay with a precision of a few femtoseconds [89, 91]. For a piece of optical fiber, the group delay is mathematically calculated as

$$T_{\mathrm{g}} = \frac{\partial \phi}{\partial \omega}, \tag{5.1}$$

which is the derivative of the changes in spectral phase, ϕ, with respect ot angular frequency, $\omega = 2\pi f$. In this approach, the beat signal of both initial (I_{in}) and testing states (I_{ts}) are detected, then the impulse response $h(k)$ which is a function of wavenumber is calculated

by applying

$$I_{\mathrm{ts}}(k) = h(k) * I_{\mathrm{in}}. \tag{5.2}$$

Here, the $*$ denotes the convolution. By defining the frequency response of $h(k)$ as

$$H(e^{j\omega T_{\mathrm{smp}}}) = A(\omega)e^{j\omega T_{\mathrm{smp}}}, \tag{5.3}$$

the group delay can be calculated as

$$T_{\mathrm{g}} = -\mathrm{Im}\frac{dH}{Hd\omega} = -T_{\mathrm{smp}}\mathrm{Re}\left.\frac{zdH}{Hd\omega}\right|_{z=e^{j\omega T_{\mathrm{smp}}}}, \tag{5.4}$$

where T_{smp} is the sampling period [92]. Considering that $H(z) = \mathscr{F}[h(k)]$, the group delay can be derived to

$$T_{\mathrm{g}} = T_{\mathrm{smp}}\mathrm{Re}\frac{\mathscr{F}[kh(k)]}{\mathscr{F}[h(k)]}, \tag{5.5}$$

where $\mathscr{F}$ represents the Fourier transform. In order to reduce the noise of signal processing, the sliding window and weighted average is applied, obtaining

$$T_{\mathrm{g}}(z) = T_{\mathrm{smp}}\mathrm{Re}\frac{\sum \mathscr{F}\left[\hat{w}(m)\hat{k}\hat{h}\right]\mathscr{F}\left[\hat{w}(m)\hat{h}\right]^*}{\sum \mathscr{F}\left[\hat{w}(m)\hat{h}\right]\mathscr{F}\left[\hat{w}(m)\hat{h}\right]^*}, \tag{5.6}$$

where $\hat{w}(m)$ is the window function with the length of m. By assigning the the sampling period by Δk in Eq. (4.2), the desired the wavenumber shift, or corresponding Bragg wavelength shift can be obtained. This method can remarkably reduce the computational time compared with the STFT and sliding band-pass filter methods.

5.2 Fast Demodulation Using Activated Weighted Sliding Window Fourier Transform

5.2.1 Principle of Weighted Sliding Window Fourier Transform

In this part, a new fast demodulation method is introduced. Rather than applying cross correlation in the last step for the calculation of wavelength shift [25, 38, 87], it is directly calculated by using the reference and test signals using as

$$X(k) = I_{\mathrm{in}} \star I_{\mathrm{ts}} = \mathscr{F}^{-1}\left[\mathscr{F}(I_{\mathrm{in}})^* \cdot \mathscr{F}(I_{\mathrm{ts}})\right], \tag{5.7}$$

where $\star$ denotes the cross correlation, and $\mathscr{F}^{-1}$ is the inverse Fourier transform. Cross correlation is a standard method of estimating the degree to which two series are correlated which gives the lag of one signal to the other. In this application, it is proportional to the wavenumber shift. Thus, what we need to do is to extract the spatial information from such a accumulated shift. To achieve it, a weighted average and sliding window Fourier transform is applied. Mathematically, the distribution of wavenumber is expressed as

$$\Delta k_{\mathrm{D}}(z) = \frac{\sum_{i=1}^{N} k_i \left|\mathscr{F}\left[\hat{w}(m)\hat{X}_{k_i}\right]\right|^2}{\sum_{i=1}^{N} \left|\mathscr{F}\left[\hat{w}(m)\hat{X}_{k_i}\right]\right|^2}, \tag{5.8}$$

where $\hat{w}(m)$ is the window function of the length m, k_i is the central wavenumber of the i^{th} window, $\hat{X}_{k_i}$ refers the windowed segment of $X(k)$ at the same central wavenumber. Schematically, this process is depicted in Fig. 5.4. When applying Fourier transform to the

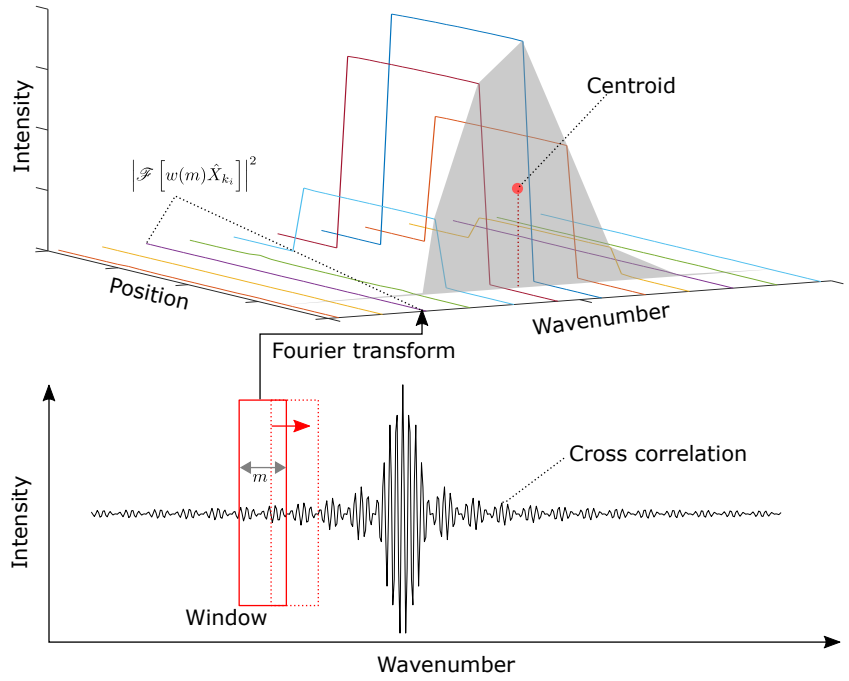

Fig. 5.4. Schematic of the fast demodulation based on weighted sliding windowed Fourier transform.

windowed segment of the cross correlated interference signal, $\hat{X}_{k_i}$, the corresponding intensity distribution of reflected light at position domain is obtained. By sliding the window through the wavenumber range of the TLS, the intensity distribution at each wavenumber can be obtained, forming a "spectrogram" like matrix. However, since only the wavenumber shift, referring to the horizontal coordinate of the centroid, is desired in this measurement, instead of obtaining the whole matrix, the wavenumber shift is directly retrieved using weighted average through the sliding window process. Considering that the Fourier transform of the windowed segment is an array at position domain, the desired distribution of wavenumber shift is acquired at once by Eq. (5.8). Thus, it is more efficient in the computational speed and memory use. This process is named as weighted sliding windowed Fourier transform (WWFT). In this research, the circular cross correlation, where FFT was used, was employed. With the sampling number of N_{s}, since the complexity of FFT is $O(N_{\text{s}}\log N_{\text{s}})$, it can be much more efficient than direct computation of linear correlation whose complexity goes as $O(N_{\text{s}}^2)$.

5.2.2 Logistic Activation Function Associated Thresholding

In the WWFT process, the noisy signal which is unavoidable in practice is not considered. Typically, a thresholding is used for the reduction of detection error. Although, denoising approaches such as moving average and low-pass filter are used in the post processing, they may reduce the spatial resolution at the same time. Thus, in this study, a novel fast thresholding process has been designed for improving the noise tolerance. One of the most

widely used thresholding applies the binary function. The hard thresholding is expressed as

$$r_{\text{bnr}} = \begin{cases} 0, & \text{if } s < \theta_{\text{thr}} \\ s, & \text{if } s \geq \theta_{\text{thr}}, \end{cases} \tag{5.9}$$

where s is the signal, θ_{thr} is the threshold, and r_{bnr} is the response, respectively. While the soft thresholding is expressed as

$$r_{\text{bnr}} = \begin{cases} 0, & \text{if } s < \theta_{\text{thr}} \\ s - \theta_{\text{thr}}, & \text{if } s \geq \theta_{\text{thr}}. \end{cases} \tag{5.10}$$

The response vs. signal curve is shown in Fig. 5.5. Since the soft thresholding which gives a smoother effect in the result, in this research, the soft thresholding is preferred.

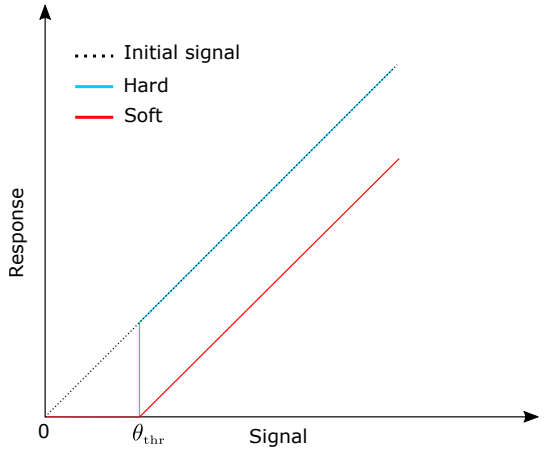

Fig. 5.5. Response of hard and soft thresholding based on binary function.

However, since the equation is not derivable at the threshold, θ_{thr} , large amount of "if functions" are necessary in the algorithm. Thus, the thresholding process will enormously increase the computational time. To address this issue, we propose a thresholding process based on the logistic activation function which is widely used in artificial neural networks [93]. The logistic function is expressed as

$$y = \frac{1}{1 + e^{-\eta_{\text{st}}(x - \theta_{\text{thr}})}}, \tag{5.11}$$

where η_{st} is the steepness of the curve, and θ_{thr} is the x-coordinate of the sigmoid's midpoint. The curve is shown in Fig. 5.6. By applying Eq. (5.11) as a multiplier, the soft thresholding based on can be built as

$$r_{\text{lgc}} = \frac{s - \theta_{\text{thr}}}{1 + e^{-\eta_{\text{st}}(s - \theta_{\text{thr}})}}, \tag{5.12}$$

of which the curve is shown in Fig. 5.7. It is apparent that in order to avoid negative responses in the thresholding, the steepness η_{st} should be large. In this research, it satisfies

$$\eta_{\text{st}} = 1 \times 10^3 \theta_{\text{thr}} > 0. \tag{5.13}$$

Usually in practical cases, the threshold ratio, θ_{rt}, which is a value within $0 \sim 100\%$ is used

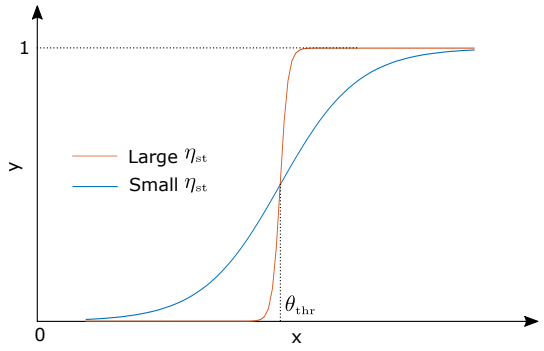

Fig. 5.6. Logistic function with different steepness.

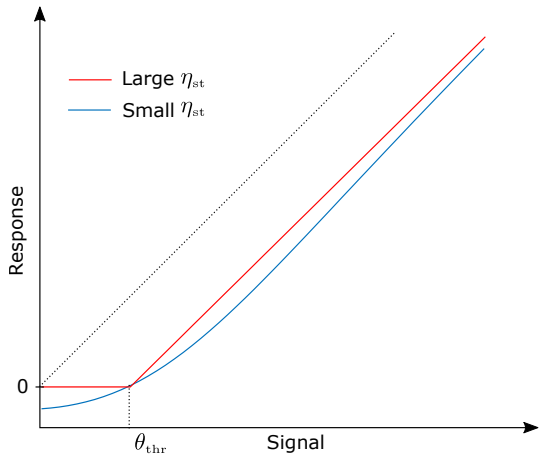

Fig. 5.7. Curve of logistic activation function based soft thresholding.

instead of threshold. The relation between them is of the form

$$\theta_{\mathrm{thr}} = \theta_{\mathrm{rt}} \left| \mathscr{F}(I_{\mathrm{in}})^* \cdot \mathscr{F}(I_{\mathrm{ts}}) \right|. \tag{5.14}$$

By inputting $s_i = \left| \mathscr{F}\left[\hat{w}\hat{X}_{k_i}\right] \right|$ as signal in Eq. (5.12), Eq. (5.8) can be derived to

$$\Delta k_{\mathrm{D}} = \frac{\sum_{i=1}^{N} k_i r_{\mathrm{lgc}}^2(s_i, \theta_{\mathrm{rt}})}{\sum_{i=1}^{N} r_{\mathrm{lgc}}^2(s_i, \theta_{\mathrm{rt}})}. \tag{5.15}$$

Note that r_{lgc} is the function of s_i and θ_{rt}. With the association of activation function, the demodulation is named as AWWFT. The wavenumber shift can be converted to wavelength distribution by

$$\Delta\lambda_{\mathrm{B}} = -\frac{\Delta k_{\mathrm{D}} \lambda_{\mathrm{s}} \lambda_{\mathrm{e}}}{2\pi}, \tag{5.16}$$

where λ_{s} and λ_{e} are the start and end of the wavelength sweep range of TLS, respectively. To avoid the confusion with FBG sensing principle where Bragg wavelength shifts are the most commonly used, all the wavenumbers are converted to wavelengths in this study. A simple distinction of WWFT and AWWFT is that AWWFT is the WWFT with implemented thresholding based on logistic activation function.

5.2.3 Demodulation Results

To demonstrate the demodulation performance of newly proposed approaches, WWFT and AWWFT, both simulation and experiments were performed. Since the spatial resolution of the OFDR used in this study is at millimeter/sub-millimeter order, 100 mm long-length FBG is enough for proving the concept. Thus, in the simulation, a three-step wavelength distribution is defined as

$$\lambda_{\mathrm{B,ts}} = \begin{cases} 1550\,[\mathrm{nm}], & L_s \le z < L_1, \\ 1551\,[\mathrm{nm}], & L_1 \le z < L_2, \\ 1552\,[\mathrm{nm}], & L_2 \le z \le L_e, \end{cases} \tag{5.17}$$

where L_s, L_e, L_1 and L_2 are the position of starting point, ending point and two singularities, respectively. z is the position on the FUT. The parameter values are given in Table 5.1 and 4.1. Considering the initial Bragg wavelength of the grating is 1550 nm, the obtained

Table 5.1. Parameter values in the simulation model.

Parameter	Value
L_{s}	400 mm
L_{e}	500 mm
L_1	433 mm
L_2	466 mm
Readout resolution, Δz_{rd}	0.1 mm
FBG segment number, N	500
Input power	1 mW

distribution of Bragg wavelength shift with and without noise is shown in Fig. 5.8. The introduced noise is -50 dBm. And the threshold ratio is 35%. From the results, it is clear that with the thresholding, AWWFT has shown effective denoising effect.

Additionally, the demodulation was performed experimentally. In the experiment, as shown in Fig. 5.9, a 100 mm FBG is bonded on the top surface of a cantilever. When load is applied to the free end, because of the hole drilled near the fiber, the strain concentration is expected to be detected. Using the approximation, $K_\varepsilon \approx 1.0\,\mu\varepsilon/\mathrm{pm}$, the retrieved strain distribution is plotted as shown in Fig. 5.10. The concentrated strain can be observed at about 345 mm. It is apparent that AWWFT shows much high tolerance to the noise in practical measurements. Here, the threshold ratio is set to be 35% while no extra random error is introduced. In addition, the size of the hole can be estimated using the FWHM after de-trending. As shown in Fig. 5.10(b), the solid red line is the trend. The estimated diameter of the hole is $\sim 5\,\mathrm{mm}$ which agrees with its actual size.

Optimization of Threshold

As mentioned, the key for improving the noise tolerance in AWWFT is the thresholding process. Thus, a proper threshold is crucial for the finial performance of the demodulation. Its value need to be optimized in terms of different application. In this study, the accuracy, or error of the measurement is estimated with root mean square deviation (RMSD), which

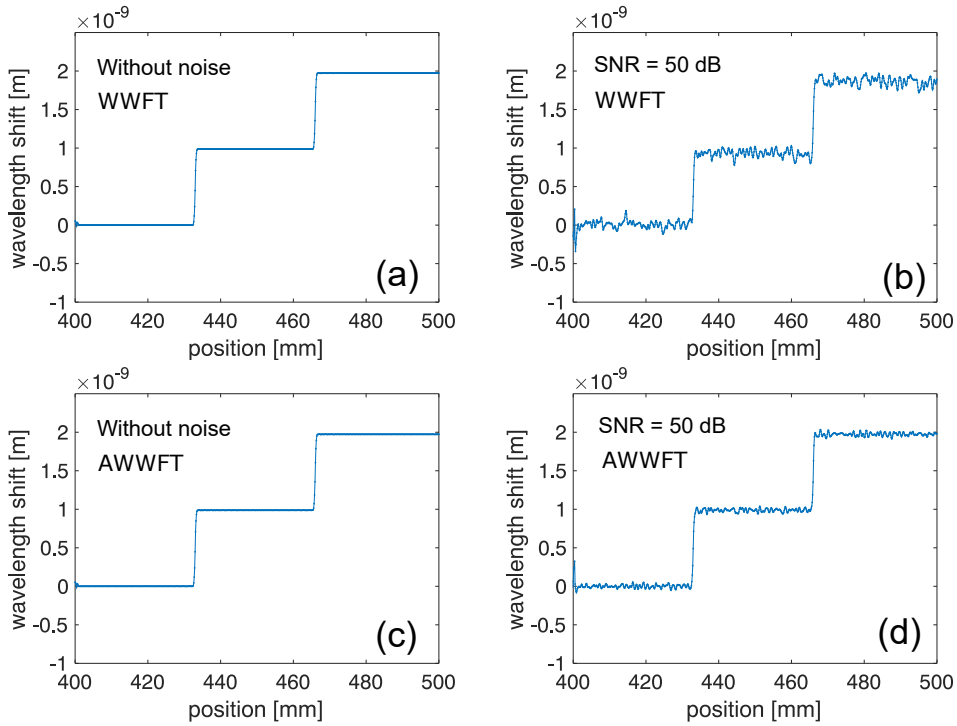

Fig. 5.8. Demodulated three step distribution by using WWFT and AWWFT: (a) WWFT demodulation without noise, (b) WWFT demodulation with noise, (c) AWWFT demodulation without noise, (d) AWWFT demodulation with noise.

is expressed as

$$\sigma_{\text{acc}} = \text{RMSD} = \sqrt{\frac{1}{N}\sum_{i=1}^{N}(x_{\text{ms},i} - x_{\text{ap},i})^2}, \tag{5.18}$$

where $x_{\text{ms},i}$ and $x_{\text{ap},i}$ are the i^{th} measured and applied value, respectively. For example, as shown in Fig. 5.11, if a uniform wavelength shift is applied to a segment of FBG, the RMSD of this segment can be used to represent the distributed measurement accuracy.

In practical applications, due to the noise, the spectral profile of the FBG reflection is usually not a perfect Gaussian shape. Figure 5.12(a) shows an acquired spectrum of wavelength shift as an example. Due to the varying Bragg wavelength and reflection strength, the multi-peak feature as well as the background noise can be observed. From the relation of accuracy vs. threshold ratio, as shown in Fig. 5.11(b), we can see that when the weak-threshold (Wk.T.) which is below the noise level is applied, the increase of threshold ratio can always result in better accuracy. Then, when the threshold reaches the waist of the spectrum, the obtained accuracy becomes relatively stable. This is the optimal-threshold (Op.T.) region. However, when it keeps increasing to the over-threshold (Ov.T.) region where multi-peak pattern occurs, there will be a sudden accuracy degradation. Although, after that, the accuracy appears to improve again, the measurement has already lost the actual profile of the spatial distribution. Thus, practically, to achieve accurate and reliable measurement, the threshold ratio should be in the Op.T. region. In this study, the chosen threshold ratio (35%) is in the optimal region. Please notice that in different sensing cases, the optimal threshold ratios need to be determined during the preparations before

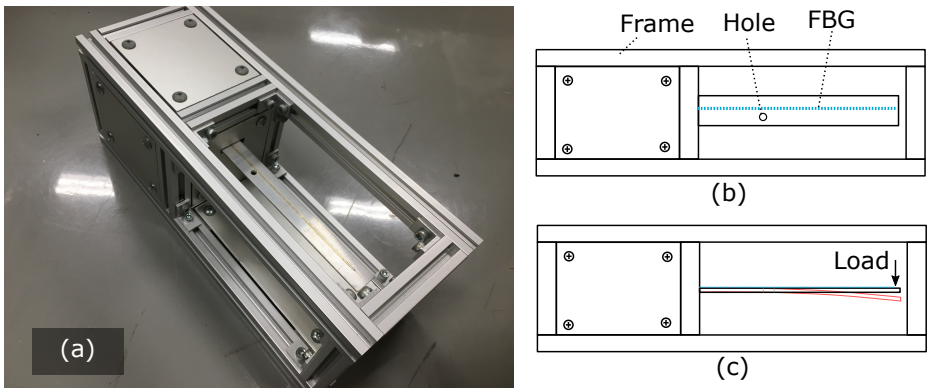

Fig. 5.9. Schematic of the experimental setup of a cantilever with a hole: (a) photo, (b) top view, (c) left side view.

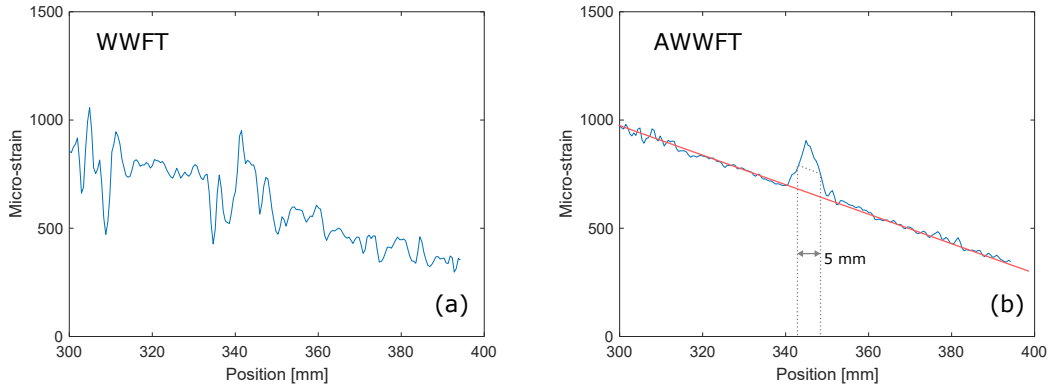

Fig. 5.10. Measured strain distribution of the cantilever using WWFT and AWWFT.

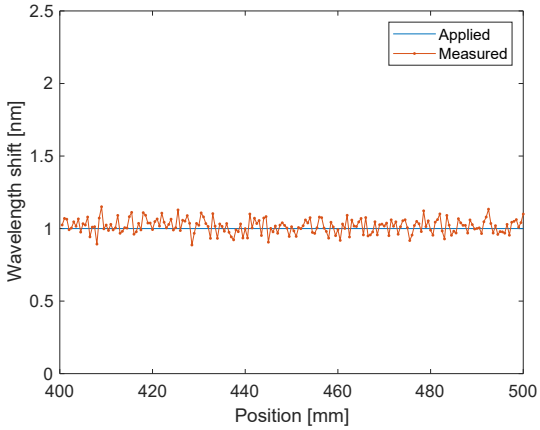

Fig. 5.11. Applied and measured uniform wavelength distribution.

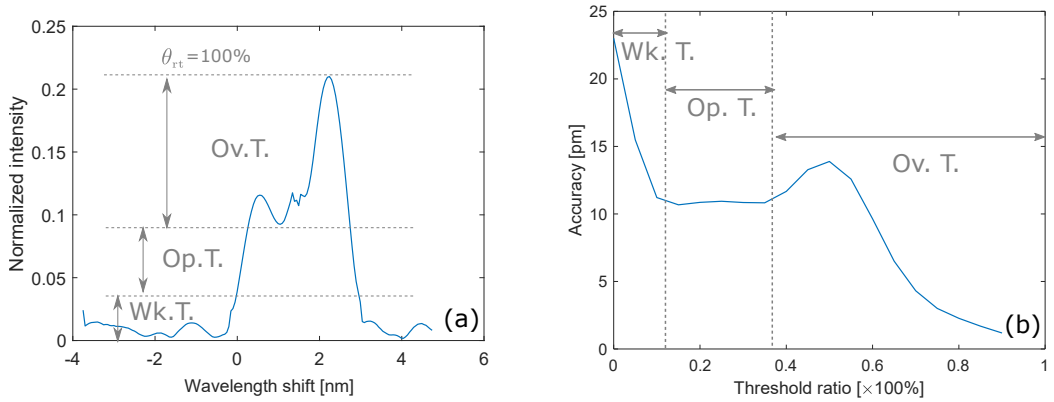

Fig. 5.12. (a) Acquired spectrum of FBG. (b) Accuracy vs. threshold ratio and various levels of threshold ratios.

the practical measurement.

5.3 Comparison of Different Demodulation Methods

To give an objective evaluation, we performed horizontal comparisons of methods based on STFT, group delay, WWFT and AWWFT by both simulation and experiment.

5.3.1 Simulation

In the simulation, the three-step distribution in Eq. (5.17) is applied to the FUT. Then the interference beat signal is demodulated by different methods. In all the methods, hamming window is selected, and the window length, step length and SNR are set to be 2 nm, 0.2 nm and 50 dB, respectively. The threshold ratio in the peak detection process of STFT based demodulation is set to be the same as in proposed AWWFT ($\theta_{\mathrm{rt}} = 35\%$). The demodulated distribution of all four methods are shown in Fig. 5.13. It is clear that in the STFT and AWWFT based methods, the accuracies are better than the other two. To compare the computational time of each method, relative time consumed is defined as

$$r_{\mathrm{t}} = \frac{t_{\mathrm{x}}}{t_{\mathrm{stft}}}, \tag{5.19}$$

which is the ratio of computational time of different methods to the computational time of STFT. The subscript x, referring to "stft, gp, wwft, or awwft", denotes the demodulation methods based on STFT, group delay, WWFT, or AWWFT, respectively. In this work, the total times are the time consumed by 100 times demodulation of each method. According to the results shown in Table 5.2, the conventional STFT method shows the best measurement accuracy (σ_{acc}), however, takes long time. The group delay based method takes much less time but shows the lowest accuracy. And the proposed fast demodulation method in this study keeps good balance in high speed and high accuracy. In all the methods, the spatial resolutions (Δz_{sp}) were defined as the 10% to 90% response distance of a pure step distribution, as shown in Fig. 5.14 [23, 37]. As shown in Table 5.2, they were achieved to be $\sim 0.3\,\mathrm{mm}$. As pure step distribution is simulated, the spatial resolution and response distance are identical. In this study, the comparison was conducted by Matlab® 2018a on the same computer (Intel® Core (TM) i7-3770 @3.4 GHz).

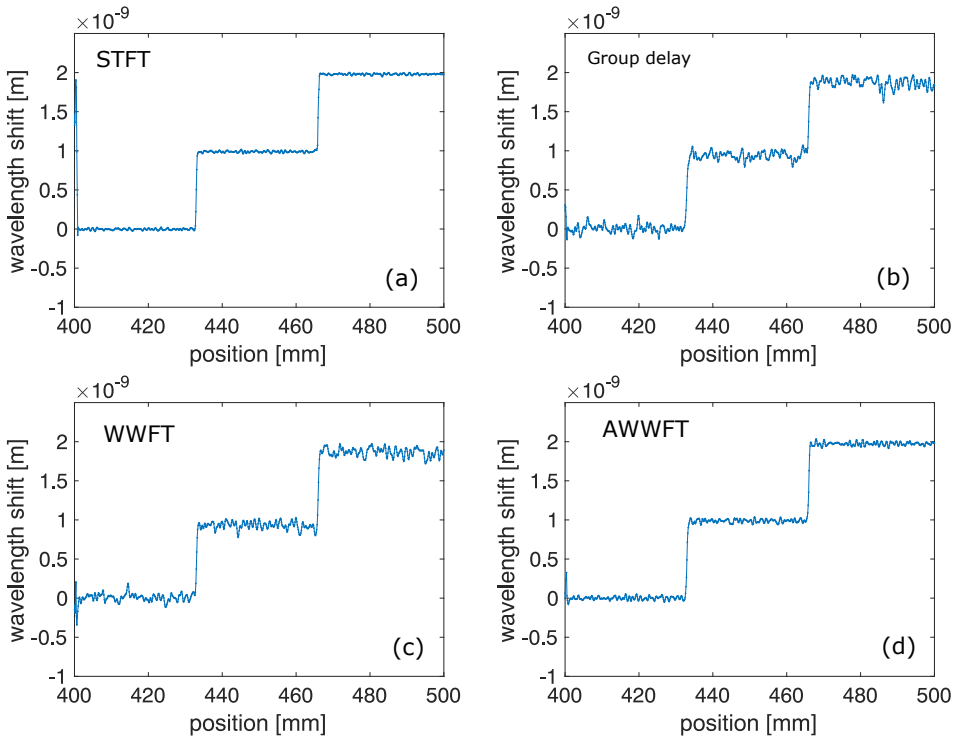

Fig. 5.13. Demodulation results of simulated three-step distribution: (a) STFT, (b) Group delay, (c) WWFT, and (d) AWWFT.

Table 5.2. Simulated comparison of different methods.

Parameter	STFT	Group delay	WWFT	AWWFT
Threshold ratio, θ_{rt}	35%	-	-	35%
Relative time, r_{t}	1.000	0.061	0.034	0.042
Accuracy, σ_{acc} [pm]	10.2	52.4	51.2	21.6
Spatial resolution, Δz_{sp} [mm]	0.3	0.3	0.3	0.3
Response distance [mm]	0.3	0.3	0.3	0.3

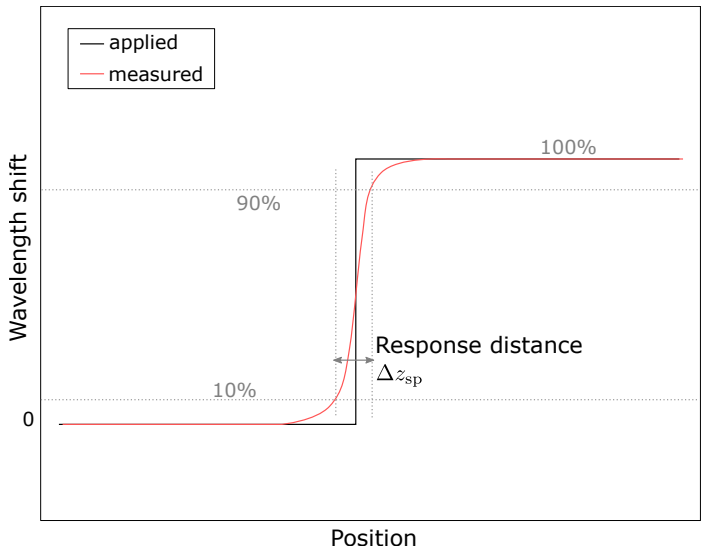

Fig. 5.14. Definition of spatial resolution.

5.3.2 Experiment

Experimentally, the three demodulation methods were also compared. An FBG with the length of about 100 mm was inscribed by using phase mask and UV light. The Bragg wavelength is $\sim$ 1551 nm at stress-free condition. As shown in Fig. 5.15(a), the FBG in the middle (green circle) was bonded to a steel wire which is fixed on a stationary stage. The diameter of the steel is $\sim$ 0.5 mm. Then one half of the grating (Fig. 5.15(a, b) right

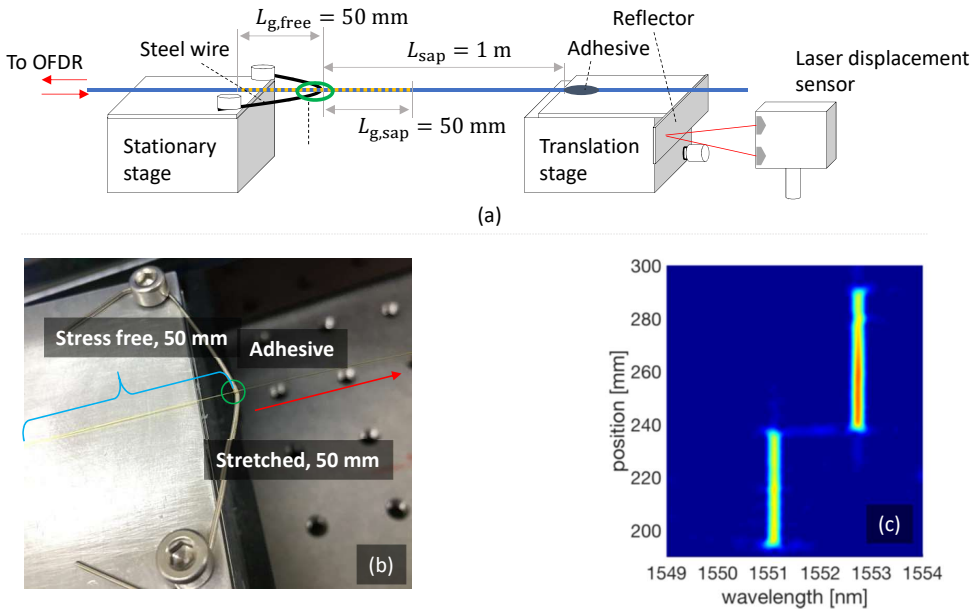

Fig. 5.15. Schematic of the experimental setup for applying two-step strain distribution. The adhesive spot diameter is about 0.7 $\sim$ 1.0 mm, and the accuracy of the laser displacement sensor is $\pm$0.2 µm.

hand side, $L_{g,sap} = 50$ mm) was stretched using a translation stage while the other half (left hand side, $L_{g,free} = 50$ mm) was left stress-free. The displacement of the translation stage was monitored by a laser displacement sensor whose accuracy is $\pm$0.2 µm. Considering the total length of stress-applied fiber, L_{sap}, is 1 m, the corresponding strain accuracy of the setup is $\pm$0.2 µε. Figure 5.15(b) shows the picture of FBG fixed area. The spectrogram of the FBG at that condition is shown in Fig. 5.15(c). The Bragg wavelength of stretched part is $\sim$ 1552.5 nm. Respectively, the STFT, group delay, WWFT, and AWWFT based methods were applied for the demodulation of which the results are shown in Fig. 5.16. In the experiment, the parameter settings are the same as in the simulation without adding extra noises. Because of the size of the adhesive spot (about 0.7 $\sim$ 1.0 mm), the applied distribution is not a pure step. Thus, the response distances are larger than the spatial resolutions in the experimental results. From the demodulated results shown in Fig. 5.16 and Table 5.3, the STFT and AWWFT based methods show similar performance regarding the accuracy, while the group delay and WWFT based method shows the lowest accuracy. In general, the experiment and simulation have shown good agreement in the conclusion that the AWWFT achieved high accuracy without slowing down the computational speed or degradation in spatial resolution.

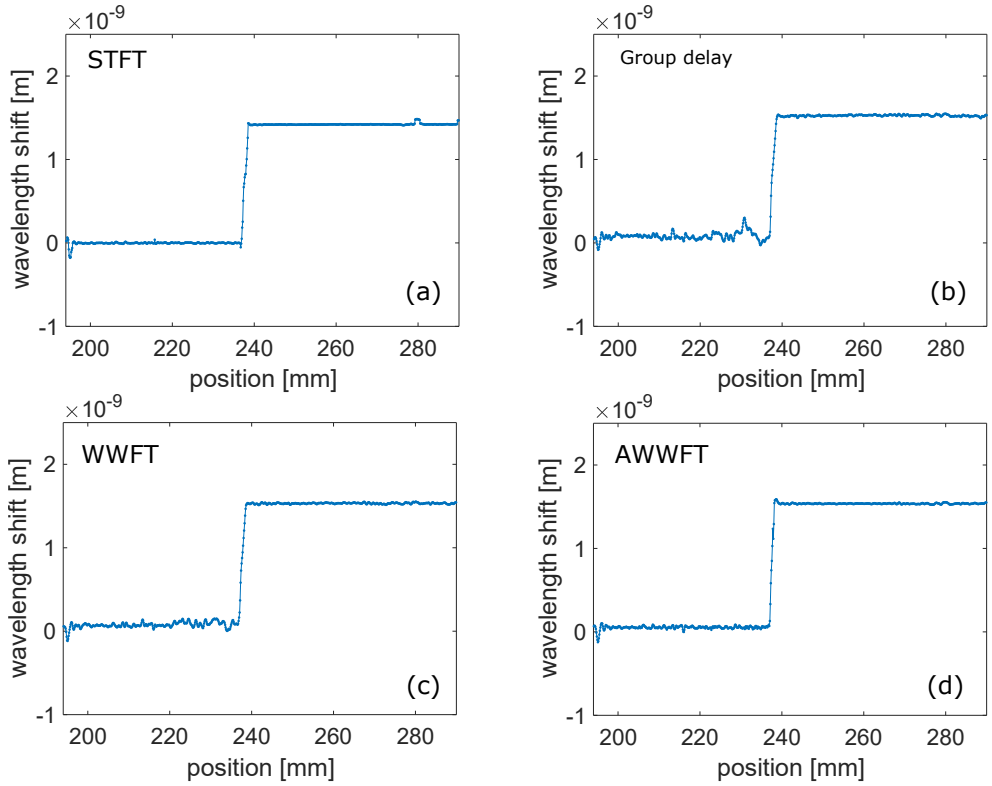

Fig. 5.16. Demodulation resutls of experimental two-step distribution:(a) STFT, (b) Group delay, (c) WWFT, and (d) AWWFT.

Table 5.3. Experimental comparison of different methods.

Parameter	STFT	Group delay	WWFT	AWWFT
Threshold ratio θ_{rt}	35%	-	-	35%
Relative time, r_{t}	1.000	0.061	0.034	0.042
Accuracy, σ_{acc} [pm]	8.9	24.2	23.6	11.2
Spatial resolution, Δz_{sp} [mm]	0.3	0.3	0.3	0.3
Response distance [mm]	1.1	1.1	1.1	1.0

5.3.3 Overall Comparison

To make the comparison more clear, the results in Tables 5.2 and 5.3 are plotted in two spider charts, as shown in Fig. 5.17. Regarding the application in real-time SHMs, the sensing systems are expected to perform with higher spatial resolution (smaller value), higher accuracy (smaller value) and shorter computational time, which refers to a smaller area in the spider charts. In both simulation and experiment, the smallest area was achieved by the proposed AWWFT method in this study. In addition, once the requirements for one specific application is given, the spider charts may provide an intuitive method for selecting the most efficient demodulation technique.

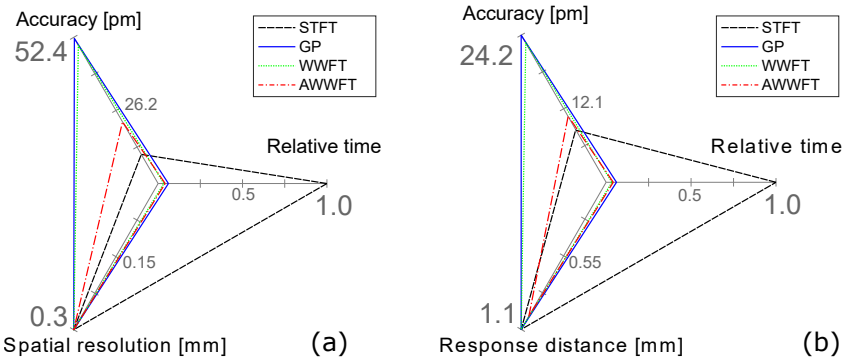

Fig. 5.17. The spider chart of the performances of different demodulation methods in (a) simulation and (b) experiment.

Chapter 6

Simultaneous Strain and Temperature Measurement

It has been proven that FBG sensors are capable of fully distributed measurement. Furthermore, FBG-OFDR sensors have sufficient accuracy at high spatial resolution of millimeter or sub millimeter order, which is important for SHM. However, for strain measurement, large temperature variations are common in practical applications. The measurement accuracy will be reduced by the cross-sensitivity of temperature and strain in the sensing head. Thus, a compensation of the influence caused by temperature variation is required. Conventionally, in addition to the strain sensor, which is sensitive to both strain and temperature, a reference FBG in stress-free condition is used as temperature sensor [94]. Since the reference FBG is in parallel located in the same environment as the strain sensor, the error of strain induced by temperature variation can be compensated by subtracting the wavelength shift of temperature sensor from the wavelength shift of the strain sensor. However, it is complicated to keep the reference FBG stress-free. Usually, it is preserved in a glass capillary. What's worse, for distributed sensing, it is very difficult to avoid the misplacement between the reference FBG and strain sensing FBG that will introduce extra sensing errors, especially when high spatial resolution is required. Hence, techniques of simultaneous strain and temperature measurement with one single FBG are under development. Echevarria *et al.* discriminated strain and temperature by measuring the first and second order diffraction wavelength of an FBG [95]. Sudo *et al.* inscribed an FBG into a polarization maintaining (PM) fiber and realized simultaneous point sensing of strain and temperature [96]. In 2011, Wada *et al.* applied a PANDA-FBG to an optical frequency domain reflectometry (OFDR), and succeeded in simultaneous distributed measurement of strain and temperature [60], which was an important progress for SHM. In this chapter, the conventional method using stressed and stress-free FBG is introduced in Section 6.1. Later, the method using PM-FBG (PANDA type) with ultra high birefringence is demonstrated and introduced in Section 6.3. In this part, the potential improvements of this method is also studied. In Section 6.4, a novel approach using multiple doped FBG with different dopants are proposed being expected to achieve higher accuracy and more stable performance than PANDA-FBG based approach. In Section 6.5, an intelligent approach namely self-evaluation is introduced. It aims to distinguish the abnormal errors from the reliable values in the dynamic distributed measurement of strain and temperature.

6.1 Reference FBG Method

Conventionally, in addition to the strain sensing FBG, a reference FBG is applied for the compensation of temperature. Usually, the reference fiber is kept stress-free with some special structures. For example, the FBG might be inserted into a capillary, as shown in Fig. 6.1. As can be seen, only one end of the fiber is fixed to the capillary for keeping

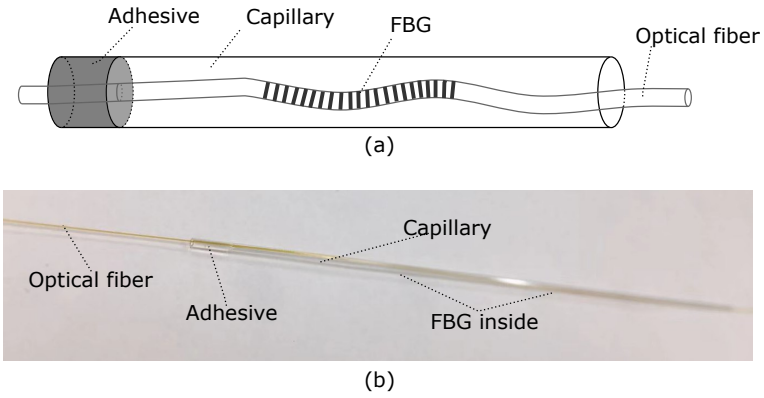

Fig. 6.1. Schematic and picture of the temperature sensing FBG setup with on end fixed: (a) schematic, (b) picture.

the inside FBG stress-free. In the application, the strain sensor and reference sensor are installed in parallel and next to each other. Since the strain sensor is sensitive to both strain and temperature while the reference one is only sensitive to the temperature, this arrange can theoretically compensate the temperature perturbation. Also, the reference fiber with both ends fixed as shown in Fig. 6.2. Similarly, the fiber in the capillary or other tubes is

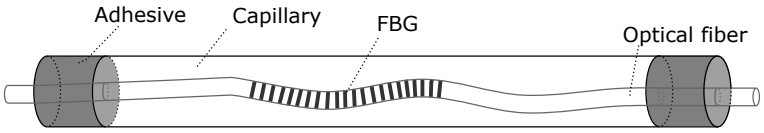

Fig. 6.2. Schematic of the temperature sensing FBG setup with two ends fixed.

loose that is insensitive to the strain. These arrangements are mature and efficient for point (single/multiple) FBG sensors, and commercial product is available. In addition, there are some integrated solutions for point strain and temperature sensing such as the one shown in Fig. 6.3. In this sensor, the FBG-1 is sensitive to the thermal strain of the metal plate and

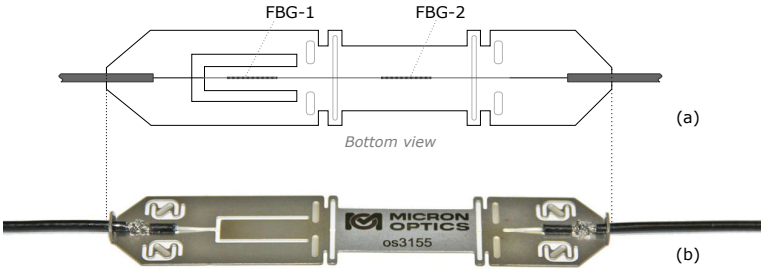

Fig. 6.3. An integrated FBG strain and temperature sensor: (a) schematic of bottom view, (b) photo http://www.micronoptics.com/product/optical-strain-gage-os3155/

the temperature while the FBG-2 is additionally sensitive to the mechanical strain of the host structure where the sensor is installed. Therefore, by subtracting the detected Bragg wavelength shift of FBG-1 from the one of FBG-2, the desired mechanical strain can be obtained.

Although, all the approaches introduced above are effective for the temperature compensation of FBG strain sensing, practically, there are still several issues:

- Since the capillary is much thicker than the optical fiber, it is very difficult to say that its temperature is the same as that of the strain sensor.
- To preserve the stress-free condition and have similar thermal conductivity to that of the optical fiber, the capillary is usually made by silica glass. Therefore, such a setup has to be arranged into short sections (usually several centimeters) to prevent the mechanical damage under strain. This will limit its applicability in distributed measurements especially fully distributed ones.
- Due to the size of capillary/metal plate and stress-free condition, it is not feasible for embedded sensing.

Therefore, the development of simultaneous strain and temperature sensing is attractive.

6.2 Principle of Simultaneous Measurement

Based on the linear assumption in Eq. (3.10), the strain and temperature sensitivities of the FBG can be respectively expressed as

$$K_\varepsilon = 2n_{\text{eff}}\Lambda\left\{1 - \frac{n_{\text{eff}}^2}{2}\left[P_{12} - \nu(P_{11} + P_{12})\right]\right\}, \tag{6.1}$$

$$K_T = 2n_{\text{eff}}\Lambda\left[\alpha + \frac{\left(\frac{dn}{dT}\right)}{n_{\text{eff}}}\right]. \tag{6.2}$$

Assume that there are two FBGs with different K_ε and K_T are being applied with the same strain and temperature variations, the corresponding Bragg wavelength shifts can be expressed as

$$\begin{bmatrix}\Delta\lambda_1\\ \Delta\lambda_2\end{bmatrix} = \begin{bmatrix}K_{\varepsilon,1} & K_{T,1}\\ K_{\varepsilon,2} & K_{T,2}\end{bmatrix}\begin{bmatrix}\Delta\varepsilon\\ \Delta T\end{bmatrix} \tag{6.3}$$

Defining the sensitivity matrix ($\mathbf{K}$ matrix) as

$$\mathbf{K} = \begin{bmatrix}K_{\varepsilon,1} & K_{T,1}\\ K_{\varepsilon,2} & K_{T,2}\end{bmatrix}, \tag{6.4}$$

the strain and temperature can be revealed by simultaneously detecting both Bragg wavelength, which is expressed as

$$\begin{bmatrix}\Delta\varepsilon\\ \Delta T\end{bmatrix} = \mathbf{K}^{-1}\begin{bmatrix}\Delta\lambda_1\\ \Delta\lambda_2\end{bmatrix}. \tag{6.5}$$

Consequently, the key to realize simultaneous measurement is to enlarge the linear independence of the $\mathbf{v}_K = (K_\varepsilon, K_T)$ vectors of the two selected FBGs. Since, currently, the electrical strain and temperature sensors, of which the accuracies are 10 με and 1 °C, respectively, satisfy most applications, the final target of simultaneous measurement is to achieve

the same accuracy level. Of course, to take advantage of the FBG-OFDR system, millimeter order spatial resolution is desired to be remained while improving the accuracy.

6.3 Hi-Bi PANDA-FBG Based Method

One potential pair of the $\mathbf{v}_K$ vectors can be found in the PM-FBGs. As mentioned in Section 3.2, the anisotropic feature at the cross section, causing birefringence, will generate differences in the optical properties of two orthogonal polarization modes (fast mode and slow mode). In details, those differences mainly happen to n_{eff} and dn/dT. Therefore, the PM-FBG can be applied for the simultaneous sensing.

In PM-FBG, the elements in $\mathbf{K}$ matrix is of the form

$$K_{\varepsilon,\text{f}} = 2(n_\text{s} - B)\Lambda \left\{1 - \frac{(n_\text{s} - B)^2}{2}\left[P_{12} - \nu(P_{11} + P_{12})\right]\right\}, \tag{6.6}$$

$$K_{T,\text{f}} = 2(n_\text{s} - B)\Lambda \left[\alpha + \frac{\left(\frac{dn}{dT}\right)_\text{f}}{n_\text{s} - B}\right], \tag{6.7}$$

$$K_{\varepsilon,\text{s}} = 2n_\text{s}\Lambda \left\{1 - \frac{n_\text{s}^2}{2}\left[P_{12} - \nu(P_{11} + P_{12})\right]\right\}, \tag{6.8}$$

$$K_{T,\text{s}} = 2n_\text{s}\Lambda \left[\alpha + \frac{\left(\frac{dn}{dT}\right)_\text{s}}{n_\text{s}}\right], \tag{6.9}$$

where n_s is the effective refractive index of the slow mode, $\left(\frac{dn}{dT}\right)_\text{s}$ and $\left(\frac{dn}{dT}\right)_\text{f}$ are the thermo-optic coefficients for the slow and fast mode respectively. Their relation can be approximately described using a simple linear assumption as

$$\left(\frac{dn}{dT}\right)_\text{f} - \left(\frac{dn}{dT}\right)_\text{s} = \frac{B}{\Delta T_\text{anl}}, \tag{6.10}$$

where ΔT_anl is the annealing temperature during the fiber drawing process.

Such an approach was firstly demonstrated by Sudo *et al.* for point sensing [96]. Later, Wada *et al.* conducted distributed simultaneous measurement for uniform strain and temperature [60]. However, the accuracy ($-100 \sim 69\,\mu\varepsilon$ and $-5.7 \sim 6.1\,^\circ\text{C}$) turned out to be not enough for practical SHM applications. For improving the accuracy, one potential method is to increase the birefringence of the PM fiber [97].

6.3.1 Simulation

The possible measurement accuracy vs. birefringence relation was firstly investigated using the numerical simulation. By increasing the birefringence from 3.0×10^{-4} to 3.2×10^{-3}, and applying the initial parameters in Table 6.1, the estimated curve are obtained from the introduced simulation in Section 4.2.3. Defining the accuracy as RMSD in the form of Eq. (5.18), and feeding the random errors given in Table 6.2, the obtained accuracy vs. birefringence relation is shown in Fig. 6.4. Note that practically, the random errors have the normal distributions of which the standard deviations equal to the given values. It is clear in the figure that with the increase in birefringence, the accuracies for both strain and temperature measurements will be improved, although the improvement is getting less

Table 6.1. Parameters of the PANDA-FBG in simulation.

Parameter	Value
n_{eff}	1.46
Λ	531 nm
υ_{fg}	0.394
κ_{ac}	$1.42\,\text{m}^{-1}$
α	$1.09 \times 10^{-6}\,^{\circ}\text{C}^{-1}$
L_{g}	300 mm
$(dn/dT)_{\text{s}}$	$8.95 \times 10^{-6}\,^{\circ}\text{C}^{-1}$
ΔT_{anl}	900 °C

Table 6.2. Input random errors of the accuracy analysis.

Parameter	Value
Bragg wavelength detection	± 3.0 pm
Reference strain	$\pm 0.2\,\mu\varepsilon$
Reference temperature	$\pm 0.1\,^{\circ}\text{C}$

efficient. In this study, the spatial resolution (Δz_{sp}) and readout resolution (Δz_{rd}) of the OFDR is set to be 1.6 mm and 0.5 mm, respectively.

6.3.2 Experiment

To verify the assumption, four FBGs with the same Bragg wavelength in slow axis are inscribed in four PANDA type PM fibers respectively. The birefringences are different for each fiber, as shown in Table 6.3.

Before applying the sensors for simultaneous measurements, they are firstly calibrated using the setup shown in Fig. 6.5. The strain is applied by a pair of stationary stage and translation stage. By monitoring the displacement using a laser displacement sensor (accuracy: 0.02 µm), which equals to the elongation of FUT, the corresponding strain value can be converted by

$$\varepsilon = \frac{\Delta z_{\text{ds}}}{L_{\text{FUT}}}, \tag{6.11}$$

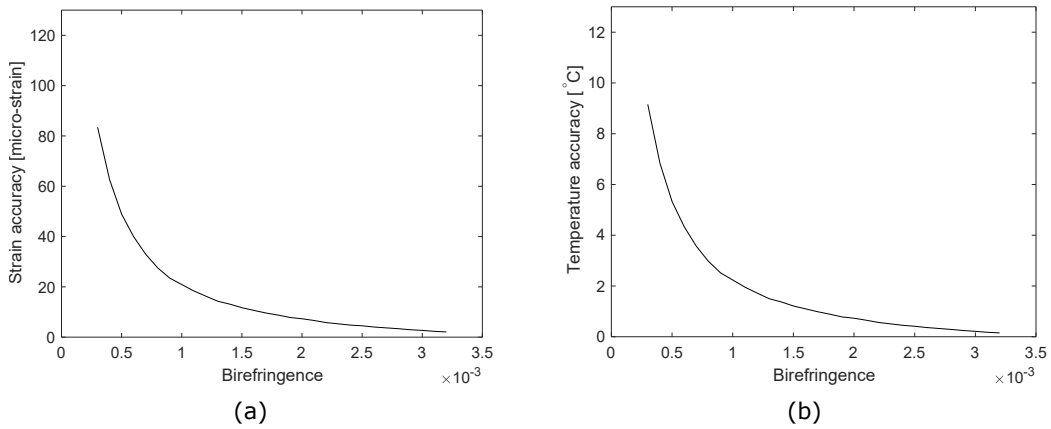

Fig. 6.4. Estimated measurement accuracies vs birefringence relations of PANDA-FBG by simulation: (a) strain accuracy, (b) temperature accuracy.

Table 6.3. PANDA-FBGs with different birefringences.

Type	Bragg wavelength [nm]		Birefringence [$\times 10^{-4}$]	FBG length [mm]
	Fast mode	Slow mode		
PANDA-A	1549.65	1550.01	3.37	300
PANDA-B	1549.57	1550.12	5.20	300
PANDA-C	1549.39	1550.02	5.98	300
PANDA-D	1549.17	1550.10	8.77	300

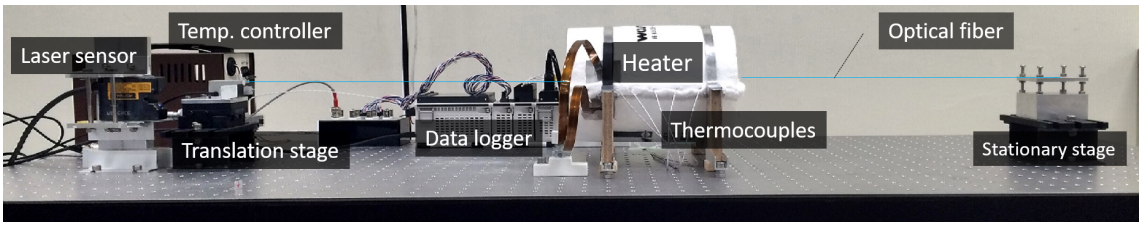

Fig. 6.5. Experimental setup for simultaneous strain and temperature measurement.

where Δz_{ds} is the displacement and L_{FUT} is the length of FUT. Meanwhile, the temperature variation is applied by the cylinder heater and monitored by thermocouples. As shown in

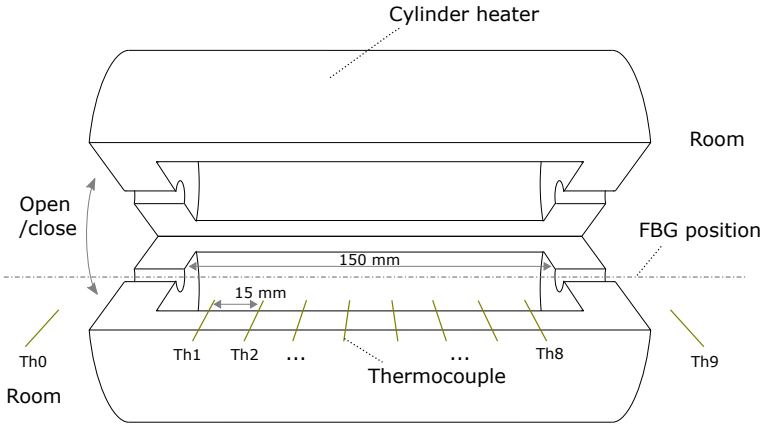

Fig. 6.6. Experimental arrangement of the cylinder heater and thermocouples.

Fig. 6.6, the temperature distribution inside the heater as well as the room temperature are monitored by thermocouples. The calibrated strain and temperature sensitivities are shown in Table 6.4. In the field of numerical analysis, the condition number of a function with respect to an argument measures how much the output value of the function can change for a small change in the input argument [98]. Thus, it can be a brief estimation of the potential measurement performance. As shown in Fig. 6.7, with the highest birefringence, the PANDA-D shows the smallest condition number that is supposed to have the best accuracy among the four types.

For verification, a simultaneous measurement of strain and temperature distribution is conducted. In the testing, a uniform strain distribution of $\sim 500\,\mu\varepsilon$ was applied to the FUT. Meanwhile, the temperature in the middle of the heater was increased from room temperature ($\sim 19\,^{\circ}\mathrm{C}$) to $\sim 85\,^{\circ}\mathrm{C}$. The discriminated strain and temperature are plotted in Fig. 6.8. As can be observed in the figure, the uniform strain and non-uniform temperature profile both can be detected. To make a quantitative conclusion of their sensing performance in terms of accuracy, the RMSD is calculated within the range of $[125, 175]\,\mathrm{mm}$ and plotted

Table 6.4. Calibrated sensitivities of different types of PANDA-FBGs.

Type	$K_{\varepsilon,\mathrm{f}}$ [pm/με]	$K_{\varepsilon,\mathrm{s}}$ [pm/με]	$K_{T,\mathrm{f}}$ [pm/°C]	$K_{T,\mathrm{s}}$ [pm/°C]
PANDA-A	1.181	1.192	11.024	10.642
PANDA-B	1.255	1.272	11.051	10.467
PANDA-C	1.207	1.226	11.169	10.541
PANDA-D	1.215	1.235	11.235	10.427

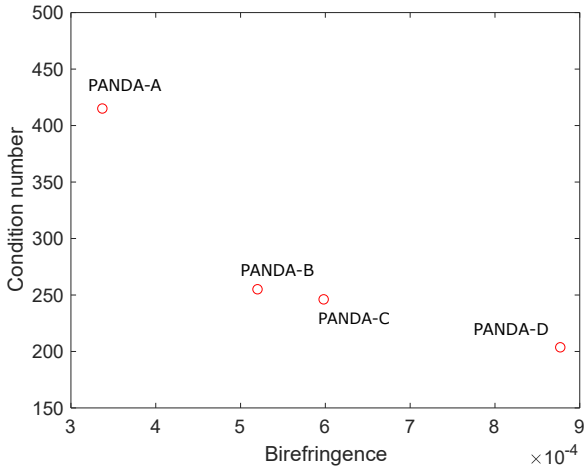

Fig. 6.7. Condition number of the **K** matrix of different PANDA-FBGs

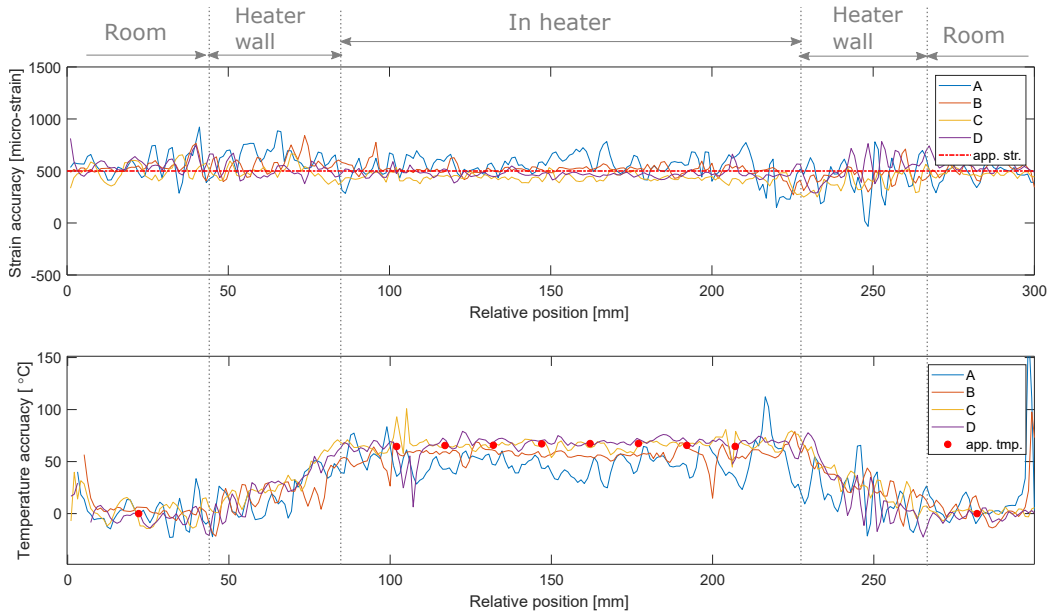

Fig. 6.8. Simultaneously measured strain and temperature distribution: (a) strain, (b) temperature.

together with the simulated results as shown in Fig. 6.9. This range was selected for avoiding the non-FBG inscribed gaps, where the measurement was not reliable, around 100 mm and 200 mm. It can be seen that the trends in the experiment and the simulation

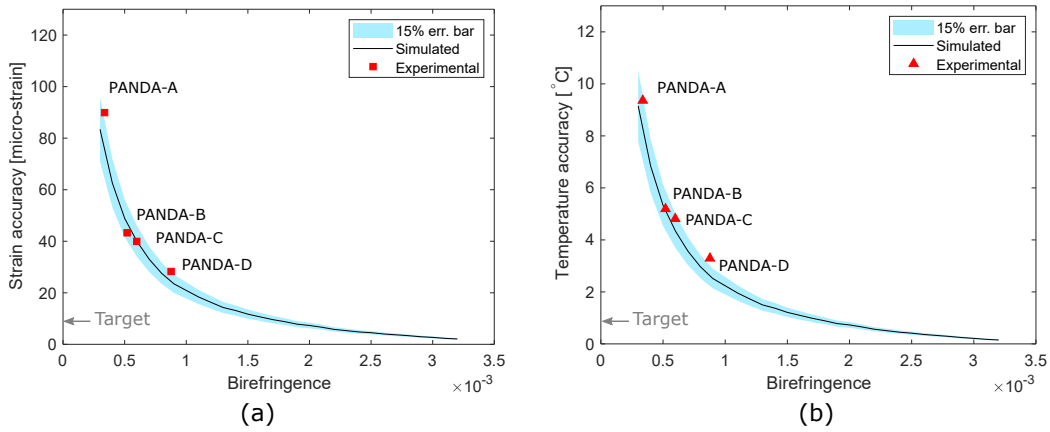

Fig. 6.9. Estimated measurement accuracies vs birefringence relations of PANDA-FBGs in experiment and simulation: (a) strain accuracy, (b) temperature accuracy.

agree with each other in both simulation. Although, the values are not the same, the experimental results generally locate within the ±15% error bar area of the simulated curves. However, the obtained best accuracy by PANDA-D (29.1 με and 2.9 °C) are still far from the targets (10 με and 1 °C). As aforementioned, the targets are supposed to satisfy most SHM applications practically. It is worthing mentioning that if the millimeter spatial resolution is over qualified for the measurement purpose in a certain application, spatial smoothing process can be applied for effectively improving the accuracies. For example, by applying moving average of which the span is 5 mm, the accuracies can be improved to be 21.3 με and 2.2 °C.

Because of the agreement of the simulation and experimental results, the proposed numerical model can be used as a reference tool to support the Hi-Bi fiber design and sensing performance estimation. Currently, the highest birefringence of PANDA fiber ever reported is achieve to be 1×10^{-3} by Hayashi *et al.* [99]. The corresponding accuracies are ~ 20.1 με and ~ 2.1 °C. Considering the practical manufacturing, further improvement is a very big challenge.

6.4 Doped FBG Based Method

In this part, an approach using FBGs inscribed in doped fibers is proposed for the simultaneous measurement of strain and temperature distribution. This approach applies the combinations of two different doped FBGs and realized the measurement based on regular determined systems. Additionally, by constructing overdetermined systems, the approach has shown significant robustness.

Abridged...

6.5 Self-Evaluation in Dynamic Distributed Simultaneous Measurement

In the applications of SHM, reliable assessment of the host structures rely on the reliable sensing results. Practically, unexpected local failures, such as decay of FBG, physical damage, may occur to the installed sensors, leading to abnormal errors. In order to distinguish them, conventionally, people install strain gauges or thermocouples at some locations as reference to estimate the level of measurement errors during the operation [38, 100, 101]. However, the use of reference sensors will make the sensing system more complicated, especially for distributed sensing, because the reference sensors are usually not distributed.

For multi-parameter DOFSs, namely strain and temperature in this study, the situation is special. Since the parameters are sensed by the same sensing component/system, their values have some hidden correlations which can be retrieved and applied as the "reference information". In this part, we use Hi-Bi PANDA-FBG based distributed simultaneous strain and temperature sensor as example. Base on the sensing properties we realized the "self-evaluation", referring to the error estimation without using other reference sensors. To our best knowledge, this is the first time that by only using the optical fiber itself the dynamic distributed error levels are available to be estimated. The employment of this technique can make further improvement of the sensing system's applicability and reliability.

6.5.1 Reliability of Strain and Temperature Sensor

The reliability of sensors should be distinguished from the structural reliability. The general definition of *reliability* in engineering is "concerned with the ability of a system or component to perform its required functions under stated conditions for a specified time". This means the reliability highly depends on where and for what the structure/sensor is applied. Let us use two applications of FBG sensors as examples.

- **FBG Damage Detection**

  FBG sensors may be used for the identification of types of damages of composite structures such as transverse crack and delamination [102, 103]. When there is a damage of the structure in the area where an FBG sensor is installed, apart from the Bragg wavelength shift, deformation of the spectral profile will occur. As shown in Fig. 6.10, the initial single Bragg peak splits into several ones with smaller reflections. Therefore, it is not feasible to measure the strain using Bragg wavelength shift. Instead, the FWHM or intensity ratio of dispersed and initial spectrum are used for evaluating the damage condition. In this case, even though the value of the strain may be unreliable, the FBG sensor is reliable for the damage identification use.

- **FBG Shape Sensing**

  The shape sensing contributes a lot of progresses in the SHM field including aircraft, bridges, roadways, buildings, ships and spacecraft. Among the technologies applied, distributed (fully or quasi) FBG sensors play important roles for their unique advantages [104–106]. In general, as shown in Fig. 6.11, these technologies follow the flowchart for sensing the shape of the fiber/structure. Since the shape (3D or 2D) is reconstructed by the detected strain distribution, for such application, the reliability mainly rely on the accuracy level of strain sensing.

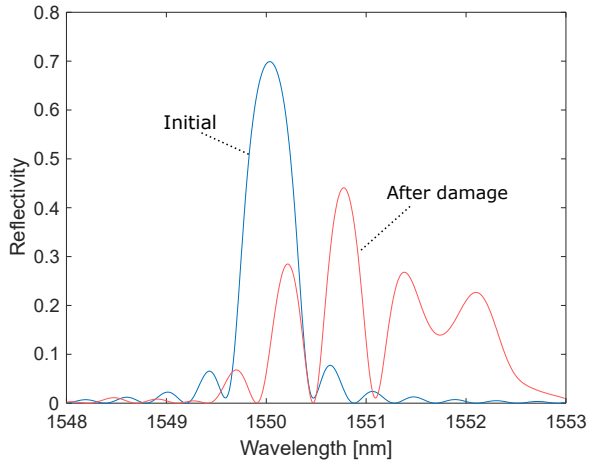

Fig. 6.10. Spectral change of FBG before and after damage.

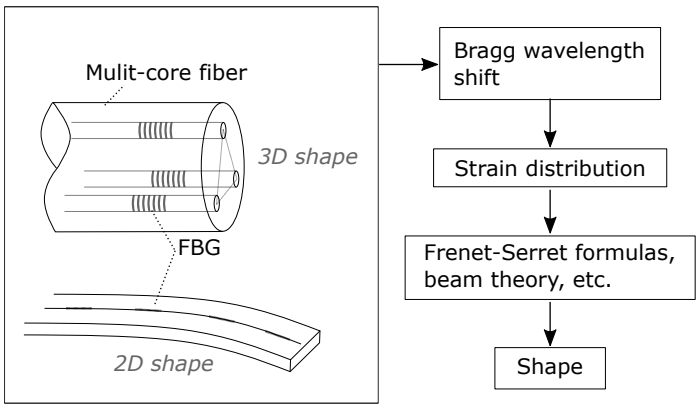

Fig. 6.11. Flowchart of FBG based shape sensing.

Therefore, when evaluating the performance of the sensors, their potential applications should be considered as well. In this study, the distributed strain and temperature sensor are developed for the assessment or measurement of structures based on the strain values and their distribution overtime. Thus, the focus of such a self-evaluation is to estimate the sensing accuracy/error using the correlations between strain and temperature sensing mechanisms.

6.5.2 Self-evaluation Principle

Conventionally, to evaluate a newly developed sensor, other well developed sensors whose performances are believed to be known and stable are applied together. Usually, the selected reference sensors are much more accurate than the sensor under testing, so that the monitored data are regarded as the applied values in the testing. Then, the accuracy of sensor under test is estimated by using the RMSD as depicted in Eq. (5.18).

Although, in previous sections, the reference sensors (laser displacement sensor and thermocouples) worked well for estimating the errors during the measurement, they will become less applicable in practical cases, especially when the FBG sensor is bonded or embedded. Thus, the development of a fast and reliable evaluation function of the system is necessary. In this section, a novel self-evaluation method for distributed PANDA-FBG

sensor is introduced.

In the simultaneous measurement, various errors may come from the Bragg wavelength detection, calibration of $\mathbf{K}$ matrix, low SNR, damage, etc. By using Eq. (6.5), their relations can be expressed as

$$\begin{bmatrix} \Delta\varepsilon + \delta\varepsilon \\ \Delta T + \delta T \end{bmatrix} = \left(\mathbf{K}^{-1} + \delta\mathbf{K}_{\text{inv}}\right) \begin{bmatrix} \Delta\lambda_{\text{f}} + \delta\lambda_{\text{f}} \\ \Delta\lambda_{\text{s}} + \delta\lambda_{\text{s}} \end{bmatrix}, \tag{6.12}$$

$$\begin{bmatrix} \delta\varepsilon \\ \delta T \end{bmatrix} = \mathbf{K}^{-1} \begin{bmatrix} \delta\lambda_{\text{f}} \\ \delta\lambda_{\text{s}} \end{bmatrix} + \delta\mathbf{K}_{\text{inv}}\mathbf{K} \begin{bmatrix} \Delta\varepsilon \\ \Delta T \end{bmatrix} + \delta\mathbf{K}_{\text{inv}} \begin{bmatrix} \delta\lambda_{\text{f}} \\ \delta\lambda_{\text{s}} \end{bmatrix}, \tag{6.13}$$

where $\delta\varepsilon$ is the error of strain, δT is the error of temperature, $\delta\mathbf{K}_{\text{inv}}$ is the error of inversed matrix $\mathbf{K}$, $\delta\lambda_{\text{f}}$ is the error of wavelength shift of fast mode and $\delta\lambda_{\text{s}}$ is the error of wavelength shift of slow mode [97]. Among the terms at the right hand side of Eq. (6.13), the first one is dominating the value of errors. Considering the relations of $K_{\varepsilon,\text{f}} \approx K_{\varepsilon,\text{s}}$ and $K_{T,\text{f}} \approx K_{T,\text{s}}$, the first term can be derived into

$$\delta_{\text{main}} = \mathbf{K}^{-1} \begin{bmatrix} \delta\lambda_f \\ \delta\lambda_{\text{s}} \end{bmatrix} \approx \frac{\delta\lambda_{\text{f}} - \delta\lambda_{\text{s}}}{K_{\varepsilon,\text{f}}K_{T,\text{s}} - K_{T,\text{f}}K_{\varepsilon,\text{s}}} \begin{bmatrix} K_{T,\text{s}} \\ -K_{\varepsilon,\text{s}} \end{bmatrix}. \tag{6.14}$$

From the derived relation, we can see that errors of strain and temperature always have approximately constant ratio of $-K_{T,\text{s}}/K_{\varepsilon,\text{s}}$, about -9. Figure 6.12 depicts an example of strain and temperature distribution with errors. The red arrows mark some obvious "sym-

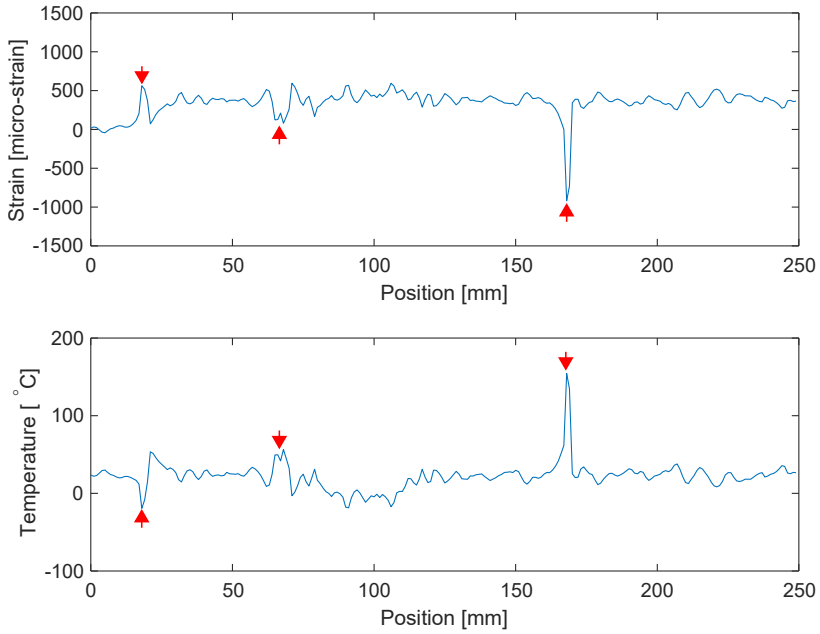

Fig. 6.12. Example strain and temperature discriminated by using PANDA-FBG.

metric" pattern in the distributions. Therefore, by identifying their position and give an estimation of the values, the evaluation can be achieved without extra sensors for reference. The details of the process is illustrated flowchart, Fig. 6.13. By sliding a window along the position for strain, ε, and temperature, T, then removing the linear trends of the windowed signals, the cross correlations and cosine similarities are calculated step by step. Then, by selecting the zero lag magnitude of local cross correlated signals, the overall error level (in

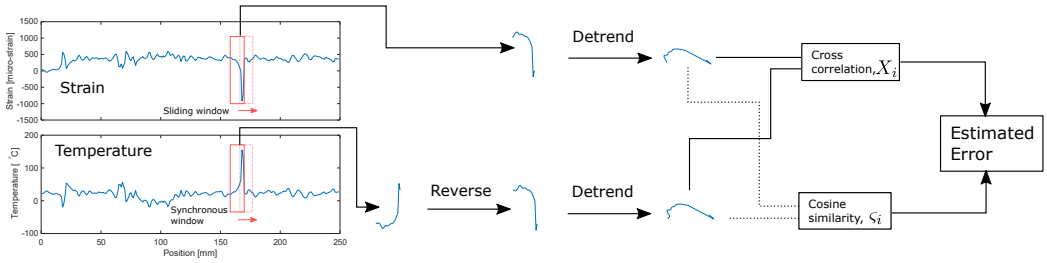

Fig. 6.13. The flowchart for 1D self-evaluation.

absolute value) is expressed as

$$\begin{aligned}\delta_{\varepsilon,i} &= \varsigma_i^{1/(1-\varsigma_i)}\mathrm{Re}\left(\sqrt{X_{c,i}K_{T,\mathrm{s}}/K_{\varepsilon,\mathrm{s}}}\right),\\ \delta_{T,i} &= \varsigma_i^{1/(1-\varsigma_i)}\mathrm{Re}\left(\sqrt{X_{c,i}K_{\varepsilon,\mathrm{s}}/K_{T,\mathrm{s}}}\right),\end{aligned} \tag{6.15}$$

where $X_{\mathrm{c},i}$ is the value of cross correlation of the $\mathrm{i_{th}}$ section at zero lag point, and ς_i is the corresponding cosine similarity of that section. Mathematically, their values are calculated as

$$X_{\mathrm{c},i} = \hat{\varepsilon}_{\mathrm{de},i} \star (-\hat{T}_{\mathrm{de},i})\big|_{lag=0}, \tag{6.16}$$

$$\varsigma_i = \frac{\mathbf{v}_{\varepsilon,i}\cdot\mathbf{v}_{T,i}}{\|\mathbf{v}_{\varepsilon,i}\|\,\|\mathbf{v}_{T\varepsilon,i}\|}, \tag{6.17}$$

where $\hat{\varepsilon}_{\mathrm{de},i}$ and $\hat{T}_{\mathrm{de},i}$ denote the windowed detrended section of strain and temperature. $\mathbf{v}_{\varepsilon,i}$ and $\mathbf{v}_{T,i}$ are the vectorized strain and temperature sections, respectively [107]. Note here that the term $w_i = \varsigma_i^{1/(1-\varsigma_i)}$ is the assigned weight for each section. Figure 6.14 shows the obtained distributions of sliding cross correlation, cosine similarities and weights. In the figure, large error at about 160 mm can be clearly identified. Also the weight values show very apparent non-uniform distribution that means part of the detected identified values might refer to the actual steep distributions of strain or temperature. By combining the obtained components, the estimated errors distribution with and without weight are shown in Fig. 6.15. By comparing the results with and without weight multiplied, it can be seen that at $\sim$ 166 mm the detected values are actual errors, while at $\sim$ 16 mm and $\sim$ 19 mm, they are combinations of error and actual steep distribution of strain. Therefore, it reasonable to conclude that the self-evaluation has potential to identify the large abnormal errors but, meanwhile, preserve the details of steep distribution.

6.5.3 Experimental Demonstration

To demonstrate the actual dynamic performance of the system, a set of equipment is used, as shown in Fig. 6.16 [108, 109]. Since we applied constant normal force at the clamping surface, when the translation stage is moving, constant strain can be applied to stress applied part (SAP) by kinetic friction of which the exact value (P) is monitored by the load sensor. Then the applied strain can be calculated as

$$\varepsilon = \frac{4P}{\pi E D_{\mathrm{fut}}^2}, \tag{6.18}$$

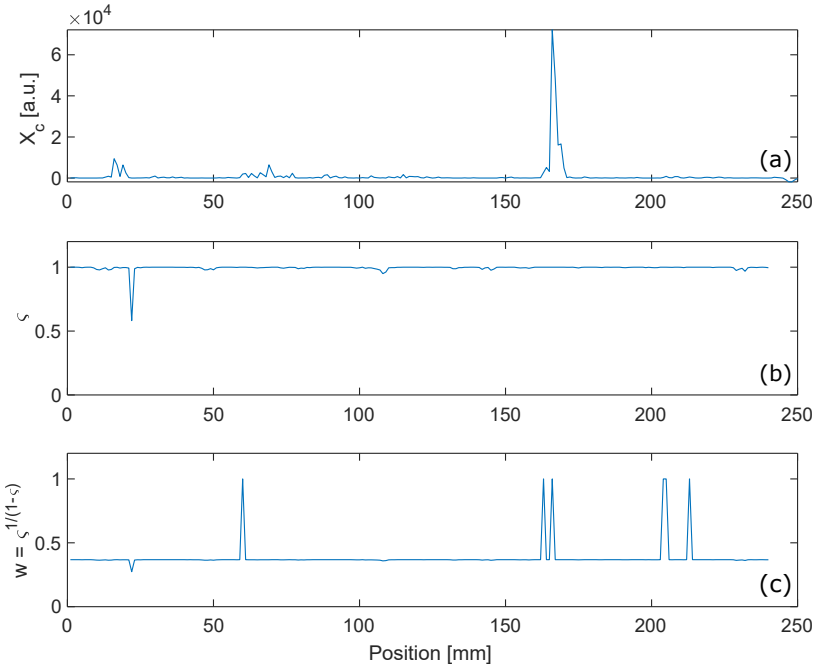

Fig. 6.14. Obtained distribution of cross correlation, cosine similarity and weight: (a) cross correlation, (b) cosine similarity and (c) weight.

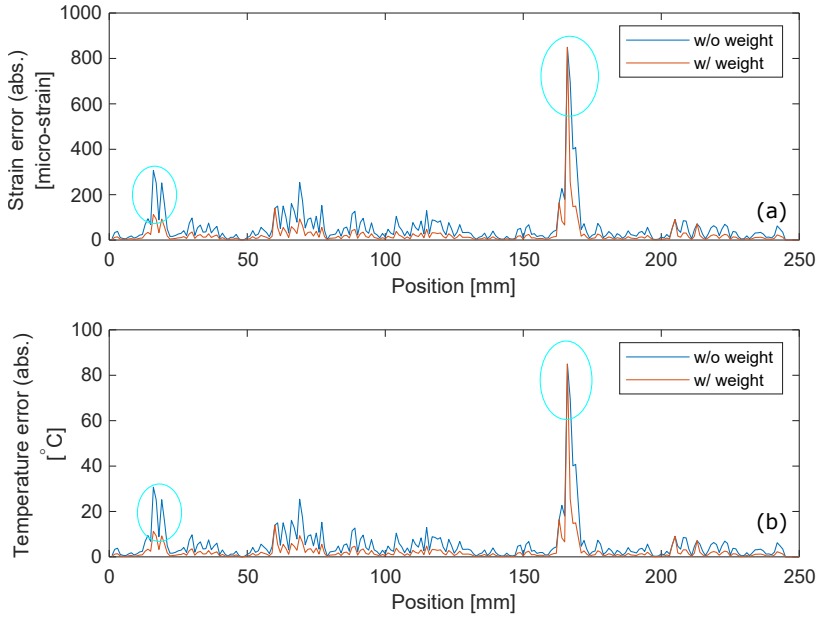

Fig. 6.15. Self-evaluated errors in absolute value: (a) strain, (b) temperature.

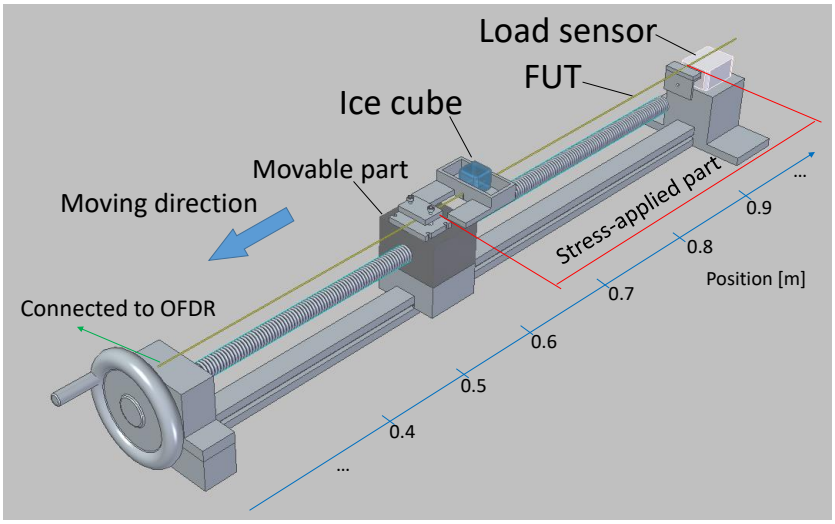

Fig. 6.16. Schematic of experimental setup for self-evaluation.

where $E = 59.2\,\mathrm{GPa}$ is the Young's modulus of fiber under test (FUT), and $D_{\mathrm{fut}} = 142\,\mu\mathrm{m}$ is the diameter of FUT, respectively. Meanwhile, the temperature distribution is applied by a pure ice cube. Since the FUT will be covered by the continuously melted water on the bottom of ice cube, 0 °C temperature can be stably applied.

In this study, the length of PANDA-FBG is 300 mm, and the Bragg wavelength of slow mode is 1550 nm. In addition, there are two $1 \sim 2\,\mathrm{mm}$ gaps at the positions of 60 mm and 160 mm, where no FBG was inscribed. They can generate similar condition as the decay of FBG which will cause abnormal errors at corresponding positions. In the demonstration, we installed the FUT to the testing equipment and moved the stage from the left hand side to the right hand side at the speed of $\sim 8.2\,\mathrm{mm/s}$. The time when the left edge of ice cube was at position 200 mm was set to be 0 s. At the same time, the Bragg wavelengths were measured by the OFDR system at 800 S/s (sampling per second). Then the distributions of strain and temperature were discriminated using Eq. (6.5). The values of the $\mathbf{K}$ matrix were calibrated to be $K_{\varepsilon,\mathrm{f}} = 1.22\,\mathrm{pm/\mu\varepsilon}$, $K_{\varepsilon,\mathrm{s}} = 1.23\,\mathrm{pm/\mu\varepsilon}$, $K_{T,\mathrm{f}} = 11.24\,\mathrm{pm/°C}$, $K_{T,\mathrm{s}} = 10.43\,\mathrm{pm/°C}$. During the test, as shown in Fig. 6.17, the room temperature was monitored to be 25 ± 0.5 °C by thermocouple, and the measured friction by load sensor was 375.0 ± 3.0 mN from 0 s to 17 s. According to Eq. (6.18), the corresponding applied strain was calculated to be $400.0 \pm 3.2\,\mu\varepsilon$.

By demodulating the beat signals from PANDA-FBG-OFDR system of each sampling, the evolutions of strain and temperature distribution can be revealed, as shown in Fig. 6.18. The movements of the clamp, ice cube, as well as two constant gaps can be clearly observed and marked. The Trace-1 is the movement of the leading edge of the moving clamp and Trace-2 is the movement of the ice cube. Meanwhile, by using the monitored data from reference sensors (load sensor and thermocouple), the reconstructed reference variations are shown in Fig. 6.19. It is clear that in this experiment, the applied strain to SAP was uniform, and its length was growing with respect to time. On the other hand, the length of ice cure covered area was constant but its position was moving at a constance speed. By regarding the values based on reference sensors as "applied" values, while FBG sensor results as measured ones. The estimated errors in absolute values by the calculation of RMSDs are plotted in Fig. 6.20. In the figures, the errors by the non FBG inscribed

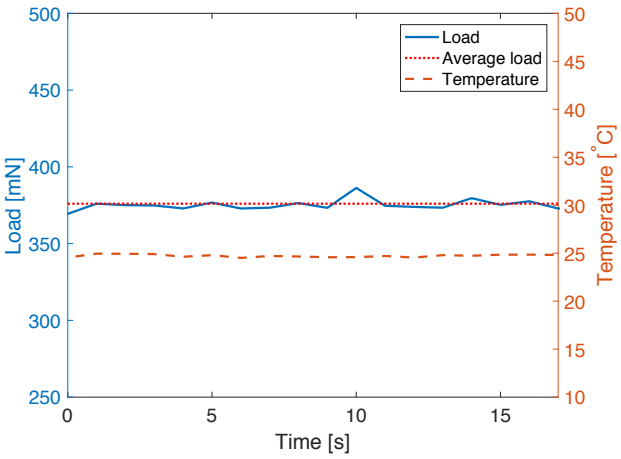

Fig. 6.17. Recorded load and temperature during the self-evaluation.

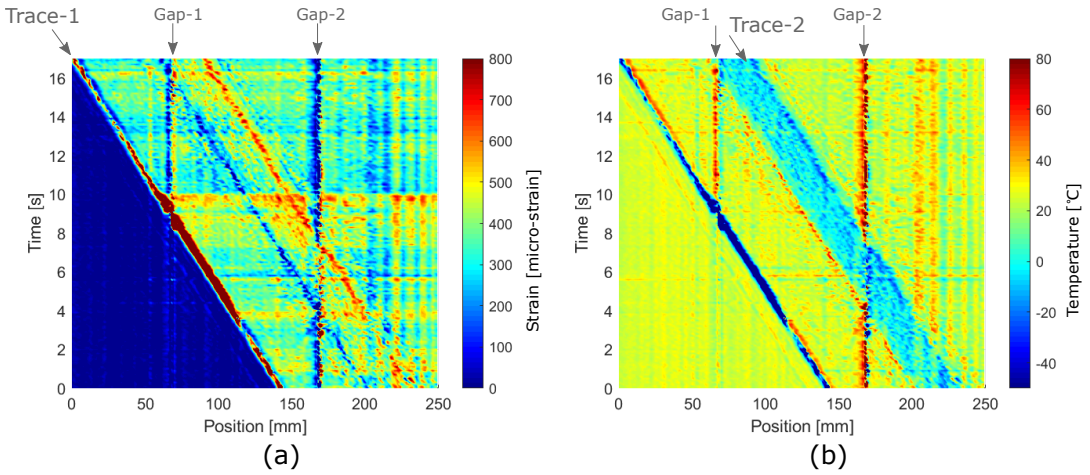

Fig. 6.18. Measured variation of strain and temperature distribution: (a) strain and (b) temperature.

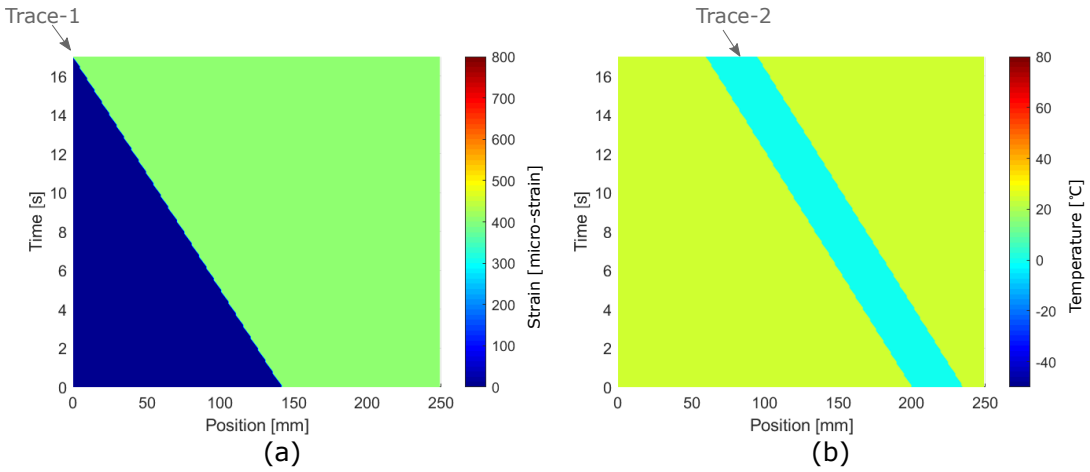

Fig. 6.19. Reconstructed variation of strain and temperature distribution using reference sensors: (a) strain and (b) temperature.

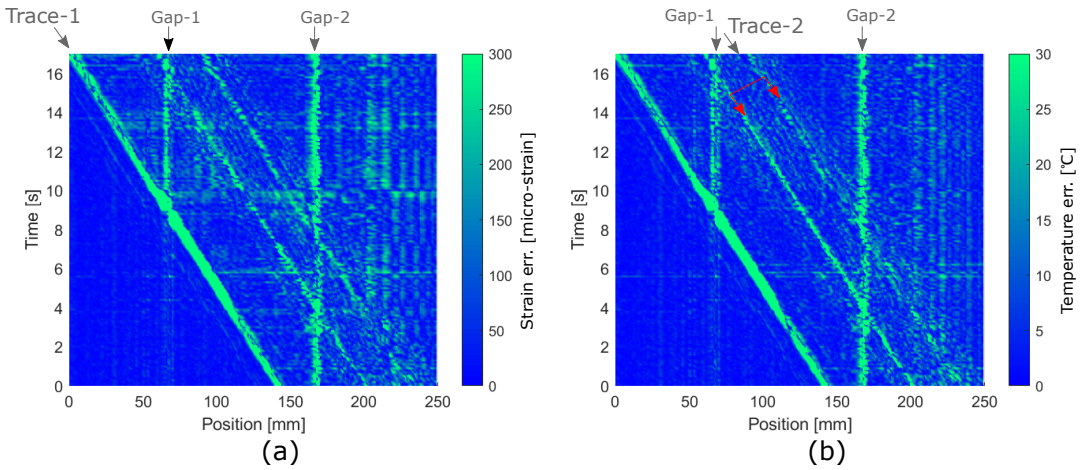

Fig. 6.20. Estimated error distribution with respect to time using reference sensors: (a) strain and (b) temperature.

gaps are obvious. Additionally, abnormal errors are observed at the Trace-1 (leading edge of the clamp) and Trace-2 (leading and trailing edges of the ice cube). These errors are caused by the optical path differences induced mismatch (offset) of the fast and slow mode of PANDA fiber. The errors caused by are very large at the position where steep (large gradient) distributions occur. Figure 6.21 illustrates a condition of steep strain induced distribution of the Bragg wavelengths in PANDA-FBG. In the figure, the dash orange line

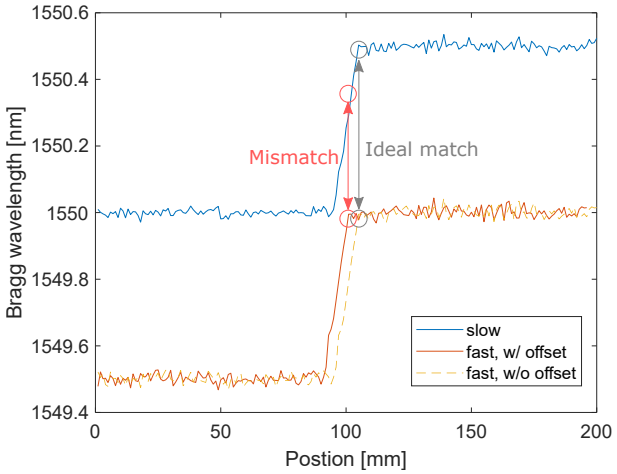

Fig. 6.21. Path difference induced mismatch.

represents the ideal position of the fast mode without offset. Therefore, ideally, the points in gray circles are supposed to be a match. However, because the offsets always exist in PM fibers, the mismatch in red ccausedircles will occur. As we can see, a small offset in position domain might lead to large errors in wavelength domain. Note that this situation is only serious at the positions where steep distribution exist. Consequently, the errors in areas like Trace-1 and 2 occurred. In the self-evaluation, the marked errors in Fig. 6.20 are also desired to be detected.

In the experiment, the self-evaluation is performed in a 2D process as, depicted in Fig. 6.22. The windowed matrices in time-spatial domain were processed in a similar as that in

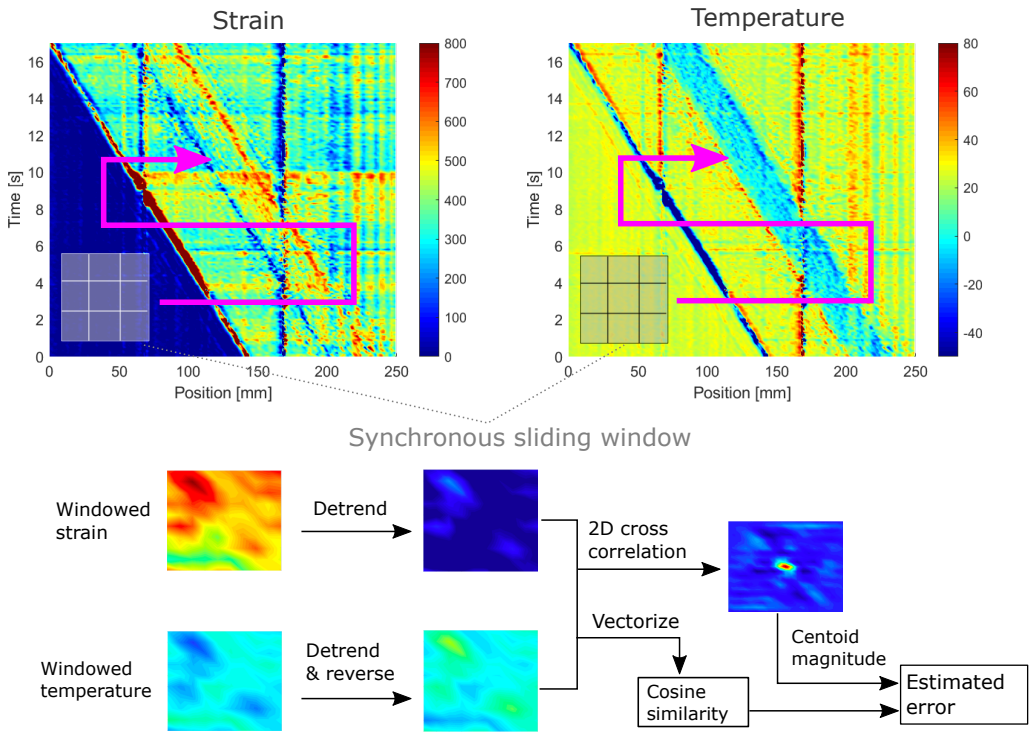

Fig. 6.22. Schematic of the self-evaluation in a 2D process.

1D cases. For an $N \times M$ matrix , the vectorization is mathematically expressed as

$$\begin{bmatrix} a_{11} & a_{12} & \cdots & a_{1M} \\ a_{21} & \ddots & & \\ \vdots & & & \vdots \\ a_{N1} & & \cdots & a_{NM} \end{bmatrix} \xrightarrow{\text{vectorize}} \begin{bmatrix} a_{11} & a_{21} & \cdots & a_{N1} & a_{N2} & \cdots & a_{NM} \end{bmatrix}. \tag{6.19}$$

This approach is available for dynamic measurements. The processed results are shown in Fig. 6.23. In this study, we use two 3×3 windows, and conduct the self-evaluation

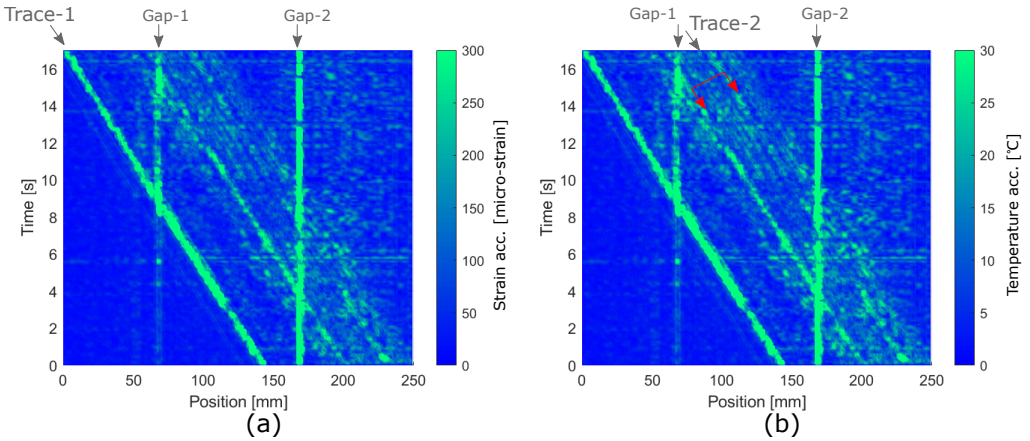

Fig. 6.23. Estimated error distribution with respect to time using reference sensors: (a) strain and (b) temperature.

for the complete measurement. In total, same as in the reference sensor based analysis, errors caused by Gap-1 and Gap-2 are observed. Meanwhile, there are identified errors at the positions of leading edge of the moving clamp and both edges of the ice cube at each moment. The nice agreement between reference sensor based and self-evaluation approach have shown that the proposed method is effective in the identifications of abnormal errors and their variations with respect to time in dynamic conditions.

6.5.4 Discussions

In order to give quantitative comparisons of self-evaluated results and conventional estimated results using reference sensors, the 2D Pearson's correlation coefficients and cosine similarities of Fig. 6.20 and 6.23 are calculated, as given in Table 6.5. Statistically, in the comparisons of both strain and temperature, strong positive linear relations [110] and high similarities are shown with the values of correlation coefficient and cosine similarity, respectively. Considering the measurement results, Gap-1 and Gap-2 gave good simulation

Table 6.5. The comparison of self-evaluation and conventional estimation.

Name	Strain	Temperature
Correlation coefficient	0.61	0.63
Cosine similarity	0.71	0.71

of local failures in the sensing FBG which will introduce confusing measured signals and disturb our strategy making. However, by taking self-evaluated error levels as reference, the large abnormal errors at $\sim 60\,\text{mm}$ and $\sim 160\,\text{mm}$ through the whole test obviously point out that there are two dead zones at corresponding positions. Additionally, the self-evaluation shows that the error levels at the front edge of clamp and both edges of ice cube are very high. Thus those measured values should not be directly used for detecting stress concentration, damage, etc. In general, this technique provides us with very direct reference for the post data analysis and strategy making in the dynamic strain and temperature distribution measurement.

The detected errors can be used as references in various ways. For example, if the noise tolerance for the strain and temperature measurements are set to be $100\,\mu\varepsilon$ and $10\,^{\circ}\text{C}$, any abnormal points in Fig. 6.18 whose errors in absolute value beyond the tolerances should be eliminated. By eliminating the identified points marked in Fig. 6.24, the retrieved strain and temperature variations were reconstructed by employing cubic interpolation, as shown in Fig. 6.25. According to the results, the errors at all the marked areas were effective decreased. For comparison, two other commonly used image filters (averaging filter and median filter [111, 112]) were applied to Fig. 6.18. The first one, in Fig. 6.26, is after the 3×3 averaging filter was applied. Compared to the reconstructed ones, the large errors, especially at Trace-1 and Trace-2 were not effectively dealt with. Meanwhile, apparent degradation of the resolution can be observed. On the other hand, in Fig. 6.27, the time-spatial informations after the median filter is similar to that after averaging filter. The size of the filter is also 3×3. Still the abnormal errors at Trace-1 and Trace-2 were not effectively decreased, but the denoising effects for Gap-1 and Gap-2 are better than that after the averaging filter. Similarly, the resolution was decreased. Consequently, it can be noted that for the effective denoising of large abnormal errors and remaining a high time-spatial resolution, the reconstruction based on self-evaluation is more efficient than the common averaging and median filter.

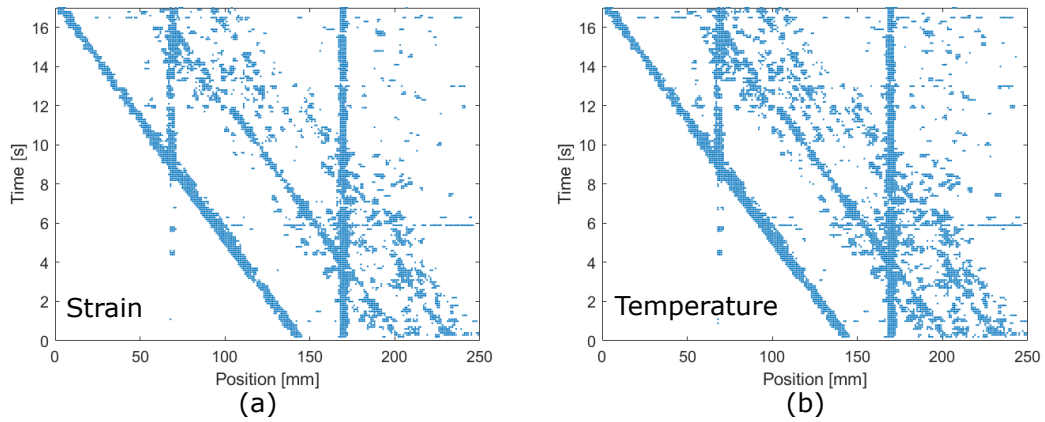

Fig. 6.24. Identified positions and times of the abnormal errors: (a) strain and (b) temperature.

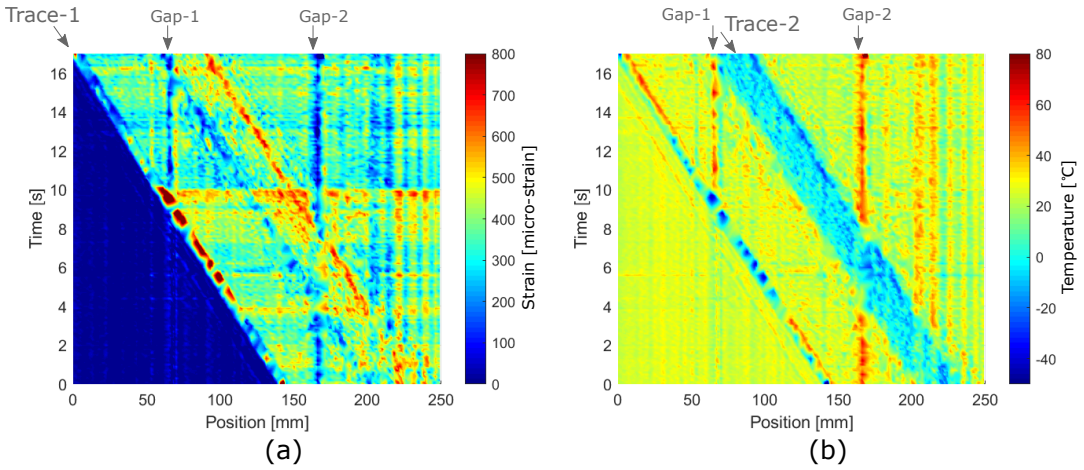

Fig. 6.25. Reconstructed strain and temperature variations after the elimination of abnormal errors: (a) strain and (b) temperature.

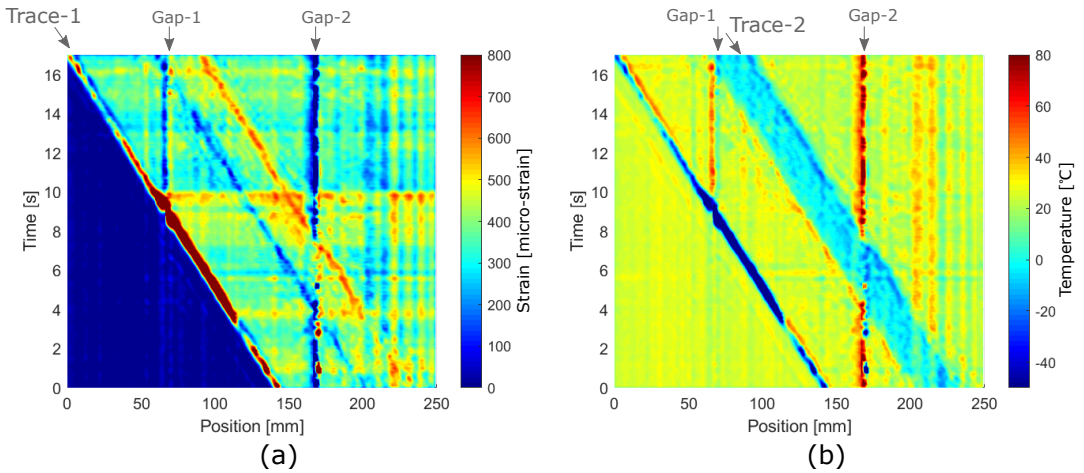

Fig. 6.26. Processed strain and temperature variations using averaging filter: (a) strain and (b) temperature.

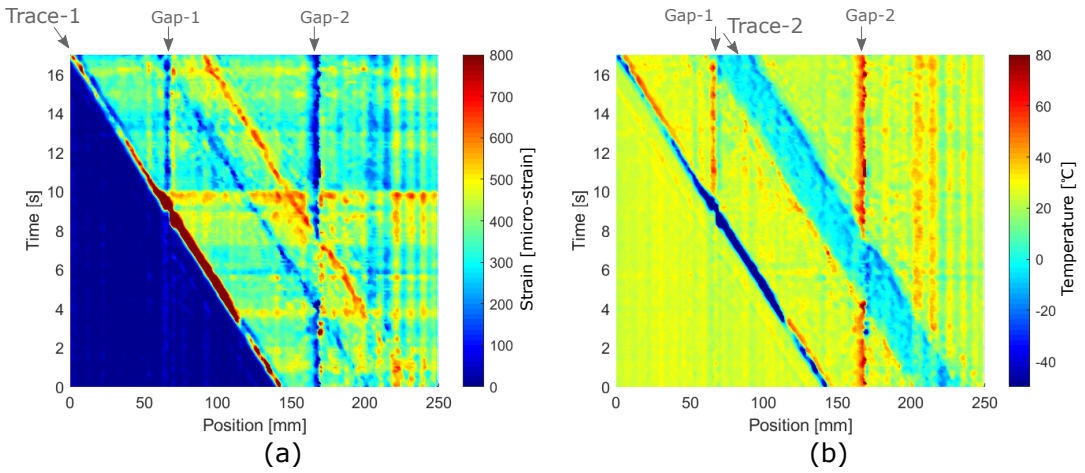

Fig. 6.27. Processed strain and temperature variations using median filter: (a) strain and (b) temperature.

It is worth mentioning that by using 3×3 windows, slightly lower spatial resolution but no obvious delay in time are observed in the self-evaluation results. However, if larger windows are applied, the spatial resolution will become even lower. Meanwhile, the significantly increased calculation will delay the self-evaluation and sampling rate that might make the self-evaluation not suitable for real time application. However, although the 3×3 window in self-evaluation decreased the resolution of the estimated errors, the resolutions for the reconstructed strain and temperature still remained at their initial level. Furthermore, the principle of self-evaluation is not limited to the PANDA-FGB sensor, but also shows good potential in other simultaneous measurement techniques, such as Brillouin scattering, Rayleigh scattering, etc [57, 59]. So, the expansion of the application of self-evaluation is one of the future works.

Chapter 7

Distributed Vibration Sensor

Fiber-optic techniques on quasi-distributed and distributed vibration sensor (DVS) are attracting a lot of attention for their excellent potential in structural health monitoring, oil and gas pipeline security, etc. [27, 113]. Currently, the most popular approach for realizing DVS is based on the phase-sensitive optical time domain reflectometry (Φ-OTDR) in which local phase variations are detected by using a laser source whose coherence length is longer than the spatial length of the interrogation pulse [22, 27, 114, 115]. However, Φ-OTDRs may suffer from the poor SNR from backscattering, which influences the performance [50, 116]. On the one hand, various approaches have been demonstrated to improve the SNR and sensitivity such as increasing the input pulse power, implementing advanced denoising algorithms, and using polarization maintaining configuration [22, 114, 117]. These systems can offer a high performance, at the cost of complicated setups and the use of high-end/expensive equipment. On the other hand, novel DVS technologies based on optical frequency domain reflectometry (OFDR) are under development [50, 118]. The increase of input pulse energy in OTDR based DVSs usually results in a worse spatial resolution. Therefore, the advantage of OFDR in high spatial resolution, which is only determined by the sweep range of tunable laser source (TLS), becomes very attractive. A. Am *et al.* demonstrated in 2014 a quasi-DVS using an array of discrete FBG arrays and double OFDR interrogation [116]. A year later, S. Wang *et al.* reported a time gated digital OFDR based DVS for demodulating the vibration induced phase changes in Rayleigh backscattering [119]. As in most approaches for vibration sensing, in such systems, a very high repetition rate (f_{sr}) is required for achieving measurable vibration frequency up to $f_{\mathrm{sr}}/2$. For an alternative, Z. Ding *et al.* presented a long distance OFDR-based method for vibration detection by the correlation analysis of non-vibrated and vibrated Rayleigh backscattering signals [118]. In this method, the maximum detectable frequency is determined by the sweeping range of the TLS and the sample number of the correlation analysis. This makes low sweeping repetition rate OFDR capable of high frequency sensing. However, this method has very low SNR and has only realized vibration detection at two locations. In this chapter, a new sensing approach for distributed vibration sensing based on slow repetition rate OFDR is introduced.

Abridged...

Conclusions and Future Works

Conclusions

This study aims to develop a distributed fiber-optic sensing system which is available for strain, temperature and vibration measurement. As a result, a numerical mode has been developed for the system design and performance analysis. Its effect and feasibility have also been proven through the experimental validation in this work.

To achieve the strain and temperature measurements, two approaches are proposed. The first one employs Hi-Bi PANDA-FBGs and achieved the accuracies as 29.1 με and 2.9 °C at 1.6 mm spatial resolution. For better accuracies and more flexible designing potential, the approach using multiple doped FBGs were studied and validated. In terms of accuracy, by constructing a regular determined system, this approach achieved 12.7 με and 1.6 °C at 1.6 mm spatial resolution, which were over 50% improved. For the first time, by constructing overdetermined systems, further improvements might be achieved (best obtained 11.8 με and 1.4 °C at 1.6 mm spatial resolution). Meanwhile, it is specially robust under unbalanced conditions, which means the quality or SNR of the different doped FBGs vary a lot. In addition, one attracting advantage of this approach is that the dopant types and concentration are available to be specially designed depending on the applications. Also, it is ideally compatible with the advanced multi-core fiber techniques for broader applicabilities.

Additionally, apart from current demodulation techniques, considering both the accuracy and measurement speed, a fast demodulation approach is proposed. It implements the features of Fourier transform, centroid detection and an integrated thresholding. Among the introduced demodulation methods, its performance has been proven to be the most balanced.

Moreover, an experiment of simultaneous measurement of dynamic strain and temperature distribution was conducted. In the demonstration, by using the error propagation properties, an adaptive algorithm was developed for the self-evaluation of measurement error levels. Since no reference sensors are needed in the approach, it is very valuable for the development of smart sensing or smart structure technologies. Also, the estimated errors can be further applied for noise reduction. The results have shown that compared to commonly used digital filters, the noise reduction is especially effective for ultra large errors.

Last but not least, the distributed vibration sensing has been successfully achieved by using the same OFDR platform as that applied for strain and temperature measurement. The maximum detectable frequency, 15 kHz, has shown excellent dynamic capability of the system. Compared to reported DVS/DASs, this system does not require high speed TLS that is more cost effective. Meanwhile, since a common interrogation system were used, the proposed methods have potential to be integrated to build a compact and efficient multi-parameter system for the distribution of strain, temperature and vibration, as well as their evolutions over time.

Future Works

As aforementioned, the developed DOFS employing a common platform is the key technology. Their integration will be one of the future works. In the integration, several scenarios might be chosen. The proposed sensing components can be in-line arranged or multiplexed through different channels of the same system. Furthermore, the exploration and exploitation of the examined technologies based on novel multi-core fibers are attractive for more flexible design and broader applications.

Appendix A

Publication List

* corresponding author, † speaker

Journal

1. **Mengshi Zhu***, Hideaki Murayama, Daichi Wada, and Kazuro Kageyama. "Dependence of measurement accuracy on the birefringence of PANDA fiber Bragg gratings in distributed simultaneous strain and temperature sensing." *Optics Express* 25, no. 4 (2017): 4000-4017.

2. **Mengshi Zhu***, Hideaki Murayama, and Daichi Wada. "Self-Evaluation of PANDA-FBG Based Sensing System for Dynamic Distributed Strain and Temperature Measurement." *Sensors* 17, no. 10 (2017): 2319.

3. **Mengshi Zhu*** and Hideaki Murayama. "Fast demodulation of OFDR based long length FBG sensing system for noisy signals." *Optics Express* 26.16 (2018): 19804-19814

Conference (International)

1. **Mengshi Zhu***, †, and Hideaki Murayama. "Simultaneous measurement of dynamic strain and temperature distribution using high birefringence PANDA fiber Bragg grating." In *25th International Conference on Optical Fiber Sensors*, pp. 103237Q-103237Q. International Society for Optics and Photonics, 2017.

2. Hideaki Murayama*, **Mengshi Zhu**†, and Daichi Wada. "Reconstruction of Comprehensive Information Using Fully-distributed FBG Sensors in Structural Health Monitoring." In *9th Australasian Congress on Applied Mechanics (ACAM9)*, 27 – 29 November 2017. (**Invited talk**)

3. **Mengshi Zhu***, †, and Hideaki Murayama. "Analytical study of the operational spatial resolution of long length FBG based OFDR." in *The 7th Asia-Pacific Optical Sensors Conference*, 2018.

Conference (Domestic)

1. **Mengshi Zhu**[*, †], Hideaki Murayama, Daichi Wada, and Kazuro Kageyama. "Dependence of measurement accuracy on the birefringence of PANDA fiber Bragg gratings in distributed simultaneous strain and temperature sensing." 第*59*回 光波センシング技術研究会講演会. (Jun. 2017)

2. Victor Shishkin[*, †], **Mengshi Zhu**, and Hideaki Murayama. "Stability comparison of point-by-point femtosecond-laser-inscribed FBGs and UV-inscribed FBGs at high temperature." 第*59*回 光波センシング技術研究会講演会. (Jun. 2017)

3. 袁　超林[†]，村山 英晶[*], 朱　夢実，荻野　豪治，影山　和郎，和田　大地. 光ファイハ゛センサによるアルミニウム平板のひす゛みと温度分布計測. *2017* 年度日本機械学会年次大会. (Sep. 2017)

References

[1] D. Balageas, C.-P. Fritzen, and A. Güemes, *Structural health monitoring*. John Wiley & Sons, 2010, vol. 90.

[2] W. Staszewski, C. Boller, and G. R. Tomlinson, *Health monitoring of aerospace structures: smart sensor technologies and signal processing*. John Wiley & Sons, 2004.

[3] V. M. Karbhari and F. Ansari, *Structural health monitoring of civil infrastructure systems*. Elsevier, 2009.

[4] S. C. Mukhopadhyay, *New developments in sensing technology for structural health monitoring*. Springer, 2011, vol. 96.

[5] R. M. Measures, *Structural monitoring with fiber optic technology*. Academic, 2001.

[6] B.-l. Shang, B.-f. Song, and F. Chang, "New sensor technologies in aircraft structural health monitoring," in *Condition Monitoring and Diagnosis, 2008. CMD 2008. International Conference on*. IEEE, 2008, pp. 701–704.

[7] H. Murayama, M. Zhu, D. Wada *et al.*, "Reconstruction of comprehensive information using fully-distributed fbg sensors in structural health monitoring," in *9th Australasian Congress on Applied Mechanics (ACAM9)*. Engineers Australia, 2017, p. 516.

[8] A. Derkevorkian, S. F. Masri, J. Alvarenga, H. Boussalis, J. Bakalyar, and W. L. Richards, "Strain-based deformation shape-estimation algorithm for control and monitoring applications," *AIAA journal*, vol. 51, no. 9, pp. 2231–2240, 2013.

[9] E. Dascotte, J. Strobbe, and U. T. Tygesen, "Continuous stress monitoring of large structures," in *Proceeding of 5th International Operational Modal Analysis Conference, Portugal*, 2013.

[10] N. E. Dowling, *Mechanical behavior of materials: engineering methods for deformation, fracture, and fatigue*. Pearson, 2012.

[11] B. Glisic and D. Inaudi, *Fibre optic methods for structural health monitoring*. John Wiley & Sons, 2008.

[12] G. Rajan and B. G. Prusty, *Structural Health Monitoring of Composite Structures Using Fiber Optic Methods*. CRC Press, 2016.

[13] G. P. Agrawal, *Nonlinear fiber optics*. Springer, 2000.

[14] I. P. Kaminow, "Polarization in optical fibers," *IEEE Journal of Quantum Electronics*, vol. 17, pp. 15–22, 1981.

[15] S. C. Rashleigh, "Origins and control of polarization effects in single-mode fibers," *Lightwave Technology, Journal of*, vol. 1, no. 2, pp. 312–331, 1983.

[16] B. H. Lee, Y. H. Kim, K. S. Park, J. B. Eom, M. J. Kim, B. S. Rho, and H. Y. Choi, "Interferometric fiber optic sensors," *Sensors*, vol. 12, no. 3, pp. 2467–2486, 2012.

[17] A. D. Kersey, M. A. Davis, H. J. Patrick, M. LeBlanc, K. Koo, C. Askins, M. Putnam, and E. J. Friebele, "Fiber grating sensors," *Journal of lightwave technology*, vol. 15, no. 8, pp. 1442–1463, 1997.

[18] R. Kashyap, *Fiber bragg gratings*. Academic press, 2009.

[19] T. Erdogan, "Fiber grating spectra," *Journal of lightwave technology*, vol. 15, no. 8, pp. 1277–1294, 1997.

[20] Y.-J. Rao, "In-fibre bragg grating sensors," *Measurement science and technology*, vol. 8, no. 4, p. 355, 1997.

[21] K. Yüksel, M. Wuilpart, V. Moeyaert, and P. Mégret, "Optical frequency domain reflectometry: A review," in *2009 11th International Conference on Transparent Optical Networks*. IEEE, 2009.

[22] Y. Lu, T. Zhu, L. Chen, and X. Bao, "Distributed vibration sensor based on coherent detection of phase-otdr," *Journal of lightwave Technology*, vol. 28, no. 22, pp. 3243–3249, 2010.

[23] X. Bao and L. Chen, "Recent progress in distributed fiber optic sensors," *Sensors*, vol. 12, no. 7, pp. 8601–8639, 2012.

[24] X. Bao, D.-P. Zhou, C. Baker, and L. Chen, "Recent development in the distributed fiber optic acoustic and ultrasonic detection," *Journal of Lightwave Technology*, vol. 35, no. 16, pp. 3256–3267, 2017.

[25] M. Froggatt and J. Moore, "High-spatial-resolution distributed strain measurement in optical fiber with rayleigh scatter," *Applied Optics*, vol. 37, no. 10, pp. 1735–1740, 1998.

[26] M. Froggatt, B. Soller, D. Gifford, and M. Wolfe, "Correlation and keying of rayleigh scatter for loss and temperature sensing in parallel optical networks," in *Optical fiber communication conference*. Optical Society of America, 2004, p. PD17.

[27] A. H. Hartog, *An introduction to distributed optical fibre sensors*. CRC Press, 2017.

[28] T. Horiguchi, T. Kurashima, and M. Tateda, "Tensile strain dependence of brillouin frequency shift in silica optical fibers," *IEEE Photonics Technology Letters*, vol. 1, no. 5, pp. 107–108, 1989.

[29] D. Culverhouse, F. Farahi, C. Pannell, and D. Jackson, "Potential of stimulated brillouin scattering as sensing mechanism for distributed temperature sensors," *Electronics Letters*, vol. 25, no. 14, pp. 913–915, 1989.

[30] K.-Y. Song, Z. He, and K. Hotate, "Distributed strain measurement with millimeter-order spatial resolution based on brillouin optical correlation domain analysis and beat lock-in detection scheme," in *Optical Fiber Sensors*. Optical Society of America, 2006, p. ThC2.

[31] A. Hartog, A. Leach, and M. Gold, "Distributed temperature sensing in solid-core fibres," *Electronics letters*, vol. 21, no. 23, pp. 1061–1062, 1985.

[32] J. Dakin, D. Pratt, G. Bibby, and J. Ross, "Distributed optical fibre raman temperature sensor using a semiconductor light source and detector," *Electronics letters*, vol. 21, no. 13, pp. 569–570, 1985.

[33] M. Davis and A. Kersey, "All-fibre bragg grating strain-sensor demodulation technique using a wavelength division coupler," *Electronics Letters*, vol. 30, no. 1, pp. 75–77, 1994.

[34] L. C. G. Valente, A. Braga, A. Ribeiro, R. D. Regazzi, W. Ecke, C. Chojetzki, and R. Willsch, "Combined time and wavelength multiplexing technique of optical fiber grating sensor arrays using commercial otdr equipment," *IEEE Sensors Journal*, vol. 3, no. 1, pp. 31–35, 2003.

[35] M. Rothhardt, M. Becker, C. Chojetzki, E. Lindner, and H. Bartelt, "Fabrication and applications of draw tower gratings," in *Bragg Gratings, Photosensitivity, and Poling in Glass Waveguides*. Optical Society of America, 2016, pp. BTh1B–1.

[36] H. Igawa, K. Ohta, T. Kasai, I. Yamaguchi, H. Murayama, and K. Kageyama, "Distributed measurements with a long gauge fbg sensor using optical frequency domain reflectometry," *Journal of Solid Mechanics and Materials Engineering*, vol. 2, no. 9, pp. 1242–1252, 2008.

[37] H. Murayama, D. Wada, and H. Igawa, "Structural health monitoring by using fiber-optic distributed strain sensors with high spatial resolution," *Photonic Sensors*, vol. 3, no. 4, pp. 355–376, 2013.

[38] B. A. Childers, M. E. Froggatt, S. G. Allison, T. C. Moore, D. A. Hare, C. F. Batten, and D. C. Jegley, "Use of 3000 bragg grating strain sensors distributed on four 8-m optical fibers during static load tests of a composite structure," in *Smart Structures and Materials 2001: Industrial and Commercial Applications of Smart Structures Technologies*, vol. 4332. International Society for Optics and Photonics, 2001, pp. 133–143.

[39] G. Xin, L. Zhengying, W. Fan, W. Yiming, W. Changjia, Z. Siyue, and Y. Haihu, "Distributed sensing technology of high-spatial resolution based on dense ultra-short fbg array with large multiplexing capacity," *Optics Express*, vol. 25, no. 23, pp. 28 112–28 122, 2017.

[40] Y. Dong, H. Zhang, L. Chen, and X. Bao, "2 cm spatial-resolution and 2 km range brillouin optical fiber sensor using a transient differential pulse pair," *Applied optics*, vol. 51, no. 9, pp. 1229–1235, 2012.

[41] Y. Dong, L. Chen, and X. Bao, "Extending the sensing range of brillouin optical time-domain analysis combining frequency-division multiplexing and in-line edfas," *Journal of Lightwave Technology*, vol. 30, no. 8, pp. 1161–1167, 2012.

[42] Y. H. Kim, K. Lee, and K. Y. Song, "Brillouin optical correlation domain analysis with more than 1 million effective sensing points based on differential measurement," *Optics express*, vol. 23, no. 26, pp. 33 241–33 248, 2015.

[43] A. Denisov, M. A. Soto, and L. Thévenaz, "Going beyond 1000000 resolved points in a brillouin distributed fiber sensor: theoretical analysis and experimental demonstration," *Light: Science & Applications*, vol. 5, no. 5, p. e16074, 2016.

[44] Y. Kumagai, S. Matsuura, S. Adachi, and K. Hotate, "Enhancement of bocda system for aircraft health monitoring," in *SICE Annual Conference, 2008.* IEEE, 2008, pp. 2184–2187.

[45] M. Höbel, J. Ricka, M. Wüthrich, and T. Binkert, "High-resolution distributed temperature sensing with the multiphoton-timing technique," *Applied optics*, vol. 34, no. 16, pp. 2955–2967, 1995.

[46] J. Park, G. Bolognini, D. Lee, P. Kim, P. Cho, F. Di Pasquale, and N. Park, "Raman-based distributed temperature sensor with simplex coding and link optimization," *IEEE Photonics Technology Letters*, vol. 18, no. 17, pp. 1879–1881, 2006.

[47] Z. Qin, L. Chen, and X. Bao, "Wavelet denoising method for improving detection performance of distributed vibration sensor," *IEEE Photonics Technology Letters*, vol. 24, no. 5, p. 542, 2012.

[48] B. J. Soller, D. K. Gifford, M. S. Wolfe, and M. E. Froggatt, "High resolution optical frequency domain reflectometry for characterization of components and assemblies," *Optics Express*, vol. 13, no. 2, pp. 666–674, 2005.

[49] F. Ito, X. Fan, and Y. Koshikiya, "Long-range coherent ofdr with light source phase noise compensation," *Journal of Lightwave Technology*, vol. 30, no. 8, pp. 1015–1024, 2012.

[50] D. Arbel and A. Eyal, "Dynamic optical frequency domain reflectometry," *Optics express*, vol. 22, no. 8, pp. 8823–8830, 2014.

[51] D. Wada, H. Igawa, M. Tamayama, T. Kasai, H. Arizono, H. Murayama, and K. Shiotsubo, "Flight demonstration of aircraft fuselage and bulkhead monitoring using optical fiber distributed sensing system," *Smart Materials and Structures*, vol. 27, no. 2, p. 025014, 2018.

[52] D. Wada, H. Igawa, and T. Kasai, "Vibration monitoring of a helicopter blade model using the optical fiber distributed strain sensing technique," *Applied optics*, vol. 55, no. 25, pp. 6953–6959, 2016.

[53] N. J. Alberto, C. A. Marques, J. L. Pinto, and R. N. Nogueira, "Three-parameter optical fiber sensor based on a tilted fiber bragg grating," *Applied Optics*, vol. 49, no. 31, pp. 6085–6091, 2010.

[54] S. M. Topliss, S. W. James, F. Davis, S. P. Higson, and R. P. Tatam, "Optical fibre long period grating based selective vapour sensing of volatile organic compounds," *Sensors and Actuators B: Chemical*, vol. 143, no. 2, pp. 629–634, 2010.

[55] O. S. Wolfbeis, "Fiber-optic chemical sensors and biosensors," *Analytical chemistry*, vol. 80, no. 12, pp. 4269–4283, 2008.

[56] R. K. Yamashita, W. Zou, Z. He, and K. Hotate, "Measurement range elongation based on temporal gating in brillouin optical correlation domain distributed simultaneous sensing of strain and temperature," *IEEE Photonics Technology Letters*, vol. 24, no. 12, pp. 1006–1008, 2012.

[57] W. Zou, Z. He, and K. Hotate, "Complete discrimination of strain and temperature using brillouin frequency shift and birefringence in a polarization-maintaining fiber," *Optics express*, vol. 17, no. 3, pp. 1248–1255, 2009.

[58] ——, "Range elongation of distributed discrimination of strain and temperature in brillouin optical correlation-domain analysis based on dual frequency modulations," *IEEE Sensors Journal*, vol. 14, no. 1, pp. 244–248, 2014.

[59] D.-P. Zhou, W. Li, L. Chen, and X. Bao, "Distributed temperature and strain discrimination with stimulated brillouin scattering and rayleigh backscatter in an optical fiber," *Sensors*, vol. 13, no. 2, pp. 1836–1845, 2013.

[60] D. Wada, H. Murayama, H. Igawa, K. Kageyama, K. Uzawa, and K. Omichi, "Simultaneous distributed measurement of strain and temperature by polarization maintaining fiber bragg grating based on optical frequency domain reflectometry," *Smart Materials and Structures*, vol. 20, no. 8, p. 085028, 2011.

[61] Z. Li, Y. Tong, X. Fu, J. Wang, Q. Guo, H. Yu, and X. Bao, "Simultaneous distributed static and dynamic sensing based on ultra-short fiber bragg gratings," *Optics Express*, vol. 26, no. 13, pp. 17 437–17 446, 2018.

[62] J. M. López-Higuera, L. R. Cobo, A. Q. Incera, and A. Cobo, "Fiber optic sensors in structural health monitoring," *Journal of lightwave technology*, vol. 29, no. 4, pp. 587–608, 2011.

[63] H.-N. Li, D.-S. Li, and G.-B. Song, "Recent applications of fiber optic sensors to health monitoring in civil engineering," *Engineering structures*, vol. 26, no. 11, pp. 1647–1657, 2004.

[64] A. Barrias, J. R. Casas, and S. Villalba, "A review of distributed optical fiber sensors for civil engineering applications," *Sensors*, vol. 16, no. 5, p. 748, 2016.

[65] H. Huang and Z. Wu, "Monitoring and structural analysis of a rehabilitated box girder bridge based on long-gauge strain sensors," *Structural Health Monitoring*, vol. 17, no. 3, pp. 586–597, 2018.

[66] M. Enckell, B. Glisic, F. Myrvoll, and B. Bergstrand, "Evaluation of a large-scale bridge strain, temperature and crack monitoring with distributed fibre optic sensors," *Journal of Civil Structural Health Monitoring*, vol. 1, no. 1-2, pp. 37–46, 2011.

[67] W. Zhang, J. Gao, B. Shi, H. Cui, and H. Zhu, "Health monitoring of rehabilitated concrete bridges using distributed optical fiber sensing," *Computer-Aided Civil and Infrastructure Engineering*, vol. 21, no. 6, pp. 411–424, 2006.

[68] J.-M. Henault, G. Moreau, S. Blairon, J. Salin, J.-R. Courivaud, F. Taillade, E. Merliot, J.-P. Dubois, J. Bertrand, S. Buschaert *et al.*, "Truly distributed optical fiber sensors for structural health monitoring: from the telecommunication optical fiber drawling tower to water leakage detection in dikes and concrete structure strain monitoring," *Advances in Civil Engineering*, vol. 2010, 2010.

[69] R. Di Sante, "Fibre optic sensors for structural health monitoring of aircraft composite structures: Recent advances and applications," *Sensors*, vol. 15, no. 8, pp. 18 666–18 713, 2015.

[70] K. Chandler, S. Ferguson, T. Graver, A. Csipkes, and A. Mendez, "On-line structural health and fire monitoring of a composite personal aircraft using an fbg sensing system," in *Smart Sensor Phenomena, Technology, Networks, and Systems 2008*, vol. 6933. International Society for Optics and Photonics, 2008, p. 69330H.

[71] H. Guo, G. Xiao, N. Mrad, and J. Yao, "Fiber optic sensors for structural health monitoring of air platforms," *Sensors*, vol. 11, no. 4, pp. 3687–3705, 2011.

[72] A. Tessler and J. L. Spangler, "A least-squares variational method for full-field reconstruction of elastic deformations in shear-deformable plates and shells," *Computer methods in applied mechanics and engineering*, vol. 194, no. 2-5, pp. 327–339, 2005.

[73] H.-I. Kim, L.-H. Kang, and J.-H. Han, "Shape estimation with distributed fiber bragg grating sensors for rotating structures," *Smart Materials and Structures*, vol. 20, no. 3, p. 035011, 2011.

[74] J.-H. Kim, Y. Park, Y.-Y. Kim, P. Shrestha, and C.-G. Kim, "Aircraft health and usage monitoring system for in-flight strain measurement of a wing structure," *Smart Materials and Structures*, vol. 24, no. 10, p. 105003, 2015.

[75] I. Kressel, J. Balter, N. Mashiach, I. Sovran, O. Shapira, N. Shemesh, B. Glamm, A. Dvorjetski, T. Yehoshua, and M. Tur, "High speed, in-flight structural health monitoring system for medium altitude long endurance unmanned air vehicle," in *EWSHM-7th European workshop on structural health monitoring*, 2014.

[76] N. Saito, T. Yari, and K. Enomoto, "Flight demonstration testing with distributed optical fiber sensor," in *EWSHM-7th European Workshop on Structural Health Monitoring*, 2014.

[77] I. Mckenzie and N. Karafolas, "Fiber optic sensing in space structures: the experience of the european space agency," in *17th International Conference on Optical Fibre Sensors*, vol. 5855. International Society for Optics and Photonics, 2005, pp. 262–270.

[78] D. C. Betz, G. Thursby, B. Culshaw, and W. J. Staszewski, "Acousto-ultrasonic sensing using fiber bragg gratings," *Smart Materials and Structures*, vol. 12, no. 1, p. 122, 2003.

[79] H. Murayama, K. Kageyama, H. Naruse, A. Shimada, and K. Uzawa, "Application of fiber-optic distributed sensors to health monitoring for full-scale composite structures," *Journal of Intelligent Material Systems and Structures*, vol. 14, no. 1, pp. 3–13, 2003.

[80] G. Wang, K. Pran, G. Sagvolden, G. Havsgård, A. Jensen, G. Johnson, and S. Vohra, "Ship hull structure monitoring using fibre optic sensors," *Smart materials and structures*, vol. 10, no. 3, p. 472, 2001.

[81] K. Majewska, M. Mieloszyk, W. Ostachowicz, and A. Król, "Experimental method of strain/stress measurements on tall sailing ships using fibre bragg grating sensors," *Applied Ocean Research*, vol. 47, pp. 270–283, 2014.

[82] L. Ren, H. Li, J. Zhou, D.-S. Li, and L. Sun, "Health monitoring system for offshore platform with fiber bragg grating sensors," *Optical Engineering*, vol. 45, no. 8, p. 084401, 2006.

[83] T. Fu, Y. Liu, Q. Li, and J. Leng, "Fiber optic acoustic emission sensor and its applications in the structural health monitoring of cfrp materials," *Optics and Lasers in Engineering*, vol. 47, no. 10, pp. 1056–1062, 2009.

[84] J. Leng and A. Asundi, "Non-destructive evaluation of smart materials by using extrinsic fabry–perot interferometric and fiber bragg grating sensors," *Ndt & E International*, vol. 35, no. 4, pp. 273–276, 2002.

[85] S. Pal, T. Sun, K. T. Grattan, S. A. Wade, S. F. Collins, G. W. Baxter, B. Dussardier, and G. Monnom, "Non-linear temperature dependence of bragg gratings written in different fibres, optimised for sensor applications over a wide range of temperatures," *Sensors and Actuators A: Physical*, vol. 112, no. 2-3, pp. 211–219, 2004.

[86] M. Zhu and H. Murayama, "Fast demodulation of ofdr based long length fbg sensing system for noisy signals," *Optics express*, vol. 26, no. 16, pp. 19 804–19 814, 2018.

[87] D.-P. Zhou, Z. Qin, W. Li, L. Chen, and X. Bao, "Distributed vibration sensing with time-resolved optical frequency-domain reflectometry," *Optics express*, vol. 20, no. 12, pp. 13 138–13 145, 2012.

[88] L. Shiloh and A. Eyal, "Distributed acoustic and vibration sensing via optical fractional fourier transform reflectometry," *Optics Express*, vol. 23, no. 4, pp. 4296–4306, 2015.

[89] D. Wada, H. Igawa, H. Murayama, and T. Kasai, "Signal processing method based on group delay calculation for distributed bragg wavelength shift in optical frequency domain reflectometry," *Optics express*, vol. 22, no. 6, pp. 6829–6836, 2014.

[90] E. Sejdić, I. Djurović, and J. Jiang, "Time–frequency feature representation using energy concentration: An overview of recent advances," *Digital Signal Processing*, vol. 19, no. 1, pp. 153–183, 2009.

[91] K. Naganuma, K. Mogi, and H. Yamada, "Group-delay measurement using the fourier transform of an interferometric cross correlation generated by white light," *Optics letters*, vol. 15, no. 7, pp. 393–395, 1990.

[92] D. Schlichthärle, *Digital Filters: Basics and Design*, 2nd ed. Springer, 2010.

[93] S. S. Haykin, *Neural networks and learning machines*, 3rd ed. Pearson Upper Saddle River, 2009.

[94] M. Xu, J. Archambault, L. Reekie, and J. Dakin, "Thermally-compensated bending gauge using surface-mounted fibre gratings," *International Journal of Optoelectronics*, vol. 9, no. 3, pp. 281–283, 1994.

[95] J. Echevarria, A. Quintela, C. Jauregui, and J. Lopez-Higuera, "Uniform fiber bragg grating first-and second-order diffraction wavelength experimental characterization for strain-temperature discrimination," *IEEE Photonics Technology Letters*, vol. 13, no. 7, pp. 696–698, 2001.

[96] M. Sudo, M. Nakai, K. Himeno, S. Suzaki, A. Wada, and R. Yamauchi, "Simultaneous measurement of temperature and strain using panda fiber grating," in *Optical Fiber Sensors*. Optical Society of America, 1997, p. OWC7.

[97] M. Zhu, H. Murayama, D. Wada, and K. Kageyama, "Dependence of measurement accuracy on the birefringence of panda fiber bragg gratings in distributed simultaneous strain and temperature sensing," *Optics Express*, vol. 25, no. 4, pp. 4000–4017, 2017.

[98] D. A. Belsley, E. Kuh, and R. E. Welsch, *Regression diagnostics: Identifying influential data and sources of collinearity*. John Wiley & Sons, 2005, vol. 571.

[99] K. Hayashi, K. Izoe, K. Aikawa, and M. Kudo, "High performance polarization-maintaining optical fiber," *Technical report of IEICE. OFT*, vol. 114, no. 64, pp. 25–30, may 2014.

[100] R. Tennyson, A. Mufti, S. Rizkalla, G. Tadros, and B. Benmokrane, "Structural health monitoring of innovative bridges in canada with fiber optic sensors," *Smart materials and Structures*, vol. 10, no. 3, p. 560, 2001.

[101] J.-R. Lee, C.-Y. Ryu, B.-Y. Koo, S.-G. Kang, C.-S. Hong, and C.-G. Kim, "In-flight health monitoring of a subscale wing using a fiber bragg grating sensor system," *Smart materials and structures*, vol. 12, no. 1, p. 147, 2003.

[102] Y. Okabe, S. Yashiro, T. Kosaka, and N. Takeda, "Detection of transverse cracks in cfrp composites using embedded fiber bragg grating sensors," *Smart Materials and Structures*, vol. 9, no. 6, p. 832, 2000.

[103] S. Takeda, S. Minakuchi, Y. Okabe, and N. Takeda, "Delamination monitoring of laminated composites subjected to low-velocity impact using small-diameter fbg sensors," *Composites Part A: Applied Science and Manufacturing*, vol. 36, no. 7, pp. 903–908, 2005.

[104] M. Davis, A. Kersey, J. Sirkis, and E. Friebele, "Shape and vibration mode sensing using a fiber optic bragg grating array," *Smart Materials and Structures*, vol. 5, no. 6, p. 759, 1996.

[105] R. G. Duncan, M. E. Froggatt, S. T. Kreger, R. J. Seeley, D. K. Gifford, A. K. Sang, and M. S. Wolfe, "High-accuracy fiber-optic shape sensing," in *Sensor Systems and Networks: Phenomena, Technology, and Applications for NDE and Health Monitoring 2007*, vol. 6530. International Society for Optics and Photonics, 2007, p. 65301S.

[106] J. P. Moore and M. D. Rogge, "Shape sensing using multi-core fiber optic cable and parametric curve solutions," *Optics express*, vol. 20, no. 3, pp. 2967–2973, 2012.

[107] P.-N. Tan *et al.*, *Introduction to data mining.* Pearson Education India, 2007.

[108] M. Zhu and H. Murayama, "Simultaneous measurement of dynamic strain and temperature distribution using high birefringence panda fiber bragg grating," in *Optical Fiber Sensors Conference (OFS), 2017 25th.* IEEE, 2017, pp. 1–4.

[109] M. Zhu, H. Murayama, and D. Wada, "Self-evaluation of panda-fbg based sensing system for dynamic distributed strain and temperature measurement," *Sensors*, vol. 17, no. 10, p. 2319, 2017.

[110] F. L. Coolidge, *Statistics: A gentle introduction.* Sage Publications, 2012.

[111] P. Fieguth, *Statistical image processing and multidimensional modeling.* Springer Science & Business Media, 2010.

[112] R. D. Boyle and R. C. Thomas, *Computer vision: A first course.* Blackwell Scientific Publications, Ltd., 1988.

[113] A. Deraemaeker and K. Worden, *New trends in vibration based structural health monitoring.* Springer Science & Business Media, 2012, vol. 520.

[114] Z. Zhang and X. Bao, "Distributed optical fiber vibration sensor based on spectrum analysis of polarization-otdr system," *Optics express*, vol. 16, no. 14, pp. 10 240–10 247, 2008.

[115] J. C. Juarez, E. W. Maier, K. N. Choi, and H. F. Taylor, "Distributed fiber-optic intrusion sensor system," *Journal of lightwave technology*, vol. 23, no. 6, pp. 2081–2087, 2005.

[116] D. Arbel and A. Eyal, "Ofdr with double interrogation for dynamic quasi-distributed sensing," *Optics Express*, vol. 22, no. 3, pp. 2299–2308, 2014.

[117] X. Hong, H. Guo, J. Wu, K. Xu, Y. Zuo, Y. Li, and J. Lin, "An intrusion detection sensor based on coherent optical time domain reflector," *Microwave and Optical Technology Letters*, vol. 52, no. 12, pp. 2746–2748, 2010.

[118] Z. Ding, X. S. Yao, T. Liu, Y. Du, K. Liu, Q. Han, Z. Meng, and H. Chen, "Long-range vibration sensor based on correlation analysis of optical frequency-domain reflectometry signals," *Optics express*, vol. 20, no. 27, pp. 28 319–28 329, 2012.

[119] S. Wang, X. Fan, Q. Liu, and Z. He, "Distributed fiber-optic vibration sensing based on phase extraction from time-gated digital ofdr," *Optics Express*, vol. 23, no. 26, pp. 33 301–33 309, 2015.